

OBTAINING SOIL-WATER CHARACTERISTIC CURVES BY NUMERICAL
MODELING OF DRAINAGE IN PARTICULATE MEDIA

A THESIS SUBMITTED TO
THE GRADUATE SCHOOL OF NATURAL AND APPLIED SCIENCES
OF
MIDDLE EAST TECHNICAL UNIVERSITY

BY

AMIR SHOARIAN SATTARI

IN PARTIAL FULFILLMENT OF THE REQUIREMENTS
FOR
THE DEGREE OF MASTER OF SCIENCE
IN
CIVIL ENGINEERING

SEPTEMBER 2014

Approval of the thesis:

**OBTAINING SOIL-WATER CHARACTERISTIC CURVES BY NUMERICAL
MODELING OF DRAINAGE IN PARTICULATE MEDIA**

Submitted by **AMIR SHOARIAN SATTARI** in partial fulfillment of the requirements for the degree of **Master of Science in Civil Engineering Department, Middle East Technical University** by,

Prof. Dr. Canan Özgen
Dean, Graduate School of **Natural and Applied Sciences**

Prof. Dr. Ahmet Cevdet Yalçiner
Head of Department, **Civil Engineering**

Inst. Dr. Nabi Kartal Toker
Supervisor, **Civil Engineering Dept., METU**

Examining Committee Members:

Prof. Dr. Erdal Çokça
Civil Engineering Dept., METU

Inst. Dr. Nabi Kartal Toker
Civil Engineering Dept., METU

Asst. Prof. Dr. Nejan Huvaj Sarihan
Civil Engineering Dept., METU

Asst. Prof. Dr. Onur Pekcan
Civil Engineering Dept., METU

Prof. Dr. Hakan I. Tarman
Engineering Science Dept., METU

Date: 01.09.2014

I hereby declare that all information in this document has been obtained and presented in accordance with academic rules and ethical conduct. I also declare that, as required by these rules and conduct, I have fully cited and referenced all material and results that are not original to this work.

Name, Last Name: Amir Shoarian Sattari

Signature

ABSTRACT

OBTAINING SOIL-WATER CHARACTERISTIC CURVES BY NUMERICAL MODELING OF DRAINAGE IN PARTICULATE MEDIA

Shoarian Sattari, Amir

M. S., Department of Civil Engineering

Supervisor: Dr. Nabi Kartal Toker

September 2014, 143 pages

The soil water characteristic curve (SWCC) reflects fundamental drainage properties of partially saturated soils by revealing the relation between soil suction and water content. Although during the past decades, various experimental methods have been proposed for obtaining the SWCC, these approaches are generally time consuming, expensive and highly dependent on operator skills. One solution to this has been sought through various empirical or physico-empirical formulations that link the SWCC to common soil properties, through transformation calculations or within available SWCC databases. Another solution is to fit a curve onto partial SWCC data via regression analysis. A more reasonable approach both in terms of accuracy and cost could be to simulate the pore-scale drainage of soil medium with application of computer modeling techniques. This study is aims to model the drainage of soil medium through developing a computer program in MATLAB for simulating the drying SWCC. In the proposed approach, initially, a solid phase of soil structure is generated based on the particle size distribution as well as void ratio (e) of a given soil sample. Next, the volume of pore water is divided into two main portions: (i) bulk water and, (ii) liquid bridges. Assuming the inter-particle region of three adjacent particles with minimum hydraulic radius as a pore throat, the air entry pressure of each

pore throat can be computed. To this end, the Young-Laplace equation is solved through a combination of the finite difference approximation and Newton-Raphson (Jacobian) numerical methods. In this simulation the amount of applied suction is gradually increased and resulting drainage scheme of bulk pores is visualized step by step. Eventually the final residual water content of bulk pores and liquid bridges after each suction increment are determined and plotted as SWCC. The usefulness of the developed computer program is verified by comparison of the obtained SWCC to those attained based on experimental and empirical techniques. The application of proposed method is limited to non-plastic soils, and is not suitable for modeling clay particles. The developed method is capable of providing SWCC, with an almost perfect level of conformity to the experimental results, in a timely manner. Moreover, it is shown that the SWCCs obtained by the proposed algorithm are much more accurate than results of the estimation methods found in the literature for a variety of real soils.

Keywords: Unsaturated Soils, Soil-Water Characteristic Curve, Air Entry Pressure, Pore Network, Numerical Modeling.

ÖZ

PARÇACIKLI ORTAMDA DRENAJIN SAYISAL MODELLEMESİ İLE ZEMİN-SU KARAKTERİSTİK EĞRİSİ ELDE EDİLMESİ

Shoarian Sattari, Amir

Yüksek Lisans, İnşaat Mühendisliği Bölümü

Tez Yöneticisi: Dr. Nabi Kartal Toker

Eylül 2014, 143 sayfa

Zemin emmesi ile su içeriği arasındaki ilişkiyi gösteren zemin-su karakteristik eğrisi (ZSKE) doygun olmayan zeminlerin drenaj özelliklerini yansıtır. Yakın geçmişte ZSKE ölçümü için geliştirilmiş olan çeşitli deneysel yöntemler çoğunlukla zaman alıcı, pahalı, ve kullanıcının becerisinden fazlaca etkilenen prosedürlerdir. Bu problemin bir çözümü ampirik veya yarı-ampirik hesaplar yoluyla temel zemin özelliklerinden dönüştürmek veya mevcut veritabanlarındaki eğrilerle benzeştirmek yoluyla ZSKE'ne bağlamaktır. Diğer bir yaygın çözüm kısmi ZSKE veri noktasına regresyon ile bir eğri oturtmaktır. İsbet ve maliyet açısından daha akılcı bir yaklaşım zemin ortamını gözenek ölçeğinde bilgisayarla modellemek olabilir. Bu çalışma toprak ortamının drenajının MATLAB platformunda hazırlanmış bir bilgisayar yazılımıyla modellenmesi yoluyla ZSKE'nin elde edilmesini hedeflemiştir. Önerilen yaklaşımda öncelikle dane boyu dağılımı ve boşluk oranı esas alınarak zemin yapısı oluşturulur. Sonra boşluk suyu hacmi boşluk gövdesi ve sıvı köprüleri olarak ikiye ayrılır. Her üç birbirine komşu parçacığın arasında kalan boşluğun en küçük kesiti boşluk boğazı olarak varsayılır, ve her boşluk boğazının hava giriş basıncı hesaplanabilir. Bu amaç için Young-Laplace denklemi sonlu farklar yakınsaması ve Newton-Raphson (Jacobi) sayısal metodlarının birlikte kullanılması yoluyla çözülür.

Bu simülasyonda suya uygulanan emme kademeli olarak arttırılarak drenaj adım adım izlenebilir. Sonunda boşluk gövdelerinde ve sıvı köprülerinde kalan su içeriği her emme kademesi için hesaplanarak ZSKE çizilir. Önerilen yöntemin kullanımı plastik olmayan zeminlerle sınırlıdır, kil danelerini modellemek için uygun değildir. Geliştirilen yöntem deneysel sonuçlarile neredeyse mükemmel tutarlılığa sahip ZSKE'lerini nisbeten hızlıca çıkarabilmektedir. Ayrıca geliştirilen yöntemin, çeşitli gerçek toprak numuneleri için literatürdeki ampirik hesap yöntemlerinin bulabildiğinden çok daha isabetli şekilde ZSKE'leri hesaplayabildiği gösterilmiştir.

Anahtar Kelimeler: Doygun Olmayan Zeminler, Zemin-Su Karakteristik Eğrisi, Gözenek Ağı, Hava Giriş Basıncı, Sayısal Modelleme.

To My Family

ACKNOWLEDGMENTS

I would like to express the deepest appreciation to my advisor Dr. Nabi Kartal Toker for his support, insightful comments and encouragements during this study. Without his guidance and persistent help this dissertation would not have been accomplished.

I would like to express my deepest gratitude to my thesis committee members: Prof. Dr. Erdal Çokça, Asst. Prof. Dr. Nejan Huvaj Sarihan, Asst. Prof. Dr. Onur Pekcan and Prof. Dr. Hakan I. Tarman for their useful feedback.

I would like to offer my special thanks to Dr. Saied Kazemzadeh Azad for his comments and helpful discussions throughout this research.

Special thanks also to my friends Mohammad Ahmadi Adli and Reza Ahmadi Naghadeh for permission to use their experimental data in my research.

My sincere thanks also goes to Asst. Prof. Dr. Fatma T. Köksal, who provided me the microscopic photographs of soils.

And finally, I would like to thank my family for their understanding and unconditional support throughout my studies.

TABLE OF CONTENTS

ABSTRACT	v
ÖZ	vii
ACKNOWLEDGMENTS	x
TABLE OF CONTENTS	xi
LIST OF TABLES	xv
LIST OF FIGURES	xvi
LIST OF SYMBOLS	xix
LIST OF ABBREVIATIONS	xxiii
CHAPTERS	
1. INTRODUCTION	1
1.1 Unsaturated Soil Mechanics	1
1.2 Scope of the Research	2
1.3 Outline of the Thesis	3
2. LITERATURE REVIEW	5
2.1 Tensile Strength of Water	5
2.1.1 Surface Curvature	6
2.1.2 Meniscus	9
2.1.3 Capillary Action	10
2.2 Soil Water Energy State	10
2.2.1 Total Suction of Soil	11
2.2.2 Matric Potential	12
2.2.3 Osmotic Potential	12
2.2.4 Application of Suction	13
2.2.5 Measurement of Soil Suction	13
2.3 Porous Medium	13
2.3.1 Pore-Scale Modeling	14

2.3.2 Packing of Uniform Spheres	16
2.3.2.1 Cubic Packing	16
2.3.2.2 Hexagonal Packing	17
2.3.2.3 Rhombohedral Packing	18
2.3.3 Pendular Rings	18
2.3.3.1 Volume of Pendular Rings	19
2.4 Drainage	24
2.4.1 Drainage Models	25
2.4.2 Air Entry Pressure	26
2.4.3 Pore-Scale Drainage	27
2.5 Soil Water Characteristic Curves	28
2.5.1 Hysteretic Effect	29
2.5.2 Laboratory Measurement Techniques	30
2.5.2.1 Hanging Column	31
2.5.2.2 Pressure Chamber	32
2.5.2.3 MIT Method	32
2.5.3 Empirical Methods for Predicting the SWCC	33
2.5.3.1 Fitting Curves	33
2.5.3.2 Estimation Techniques	34
2.5.3.2.1 Arya and Paris (1981) Method	34
2.5.3.2.2 Fredlund and Wilson (1997) Method	36
2.6 Numerical Methods	37
2.6.1 Taylor Series	37
2.6.2 Newton-Raphson Method	37
2.6.3 Finite Difference Approximation	39
3. PORE-SCALE MODELING OF DRAINAGE	43
3.1 Outline	43
3.2 Solid Phase of Soil Structure	45
3.2.1 Generating the Particles	45
3.2.2 Packing the Particles	46
3.2.2.1 Particle Arrangement	47

3.2.2.2 Stability Control	54
3.2.2.3 Periodic Boundary Condition	54
3.2.2.4 Void Ratio of Simulated Medium	57
3.2.3 Results of Packing Algorithm	59
3.2.3.1 Variability of Void Ratio	60
3.2.3.2 Homogeneity of Simulated Medium	61
3.3 Identification of Porous Medium	62
3.3.1 Defining the Pore Throats.....	63
3.3.2 Throat Side-Points	65
3.3.3 Identifying Bulk Pores	68
3.3.4 Volume of Bulk Pores	72
3.3.5 Pendular Rings	73
3.3.5.1 Possibility of Pendular Rings Formation	73
3.3.5.2 Volume of Pendular Rings	74
3.4 Air Entry Pressure of Pore Throats	75
3.4.1 Grid Placement in Pore Throat Region	76
3.4.2 Characteristics of Grid Points	78
3.4.2.1 Boundary Points	80
3.4.2.2 Curvature Points	82
3.4.3 Finite Difference Approximation	83
3.4.4 Newton-Raphson (Jacobian) Method	84
3.4.4.1 Convergence of Newton-Raphson Method	85
3.4.5 Parametric Study	87
3.4.5.1 Effect of B Variable on AEP Results	87
3.4.5.2 Effect of C Variable on AEP Results	88
3.5 Drainage of Simulated Medium	90
3.6 User Interface	94
3.6.1 Input Variables of the Algorithm	94
3.6.2 Outputs of the Algorithm	95
4. INTERPRETATION AND COMPARISION OF RESULTS	97
4.1 Parametric Results	97

4.1.1 Effect of Particles Size on Simulated SWCC	97
4.1.2 Effect of Void Ratio on Simulated SWCC	98
4.1.3 Effect of Contact Angle on Simulated SWCC	99
4.2 Verification Using Experimental Results of Spherical Particles	100
4.2.1 Material Properties	100
4.2.2 Interpretation of Experimental SWCC Data	105
4.2.3 Simulated SWCC Results of Glass Beads	107
4.3 Verification with Real Soils	111
4.3.1 Material Properties	112
4.3.2 Estimation Methods	116
4.3.2.1 Arya and Paris (1981) Method	116
4.3.2.2 Fredlund and Wilson (1997) Method	118
4.3.3 Simulated SWCC of Real Soils	118
4.4 Computational Performance	123
5. CONCLUSION	127
5.1 Summary	127
5.2 Discussion of the Results	127
5.3 Recommendations for Future Works	129
REFERENCES	131

LIST OF TABLES

TABLES

Table 3.1 Void ratios of simulated media	60
Table 3.2 Standard deviation and variance of void ratio	61
Table 3.3 Void ratios of simulated non-uniform medium and divided halves	62
Table 3.4 PSDs of simulated cubic medium and divided halves	62
Table 3.5 Effect of B variable on AEP results and average computing time	88
Table 3.6 Effect of C variable on AEP results and average computing time	89
Table 4.1 Physical properties of specimens presented by Toker (2007)	102
Table 4.2 The ω_{sat} and e of mostly uniform specimens presented by Toker (2002) .	104
Table 4.3 The ω_{sat} and e of gap-graded specimens presented by Toker (2002)	105
Table 4.4 Properties of real soils	115
Table 4.5 Physical properties of real soils	116
Table 4.6 Dividing the PSD of sandy soil into small segments	117
Table 4.7 Arya and Paris (1981) parameters for sandy soil	117
Table 4.8 Comparison of determined AEPs of real soils	121
Table 4.9 Comparison of maximum slope of resulted SWCC	122
Table 4.10 Comparison of maximum relative errors in suction values of real soils	122
Table 4.11 Comparison of maximum absolute errors in water content values of real soils	123

LIST OF FIGURES

FIGURES

Figure 2.1 Infinitesimal segment of curve surface	6
Figure 2.2 Infinitesimal element of surface in Cartesian coordinate	8
Figure 2.3 Contact angle of water droplet with solid surface	10
Figure 2.4 The pore water in form of (a) bulk water and, (b) water bridges	14
Figure 2.5 Cubic packing	17
Figure 2.6 Hexagonal packing	17
Figure 2.7 Rhombohedral packing	18
Figure 2.8 Torus pendular ring (Sjoblom, 2000)	19
Figure 2.9 Cross-section of pendular ring	20
Figure 2.10 Spherical cap	24
Figure 2.11 Drainage of pore water	27
Figure 2.12 SWCC of fine and coarse soils	29
Figure 2.13 Hysteretic effect	30
Figure 2.14 Schematic of hanging column setup (ASTM, D6836-02)	31
Figure 2.15 Schematic of pressure chamber setup (ASTM, D6836-02)	32
Figure 2.16 Schematic of MIT method setup (Toker, 2007)	33
Figure 3.1 Flow chart of proposed algorithm	44
Figure 3.2 Arbitrary PSD and defined segments	46
Figure 3.3 Flow chart of particle packing process	47
Figure 3.4 Defined β and ϕ angles in Cartesian coordinate	50
Figure 3.5 (a) Stable and, (b) unstable conditions of red particle	55
Figure 3.6 Projection of center points of relevant particles for stability control of n^{th} particle	55
Figure 3.7 Particle mirroring in XY plane	56
Figure 3.8 The simulated (a) uniform and, (b) non-uniform specimens	59
Figure 3.9 PSD of non-uniform specimen	60

Figure 3.10 Flow chart of porous medium identification	63
Figure 3.11 Defined throat plane	64
Figure 3.12 Invalid and valid throat planes in XY plane	65
Figure 3.13 Generated Side-Points	67
Figure 3.14 Schematic of the bulk pore identification process, 1th method	69
Figure 3.15 The bulk pore entrapped between four particles and relevant Side-Points in 3D	69
Figure 3.16 Schematic of the bulk pore identification process, 2nd method	70
Figure 3.17 The bulk entrapped between six particles	71
Figure 3.18 The bulk entrapped between seven particles	72
Figure 3.19 Schematic of connectivity of pendular rings	74
Figure 3.20 Flow chart of AEP determination process	76
Figure 3.21 Grid defined in pore throat region	77
Figure 3.22 Grid points located inside throat plane	78
Figure 3.23 Properties of grid points	79
Figure 3.24 Contact angle in particle-air-water interface	80
Figure 3.25 Grid points in XY plane	83
Figure 3.26 Properties of grid points after each iteration	86
Figure 3.27 The air-water surfaces when the applied suction is (a) 2, (b) 3.7 and, (c) 4.01 kPa	89
Figure 3.28 Schematic of drainage process	91
Figure 4.1 Effect of particles size on SWCC	98
Figure 4.2 Effect of void ratio on SWCC	99
Figure 4.3 Effect of contact angle on SWCC	100
Figure 4.4 Microscopic photographs of (a) Type 1 and, (b) Type 2 glass beads	101
Figure 4.5 SWCC of mostly uniform (Type 1) and perfectly uniform (Type 2) specimens (Toker, 2007)	102
Figure 4.6 SWCC of mostly uniform specimens (Toker, 2002)	103
Figure 4.7 SWCC of gap-graded specimens (Toker, 2002)	104
Figure 4.8 Comparison of SWCC of mostly uniform (Type 1) and perfectly uniform (Type 2) specimens given by Toker (2002, 2007)	106
Figure 4.9 PSD of gap-graded specimens with modified fractions	106

Figure 4.10 Comparison of simulated SWCC with experimental results given by Toker (2007)	107
Figure 4.11 Comparison of simulated SWCC with experimental results given by Toker (2002)	108
Figure 4.12 Comparison of simulated SWCC (modified fractions) with experimental results given by Toker (2002)	109
Figure 4.13 Simulated SWCCs of gap-graded specimens consist of (a) 13% (b) 18% (c) 25% (d) 35% and, (e) 50% fine fraction and their comparison with experimental data given by Toker (2002)	110
Figure 4.14 Comparison of (a) void ratios and, (b) AEP of simulated media with experimental data of gap-graded specimens given by Toker (2002)	111
Figure 4.15 PSD of sand (Fredlund and Wilson, 1997)	112
Figure 4.16 PSD of NJFS (Toker, 2002)	113
Figure 4.17 PSD of quartz sand (Ahmadi Adli, 2014)	113
Figure 4.18 Microscopic photograph of quartz sand	114
Figure 4.19 PSD of quartz silt (Ahmadi Naghadeh, 2014)	114
Figure 4.20 Microscopic photograph of quartz silt	115
Figure 4.21 Comparison of the SWCC results of sandy soil with experimental data given by Fredlund and Wilson (1997)	119
Figure 4.22 Comparison of the SWCC results of NJFS with experimental data given by Toker (2002)	119
Figure 4.23 Comparison of the SWCC results of quartz sand with experimental data given by Ahmadi Adli (2014)	120
Figure 4.24 Comparison of the SWCC results of quartz silt with experimental data given by Ahmadi Naghadeh (2014)	121
Figure 4.25 Effect of total number of particles on simulated SWCCs of quartz sand	124
Figure 4.26 Effect of total number of particles on computing time	124
Figure 4.27 Computing time versus total number of particles	125

LIST OF SYMBOLS

SYMBOLS

CHAPTER 2

σ_{st}	Air-water interfacial tension
σ_{st}^o	Air-water interfacial tension at current temperature
κ	Mean curvature
r_1, r_2	Radii of curvature
β_1, β_2	Angles on orthogonal planes
Δu	Pressure difference
G	Gibbs energy
U	Internal energy of surface
p	Imposed pressure
V	Volume bound by air-water interface
X, Y, Z	Cartesian coordinates
Z_X	First order partial derivative of Z with respect to X
Z_Y	First order partial derivative of Z with respect to Y
Z_{XX}	Second order partial derivative of Z with respect to X
Z_{YY}	Second order partial derivative of Z with respect to Y
Z_{XY}	Partial derivative of Z with respect to X and Y
θ	Contact angle
ρ_w	Density of water
g	Acceleration due to gravity
h	Height of water inside capillary tube
r	Radius of capillary tube
Ψ_t	Total soil water potential
Ψ_g	Gravitational potential
Ψ_p	Pressure potential
Ψ_o	Osmotic potential

Ψ_m	Matric potential
Ψ	Total soil suction
u_a	Air pressure
u_w	Water pressure
$\frac{n}{V}$	Total ion concentration (Molar)
R	Universal gas constant
T	Absolute temperature (k)
ϕ_1, ϕ_2	Filling angles from center of particles
R_1, R_2	Principal radii of pendular ring
V	Volume of pendular ring
$D_{average}$	Average diameter of particles
R_s	Radius of pore channel in disks
J	Jacobian
J^{-1}	Inverse Jacobian
u_x	First order partial derivative of u with respect to x
u_{xx}	Second order partial derivative of u with respect to x
u_y	First order partial derivative of u with respect to y
u_{xy}	Partial derivative of Z with respect to x and y

CHAPTER 3

M	Finer mass percent
D	Sieve diameter
N_i	Number of particles in the i^{th} segment
d_j	Particles diameter
r	Radius of each particle
b	Dimension of sides of cubic medium
X, Y, Z	Cartesian coordinates
x, y, z	Coordinates of centers of particles
E_d	Euclidean distance between surface of two particles

M_R	Mirroring range of particles
x_m, y_m, z_m	Coordinates of Side-Points
R_{min}	Minimum radius of all packed particles
V_{cap}	Volume of spherical cap
v_s	Particle volume inside the domain
V_s	Total volume of particles inside the domain
e	Void ratio
V_t	Total volume of domain
V_v	Volume of voids
e_d	Target void ratio
D_f	Density factor
v	Variance
σ	Standard deviation
v_B	Proportion volume of bulk pores
ψ	Suction
σ_{st}	Air-water surface tension
R_1, R_2	Principal radii of pendular ring
v_p	Volume of pendular ring
A	Number of grid intervals
ΔX	Step sizes of grid points in X direction
ΔY	Step sizes of grid points in Y direction
x_p, y_p, z_p	Coordinates of grid points
θ	Contact angle
Z_X	First order partial derivative of Z with respect to X
Z_Y	First order partial derivative of Z with respect to Y
Z_{XX}	Second order partial derivative of Z with respect to X
Z_{YY}	Second order partial derivative of Z with respect to Y
Z_{XY}	Partial derivative of Z with respect to X and Y
J	Jacobian
J^{-1}	Inverse Jacobian

C	Boundary fixing parameter
D	Under-relaxation factor
V_w	Volume of pore water
V_a	Volume of pore air
U_w	Water pressure
S_I	Suction interval
S_m	Suction multiplier
S_{max}	Maximum applied suction
S_{min}	Minimum applied suction
V_R	Remaining water
V_B	Volume of drained bulk pore
V_P	Total volume of developed pendular rings
S	Degree of saturation
ω	Gravimetric water content
G_S	Specific gravity

CHAPTER 4

e	Void ratio
ω_{sat}	Gravimetric water content at saturation
G_S	Specific gravity
Θ	Volumetric water content
ω	Gravimetric water content
ρ_d	Dry density
ρ_w	Water density
M	Maximum slope of soil-water characteristic curves

LIST OF ABBREVIATIONS

ABBREVIATIONS

AEP.....	Air Entry Pressure
ASTM	American Society for Testing and Materials
BP	Bulk Pore
DEM	Discrete Element Method
FDA	Finite Difference Approximation
NJFS	New Jersey Fine Sand
PSD	Particle Size Distribution
SP.....	Side-Point
SWCC	Soil Water Characteristic Curves
TP.....	Throat Plane

CHAPTER 1

INTRODUCTION

1.1 Unsaturated Soil Mechanics

Generally, physical behavior of geomaterials is considered based on two states, saturated or completely dry. In these two states, pore of a soil medium is considered to be either filled with water or air phases. However, most of the soils in nature are partially saturated, and both water and air phases exist in porous media. In early 20th century, the first science-based behavior of saturated soils is put forth by Karl Terzaghi (Terzaghi, 1943). After Terzaghi theory, the behavior of unsaturated soils is considered by applying correction factors to saturated soil properties. In 1960s, for better understanding of unsaturated soil behavior and eliminating the error caused by correction factors, it was revealed that partially saturated soil properties would need to be represented in different methods than saturated soils.

With regard to designing purposes, understanding the fundamental properties of soil is essential. These properties explain the mechanisms of shear strength, deformation and flow of soil structure. Understanding of these properties in unsaturated soil mechanics can be practical in designing foundations or retaining walls, obtaining consolidation and swelling properties, understanding the seepage through soil media, computing amount of migration of leachate in landfills, measurement of wilting point of soils (Briggs et al., 1910) for agricultural purposes, etc. While considering the water distribution and flow in partially saturated soils, knowledge of soil hydraulic properties is essential. The main hydraulic properties of unsaturated soils are, (i) the relation of negative pore water pressure and water content of soil, known as soil water characteristic curve (SWCC) and (ii) the relation of hydraulic conductivity to soil

water pressure or soil water content. The SWCC is useful for obtaining different parameters of partially saturated soils such as shear strength, volume strain, pore size distribution, etc. The SWCC is also used for analyzing the flow in unsaturated soils by estimating the permeability of a partially saturated soil.

During the past decades, unsaturated soil's uncertainties have resulted in development of numerous empirical methods. In this regard, the water content relation with negative pore water pressure (soil suction) is studied, and various empirical methods are proposed so far. With regard to SWCC, these curves can be obtained from laboratory or in-situ tests but these tests are tedious, expensive and indeed time consuming. The need for faster and inexpensive techniques has resulted in formation of various empirical and physico-empirical methods for estimating the SWCC. These methods utilized the available SWCC data and proposed some empirical equations to fit the SWCC. However, limitations in available data and dependency of SWCC on texture and density of soils yielded inaccurate results.

1.2 Scope of the Research

The need for comprehensive methods based on mechanical properties of soils, which can lead to more accurate SWCC in shorter time periods, resulted in development of the proposed approach. In this research, the drying SWCC, which is mostly considered and determined from laboratory tests or estimation methods, is simulated. According to the proposed method, while considering the physical properties of soil, computer modeling of drying SWCC is considered. To this end, the available particle size distribution (PSD) and void ratio of soils are taken as the inputs. The first step of soil medium modeling, the solid phase of soil (particles) is simulated based on PSD as well as void ratio of a given soil specimen. For the sake of simplicity in calculations, all particles are assumed to be spherical. Later, the porous medium between the generated particles is identified and subsequently, drainage algorithm based on the air entry pressure (AEP) of every pore throat is developed. Finally, water content of simulated medium in each suction value is calculated and plotted as SWCC. In order

to validate the proposed method, obtained SWCC are compared with both experimental and empirical results found in the literature. The surface charges and ionic attractions that can be developed inside the soil medium are not considered in this research. Therefore, in this study, only SWCCs of non-plastic soils can be simulated. In addition, with the assumption of spherical particles, clayey soils cannot be simulated with proposed algorithm.

1.3 Outline of the Thesis

The next chapter contains background information of relevant topics. These topics are; tensile strength of water, soil suction, porous medium, drainage, SWCC and numerical methods. Chapter 3 describes the proposed method from the first step, which is solid phase simulation, to the final drainage step with details. The implemented methods for solid phase generation, porous medium identification, pore volume calculation, air entry pressure determination for individual pore throats and pendular ring calculations are described in this chapter. Chapter 4 of this study contains the comparison of simulated SWCC results with experimental and empirical results from the literature as well as a parametric study investigating changes in the SWCC with PSD, void ratio or contact angle. The conclusion chapter, 5, discusses achieved goals in this research and proposes some recommendations for future works.

CHAPTER 2

LITERATURE REVIEW

2.1 Tensile Strength of Water

It was back in 18th century that the notion of water's ability to withstand tension stresses arose (Bernoulli brothers, 1730). Later, in 1754, Euler presented mathematical form of this theory. This theory represented an inverse relation between velocity and pressure of fluid. The major advancement in this theory was proposed by Berthelot in 1850. He conducted experiments on sealed tubes filled with air and water. By cooling down the pre-heated tube, he applied tension and measured sudden change of water in cavitation point. He managed to measure water tensions of 5MPa with this method. Since then, different methods with similar basis to Berthelot's setup have been developed by various scientists (Lewis, 1961; Henderson et. al., 1980; Trevana, 1987). Trevana (1987) measured the highest water tension (27.7 MPa) using Berthelot's setup. In the past decade, Toker (2002) managed to analytically calculate the tensile strength of water around air bubbles in terms of pressure, via limit equilibrium solution. Alternative solutions through energy are also available (Maris and Balibar, 2000).

Scientifically, the rupture of water takes place in interfaces with other substances such as air. This issue prevents obtaining true values of tensile strength of water. In 1960, Adamson presented the relation of interfacial tension of an interface of small radii based on matric suction and curvature value as given by

$$\sigma_{st} = \frac{1}{(1 + \kappa \cdot 2 \times 10^{-8}(\text{cm}))} \sigma_{st}^o \quad (2.1)$$

where, κ is mean curvature, and σ_{st}^o is air-water tension in a flat surface at considered temperature. The tensile strength of water varies with temperature and in the case of 20 degrees Celsius, the surface tensile of air water interface is equal to 72.73×10^{-3} (N/m) (Adamson, 1960).

2.1.1 Surface Curvature

The unbalanced cohesive forces acting on a molecule of fluid at interface results in formation of surface tension. While considering the air water interface, a water molecule withstands asymmetric forces. In order to prevail on this asymmetry and reach the equilibrium, the surface of water undergoes tension and engenders curved surface. Figure 2.1 represents an infinitesimal segment of curved surface. In the case of force equilibrium, Figure 2.1 can be represented mathematically as given by,

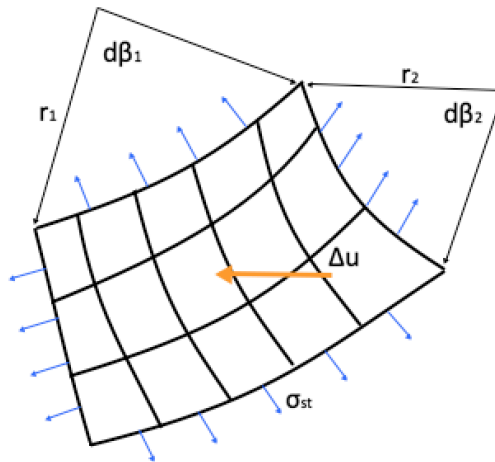


Figure 2.1: Infinitesimal segment of curve surface

$$\Delta u \cdot r_1 \cdot d\beta_1 \cdot r_2 \cdot d\beta_2 = \sigma_{st} \cdot r_1 \cdot d\beta_1 \cdot \frac{d\beta_2}{2} - \sigma_{st} \cdot r_2 \cdot d\beta_2 \cdot \frac{d\beta_1}{2}$$

$$\Delta u = \sigma_{st} \left(\frac{1}{r_1} - \frac{1}{r_2} \right) = 2\kappa\sigma_{st} \quad (2.2)$$

Where;

Δu = Pressure difference

σ_{st} = Surface tension

r_1 and r_2 = Radii of curvature

κ = Mean curvature of interface

Eq. (2.2) is known as Young-Laplace Equation. In air-water interfaces, Δu is the difference between pressure of air and water ($u_a - u_w$) and when it reaches the equilibrium, the mean curvature of interface will be a constant value. In order to obtain the variational derivatives of Young-Laplace equation (Eq. (2.2)), Gibbs energy theory (Willard Gibbs, 1873) is considered. When a surface reaches equilibrium at constant pressure and temperature, the Gibbs energy (G) is minimized.

$$G = U + pV \quad (2.3)$$

where, U is internal energy of surface, p is imposed pressure, and V is volume. By considering the same infinitesimal element of curve surface shown in Figure (2.1) in Cartesian coordinate (Figure 2.2), U is defined as:

$$U = \int \sigma_{st} dA \quad (2.4)$$

Representing the surface with explicit equation ($Z=Z(X,Y)$) will result in,

$$V = \iint Z(X, Y) \cdot dX \cdot dY = \iint Z \cdot dX \cdot dY \quad (2.5)$$

And,

$$\vec{\Delta s}_x = \begin{bmatrix} dX \\ 0 \\ Z_x dX \end{bmatrix} \quad \vec{\Delta s}_y = \begin{bmatrix} 0 \\ dY \\ Z_y dY \end{bmatrix}$$

$$dA = |\vec{dA}| = |\Delta\vec{s}_X \times \Delta\vec{s}_Y| = \sqrt{1 + Z_X^2 + Z_Y^2} \cdot dX \cdot dY \quad (2.6)$$

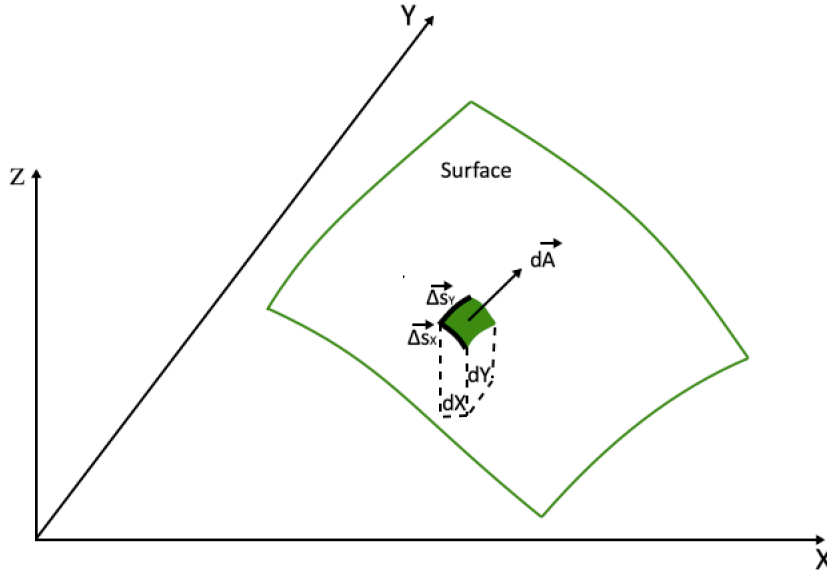


Figure 2.2: Infinitesimal element of surface in Cartesian coordinate

where, Z_X and Z_Y are partial derivatives of Z in X and Y directions, respectively. Combining Eq. (2.6) with Eq. (2.4) leads to,

$$U = \iint \sigma_{st} \cdot \sqrt{1 + Z_X^2 + Z_Y^2} \cdot dX \cdot dY \quad (2.7)$$

By substituting Eq. (2.5) and Eq. (2.7) into Eq. (2.3), G is equal to,

$$G = \iint \left(\sigma_{st} \cdot \sqrt{1 + Z_X^2 + Z_Y^2} + pZ \right) dX \cdot dY \quad (2.8)$$

So,

$$G = \iint F \cdot dX \cdot dY \quad (2.9)$$

where, F is function of Z , Z_X and Z_Y .

By Application of Euler-Lagrange equation (Euler, 1750) and considering the fact that Gibbs energy should be minimum in balance condition, the curvature equation will be resulted. The Euler-Lagrange equation is given by,

$$\frac{\partial F}{\partial Z} - \frac{d}{dX} \frac{\partial F}{\partial Z_X} - \frac{d}{dY} \frac{\partial F}{\partial Z_Y} = 0 \quad (2.10)$$

By solving Eq. (2.10), Eventually, following relation will be derived,

$$\frac{p}{\sigma_{st}} = \frac{(Z_{XX}(1+Z_Y^2)) - 2Z_X Z_Y Z_{XY} + (Z_{YY}(1+Z_X^2))}{(\sqrt{1+Z_X^2+Z_Y^2})^3} \quad (2.11)$$

where, Z_{XX} and Z_{YY} are second order partial derivatives of Z in X and Y directions, respectively, and Z_{XY} is a mixed derivative of Z in XY direction. In air-water interface, p is equal to suction (Δu).

2.1.2 Meniscus

In the contact surface of air-water interface with solids, air-water and solid-water interfaces meet. The meniscus will be formed in proximity of air-water surface with solid subjects due to surface tension. Figure 2.3 illustrates an example of contact angle of water droplet with solid surface. The meniscus can be either concave or convex, depending on substances forming liquid and solid phases. If adhesive forces within liquid fail to overcome cohesive forces in solid-liquid interface, the interface will curve and an angle lower than 90° with solid surface will form. These angles, which are also known as contact angles (θ), are less than 90° on the water side in most particle-water surfaces.

Contact angle can be affected by solid properties, surface roughness, and dissolved materials in water. For pure water on an absolutely clean glass surface, the contact

angle is considered to be less than 5° (Mattox, 1998). Although, this level of cleanness is extremely difficult to achieve and sustain (Bohren, 1987).

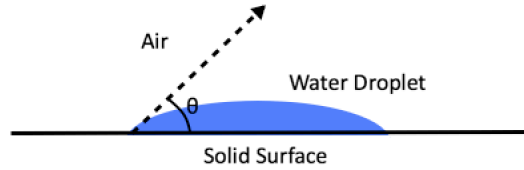


Figure 2.3: Contact angle of water droplet with solid surface

2.1.3 Capillary Action

The ability of water to rise inside a tube in opposition to gravity is called capillary action. The combinations of adhesive forces among tube and water as well as tension in air-water interface are main reasons of water rise in tube. The height of water (h) inside a tube has an inverse relation with radius (r) of tube as given in capillary equation.

$$h = \frac{2\sigma_{st} \cos(\theta)}{\rho_w \cdot g \cdot r} \quad (2.12)$$

where, θ is contact angle, ρ_w is density of water, and g is acceleration due to gravity.

2.2 Soil Water Energy State

The status of water in soils is described with amount of water and corresponding energy state. The kinetic and potential forms of energy are key factors in defining soil water status. Kinetic energy is obtained by motion and is proportional to square of velocity. In soil medium, water has slow movements so kinetic energy can be neglected. As a result of this assumption, soil water status under isothermal conditions are mostly due to potential energy, which is defined by position of soil water within

soil body. According to Aitchison (1965), the total potential of soil water is total of work that must be done per unit quantity of pure water to transfer reversibly and isothermally an infinitesimal unit quantity of water from a pool of pure water at reference elevation and pressure to the required elevation of soil water. The soil water is exposed to various force fields, which results in formation of soil water potential.

The total soil water potential (ψ_t) can be defined as sum of gravitational (ψ_g), pressure (ψ_p), osmotic (ψ_o) and matric (ψ_m) potentials.

$$\psi_t = \psi_g + \psi_p + \psi_o + \psi_m \quad (2.13)$$

Soil water moves from higher potential energy to lower till it reaches the equilibrium with surrounding media. The equilibrium requires that vector sum of various forces acting on a body of water in different directions to be zero.

2.2.1 Total Suction of Soil

In soil science, because of negligible pressure differences and movements at a considered point, gravitational and pressure factors are mostly neglected. Therefore, according to Eq. (2.13), the total sum of matric and osmotic potentials are known as total soil suction (ψ), which is usually referred as negative pore pressure in soil mechanics.

$$\psi = \psi_o + \psi_m \quad (2.14)$$

Various properties of soil profile, such as strength, deformation and hydraulic conductivity are function of soil suction. Over the centuries, thermo-dynamical aspects of soil suction have been studied theoretically by different scientists (Van Der Waals, 1893; Aitchison, 1965; Coussy and Fleureau, 2002) and its mechanical aspects mostly have been studied from a practical point of view.

2.2.2 Matric Potential

The matric potential (i.e. capillarity and adsorption) is result of interaction between solid phase and liquid phases. It appears due to physics of air-water interfaces and mainly is ascribed to capillary actions in soil profile. In saturated soil, where water is free to flow, matric potential has no influence and its value is zero. In contrast, in partially saturated soils attention is developed for matric potential, due to interaction between soil and water. Therefore, availability of water to move and its mobility in soil profile is determined by matric potential. The matric potential is defined as negative gage pressure in the pore water, which is equal to

$$\Psi_m = u_a - u_w \quad (2.15)$$

where, u_a and u_w are air and water pressures, respectively.

2.2.3 Osmotic Potential

The osmotic potential arises from differences in chemical composition of solutions within porous medium of soil. For an instance, the availability of salts in soil water, which results in osmotic potentials, makes it harder for plants to intake soil water even when water is present. In 1989, Petrucci altered the ideal gas equation and suggested Eq. (2.16) for determining quantity of osmotic potential.

$$\psi_o = \frac{n}{V}RT \quad (2.16)$$

where, $\frac{n}{V}$ is total ion concentration, R is gas constant, and T is absolute temperature.

In practical problems of geotechnical engineering, the osmotic potential of soil suction is neglected (Nelson & Miller, 1992). Therefore, the total suction of soil will be merely equal to matric suction.

2.2.4 Application of Suction

Different approaches for measuring and inducing soil suction are presented in references such as Fredlund & Rahardjo (1993). Application of suction into a soil specimen is carried out either by applying air pressure or changing relative humidity of environment. The methods, such as pressure plate (ASTM, C1699-09), pressure membrane (ASTM, D3152-72), and axis translation (Anderson et al., 1997) are implemented by applying air pressure into chamber. Measuring differences between pore water pressure and air pressure provides amount of matric suction inside specimen. The methods considering a change in humidity are carried out by means of humidity chamber and the relative humidity of corresponding suction is measured and applied subsequently.

2.2.5 Measurement of Soil Suction

In order to measure the suction developed within soil sample, different approaches are developed during past decades. The relative humidity, indirect and direct matric suction measurements are some of the common approaches for measuring the suction. For measuring the humidity in the pore air, filter paper method (ASTM, D5298-10) and psychrometers are suggested. Indirect measurement of matric suction is performed by means of different methods, such as filter paper, pressure membrane, porous plate (ASTM, D2325-68), time domain reflectometry (Conciani et al., 1996) and heat dissipation sensors. The only method to measure the suction directly is carried out by means of tensiometers (ASTM, D3404-91).

2.3 Porous Medium

In terms of partially saturated soil mechanics, porous media consists of two immiscible substances: water and air. While considering the water regime of porous medium, pore water is separated into three distinct phases according to its potential (Briggs, 1897); Bulk water, water bridges (pendular rings in the case of spherical

particles) and adsorbed water. The adsorbed water is a layer of water coating the surface of particles and its volume is usually negligible. The water bridges are formed in particles contact points due to capillary action. Mainly, the volume of water is attributed to the bulk water in inter-particle zones. Figure 2.4 shows the pore water structures entrapped between particles.

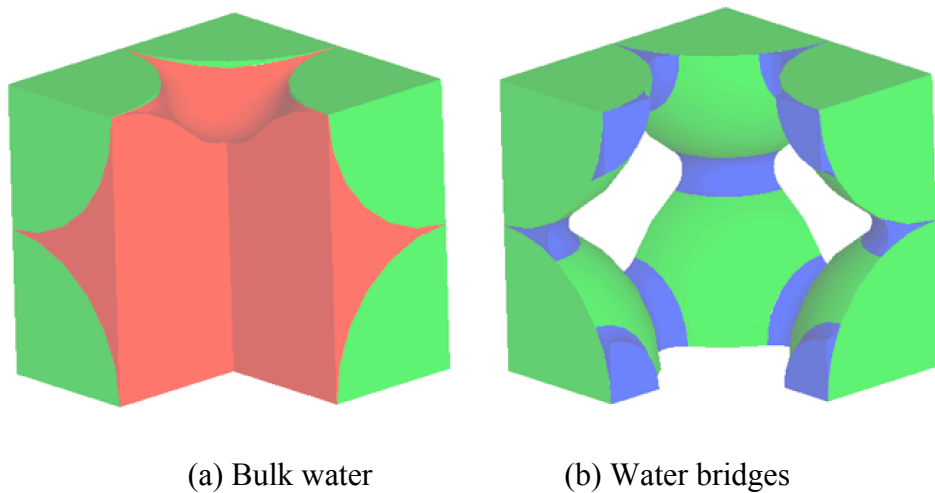


Figure 2.4: The pore water in form of (a) bulk water and, (b) water bridges (Toker, 2002)

2.3.1 Pore-Scale Modeling

During the past decades, in order to obtain the mechanical properties of the soil, various models of porous medium are developed. The earlier theories that developed were assuming the pores as bundle of tubes (Childs and Collis-George, 1950; Fatt and Dykstra, 1951; Burdine, 1953). The idea was to relate the properties of porous media to tube radius frequency distribution but they all fail to represent porous media accurately. The need of accurate description of porous media leads to development of regular network approaches. In regular network approaches, the group of spheres representing the particles are packed in various shapes, such as cubic, hexagonal and rhombohedral packings (Fatt, 1956; Amyx et al., 1960). Chatzis and Dullien (1977)

compared the experimental data with regular network results and observed unrealistic results according to regular networks. For better reflection of porous medium, random networks models were proposed. In 1984, Jerauld et al. applied Voronoi diagrams for better representation of porous media. Later, Blunt et al. (1990) used similar approach but they all fail to capture any of statistics associated with porous medium. Application of networks derived from real porous medium was put forth by Bryant et al. (1992 and 1993). The purposed methods were considering equally sized sphere packing leading to need of more accurate approaches. Pore-network models have been most commonly developed to predict the permeability of materials from microstructural geometry (Bryant et al., 1993; Thompson and Fogler, 1997; Hilpert et al., 2003; Abichou et al., 2004), but have also been extended to include multiphase flow effects (Bryant et al., 1992; Piri and Blunt, 2005). The volume decomposition of pore-scale can be implemented with application of classical Delaunay triangulation (dividing a space among points of interest) and their dual Voronoi graphs (Bryant and Blunt, 1992; Bryant and Johnson, 2003; Thompson and Fogler, 1997). Regular Delaunay triangulation (Edelsbrunner and Shah, 1996) generalizes classical Delaunay triangulation to weighted points, where weights account for the radius of spheres. With application of regular Delaunay triangulation, the pore bodies and their connectivity are defined (Chareyre et al., 2002). The open source software Yade (Smilauer et al., 2010) contains the packages of network models and meanwhile C++ library CGAL (Boissonnat et al., 2002) can be used for the Delaunay triangulation procedure.

In past few years, for description of porous medium, 3D voxel based methods were developed. According to 3D voxel concept, a single sample or data point is represented on 3D space. The X-ray microtomography, object-base modeling, Gaussian technique and simulated annealing are only few methods that utilized this concept. The X-ray microtomography (Dunsmuir et al., 1991; Spanne et al., 1994) is applicable due to X-ray absorption differences in solid matrix and pore spaces. Reconstructing a porous media with this method requires special scanners, which are costly. The need for cheaper methods resulted in formation of Gaussian field

technique. By implementation of image analysis of the 2D section, the porosity and correlation functions are acquirable. In regard to these methods, the algorithms for reconstructing the pore space are mostly stochastic. A thorough review on these methods is presented in Adler et al. (1998) paper. These methods fail to capture the underlying particulate structures of pore space. Later, in 1998, Yeong et al. proposed stochastic methods using simulated annealing. In this method additional correlation functions like particle size distribution functions, are integrated and by moving the pore-space voxel, minimized objective functions are obtained. Incorporating more factors will result in better assumption of the porous medium, but it will be costly and time consuming. The object-based technique is presented for actual simulation of particles. Various works are combined for this purpose. Packing algorithms for spheres are presented by Adler et al. (1998) and arbitrary shapes are established by different scientists (Coelho et al., 1997; Pilotti, 2000; Latham et al., 2001 & 2002). In the past few years, the combination of above mentioned methods are considered. Thovert et al. (2001) and Hilfer (2002) developed a method using statistical and object-based approaches.

2.3.2 Packing of Uniform Spheres

As mentioned in section 2.3.1, one of simplest methods of pore-scale modeling is to pack the particles of a representative size in various arrangements. This will lead to determination of volume and shape of porous medium between particles. The most commonly analyzed sphere packings are cubic, hexagonal and rhombohedral packing.

2.3.2.1 Cubic Packing

The cubic packing for identical spheres is the simplest method to represent the pore scale medium. In order to establish this form of packing, each sphere has six tangent neighbors and each of these tangent neighbors has centers at orthogonal positions to one another (Figure 2.5).

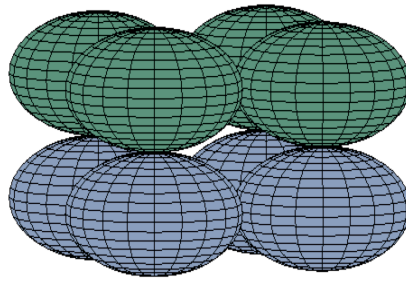


Figure 2.5: Cubic packing

By adjusting the distances between the spheres, the pore volume between the particles can be increased.

2.3.2.2 Hexagonal Packing

In order to present more realistic form of packing and decrease the void ratio of model, the hexagonal packing is developed. In this form of packing the bottom layer is packed similar to cubic packing while the upper layer of spheres are located within the gaps developed in lower layer. Figure 2.6 illustrates the simple hexagonal packing. The volume and density of medium can be calculated by means of geometry.

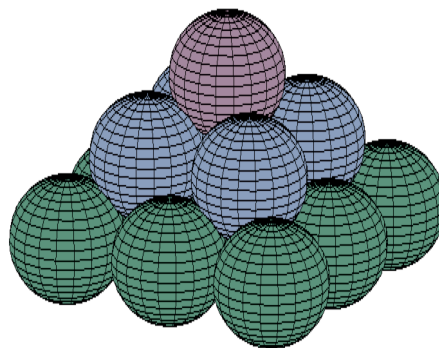


Figure 2.6: Hexagonal packing

2.3.2.3 Rhombohedral Packing

The need for denser packing resulted in formation of rhombohedral packing model. In this form of packing, the pore throat is defined with three sphere-to-sphere contacts, while in cubic packing four sphere-to-sphere contacts exist. This form of packing will decrease the porosity and permeability of medium in comparison with previous form of packings. Figure 2.7 depicts the simple example of rhombohedral packing.

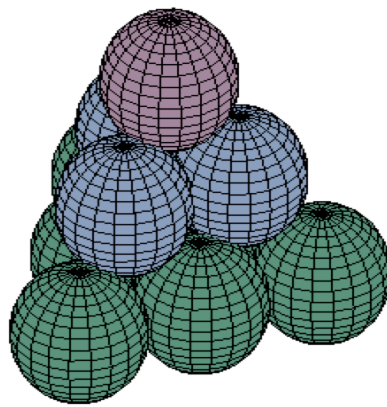


Figure 2.7: Rhombohedral packing

2.3.3 Pendular Rings

The water that has been collected around the particle-to-particle contact points of a material forms a water bridge, which in the case of spherical particles is called pendular rings. Figure 2.8 shows a torus pendular ring, which has been developed between two spherical particles. Throughout the past century, attention developed in determination of shape and volume of pendular rings as well as measuring the tensile forces among particles. In 1968, Clark et al. came to the conclusion that surface of pendular rings are not circular. In mathematical terms, pendular rings can be shown as distorted catenoids (Briggs, 1897).

In order to find the volume of pendular rings, various assumptions are made during past century. Some methods considered meniscus of pendular rings as circular arc (Pietsch et al., 1967) others considered geometry of equal sized spheres (Melrose, 1966; Lian et al., 1993; Pierrat, 1997; Urso et al., 1999). Even assumption of zero contact angles is considered (Kruyer, 1958; Cross et al., 1963; Erle et al., 1971; Rabinovich, 2005).

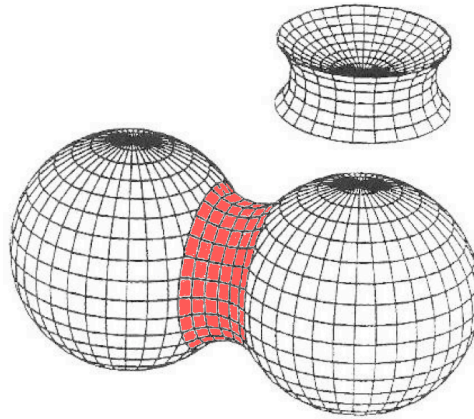


Figure 2.8: Torus pendular ring (Sjoblom, 2000)

Theoretically, the volume of pendular ring depends on different factors. The most noticeable ones are: magnitude of induced suction, filling angles (depending on size of spheres) and contact angle in solid-water interface. In 2011, Chen et al. found the volume of pendular rings developed between unequal-sized spheres. In this method the surface of pendular rings are considered to be circular arcs. One of the notable dilemmas that encountered while dealing with pendular rings is to define the passable distance between particles where pendular rings can be formed. In this regard, Lian et al. (1993) theoretically defined maximum distance between equal-sized spheres where pendular rings can be engendered.

2.3.3.1 Volume of Pendular Rings

The volume of pendular rings can be mathematically calculated with assumption in the shape. The pendular rings surface is assumed to be a circular arc. The volume of

pendular rings mainly depends on the magnitude of applied suction, filling angles (ϕ_1 , ϕ_2) and contact angle (θ) between soil particles and water. Figure 2.9 shows a cross-section of pendular ring with two unequal-sized spherical particles. Centers of particles are located at O_1 and O_2 with corresponding radii of r_1 and r_2 . O_3 is a center of the arc of the pendular ring surface and C_1 and C_2 are contact points of the arc with two particles. The A is intersection of two radii. The B_1 and B_2 are projection of points of C_1 and C_2 on X-axis, respectively. The intersection of line O_3B_3 with arc of the pendular ring (C_1C_2) and X-axis are noted with C_3 and B_3 , respectively. The distance between two particles is noted with d .

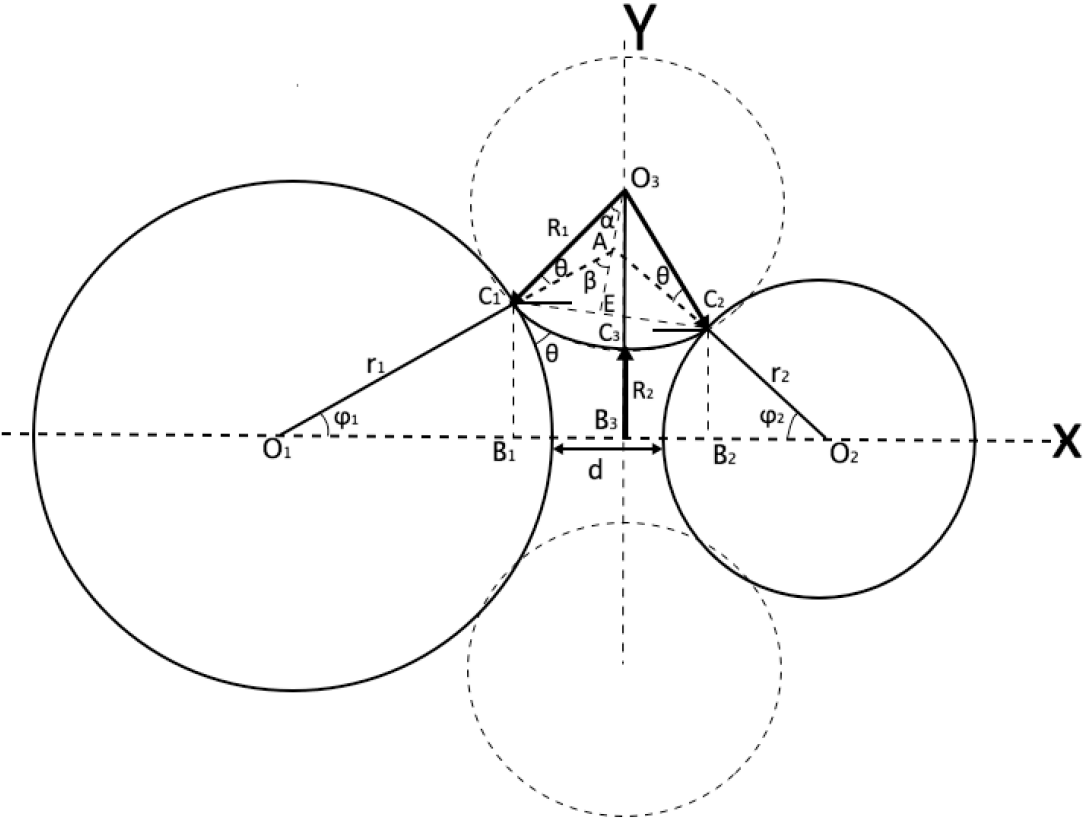


Figure 2.9: Cross-section of pendular ring

By considering the fact that $C_1A=C_2A$ (C_1AC_2 is isosceles triangle), the relation between filling angles will be equal to,

$$O_1A \cdot \sin \varphi_1 = O_2A \cdot \sin \varphi_2$$

$$\frac{\sin \varphi_1}{\sin \varphi_2} = \frac{O_2A}{O_1A} = \frac{r_2 + C_2A}{r_1 + C_1A} \quad (2.17)$$

Therefore,

$$C_1A \cdot \cos \varphi_1 + C_2A \cdot \cos \varphi_2 = d + r_1 + r_2 - r_1 \cos \varphi_1 - r_2 \cos \varphi_2 \quad (2.18)$$

So,

$$C_1A = \frac{d + r_1 + r_2 - r_1 \cos \varphi_1 - r_2 \cos \varphi_2}{\cos \varphi_1 + \cos \varphi_2} \quad (2.19)$$

The combination of Eq. (2.17) and Eq. (2.19) will lead to,

$$\varphi_2 = 2 \arctan \left(\frac{d + 2r_1}{d + 2r_2} \tan \left(\frac{\varphi_1}{2} \right) \right) \quad (2.20)$$

After determining the filling angles, the next step is to find the values of principal radii (R_1 and R_2). R_1 is the radius of circular arc and R_2 is a minimum distance between the pendular ring surface and axis of X. By considering the right triangles of O_3C_1E and AC_1E ,

$$\sin \alpha = \frac{C_1E}{R_1} \quad \& \quad \sin \beta = \frac{C_1E}{C_1A} \quad (2.21)$$

As a result,

$$R_1 \sin \alpha = C_1A \cdot \sin \beta$$

$$R_1 = C_1A \cdot \frac{\sin \beta}{\sin \alpha} \quad (2.22)$$

where, α and β are,

$$\alpha = \frac{\pi - \varphi_1 - \varphi_2 - 2\theta}{2} \quad (2.23)$$

$$\beta = \frac{\pi - \varphi_1 - \varphi_2}{2} \quad (2.24)$$

Arrangement of Eq. (2.19), (2.23) and (2.24) into Eq. (2.22) leads to,

$$R_1 = \frac{d + r_1 + r_2 - r_1 \cos \varphi_1 - r_2 \cos \varphi_2}{\cos \varphi_1 + \cos \varphi_2} \frac{\sin\left(\frac{\pi - \varphi_1 - \varphi_2}{2}\right)}{\sin\left(\frac{\pi - \varphi_1 - \varphi_2 - 2\theta}{2}\right)} \quad (2.25)$$

In order to simplify Eq. (2.25), the angle transformation formulas are utilized.

$$\begin{aligned} \cos(x + y) &= \cos(x)\cos(y) - \sin(x)\sin(y) \\ \tan\left(\frac{x}{2}\right) &= \frac{\sin(x)}{1 + \cos(x)} \end{aligned} \quad (2.26)$$

Hence, R_1 will be equal to,

$$R_1 = \frac{d + r_1(1 - \cos \varphi_1) + r_2(1 - \cos \varphi_2)}{\cos(\varphi_1 + \theta) + \cos(\varphi_2 + \theta)} \quad (2.27)$$

Subsequently, R_2 can be obtained as given,

$$R_2 = r_1 \sin \varphi_1 - R_1(1 - \sin(\varphi_1 + \theta)) \quad (2.28)$$

The volume of pendular ring can be attained by rotation of pendular surface around the X-axis. V_1 is the volume generated by rotation of the arc $C_1C_2C_3$ around the axis of X and V_2 is the part of the volume V_1 that is located inside spherical particles. With assumption of the point B_3 as the origin of coordinate system, the equation of arc $C_1C_2C_3$ can be written as,

$$(X - x_{O_3})^2 + (Y - y_{O_3})^2 = R_1^2 \quad (2.29)$$

where, x_{O_3} is equal to zero and y_{O_3} is sum of principal radii ($R_1 + R_2$). Rearrangement of Eq. (2.29) will result in,

$$Y^2 = y_{O_3}^2 + R_1^2 - X^2 - 2y_{O_3}\sqrt{R_1^2 - X^2} \quad (2.30)$$

The volume of V_1 is given by,

$$V_1 = \int_{x_1}^{x_2} \pi Y^2 \cdot dX \quad (2.31)$$

Where;

$$x_1 = -B_1B_3 = -R_1 \cos(\varphi_1 + \theta)$$

$$x_2 = B_2B_3 = R_1 \cos(\varphi_2 + \theta)$$

Solving Eq. (2.31) will result in the volume of V_1 as written,

$$\begin{aligned} V_1 = & \pi(y_{O_3}^2 + R_1^2)R_1(\cos(\varphi_1 + \theta) + \cos(\varphi_2 + \theta)) - \frac{\pi}{3}R_1^3(\cos^3(\varphi_1 + \theta) + \cos^3(\varphi_2 + \theta)) - \\ & - 2\pi y_{O_3}^2 R_1^2(\sin(\varphi_1 + \theta)\cos(\varphi_1 + \theta) + \sin(\varphi_2 + \theta)\cos(\varphi_2 + \theta)) + 2\pi y_{O_3}^2 R_1^2(\varphi_1 + \varphi_2 + 2\theta - \pi) \end{aligned} \quad (2.32)$$

V_2 can be obtained using the volume of spherical cap as given in Eq. (2.33). Figure 2.10 shows a spherical cap with height of h .

$$V_{\text{cap}} = \frac{\pi h^2}{3}(3r - h) \quad (2.33)$$

Regarding to Figure 2.9, the height of the cap for the first and second spheres are equal to,

$$h_1 = r_1(1 - \cos \phi_1) \quad \& \quad h_2 = r_2(1 - \cos \phi_2) \quad (2.34)$$

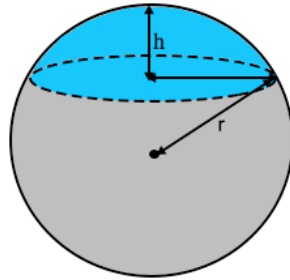


Figure 2.10: Spherical cap

As a result, the volume of V_2 is obtained as,

$$V_2 = \frac{\pi}{3}(r_1^3(2 - 3\cos \phi_1 + \cos^3 \phi_1) + r_2^3(2 - 3\cos \phi_2 + \cos^3 \phi_2)) \quad (2.35)$$

Finally, the volume of pendular ring (V) is obtained by subtracting V_1 from V_2 as given by.

$$V = V_1 - V_2 \quad (2.36)$$

2.4 Drainage

Natural ability of the soil to allow passage of water through it is called soil drainage. The rate that water will drain away through the soil is related to its porosity, which is influenced by the texture and structure of the soil. Dense soils in comparison with loose soils will hold water and passage of water will be slower.

2.4.1 Drainage Models

For many years, attention developed to model the drainage process of porous medium. In a basic representation of porous medium, pores are modeled using capillary tubes with different diameters (Levine et al., 1974; Bear et al., 1992). Alternatively, various approaches are emerged considering the assumptions in shape of pores. In 1972, Mason assumed that the shape of pores is tetrahedral and drainage is linked to curvature of faces of tetrahedron. Alternatively, researchers considered regular packings of spheres in porous medium as discussed in section 2.3.2. Fisher (1926) defined a matrix containing regularly packed identical spheres and ascribed volume of water to tensile forces generated within porous medium.

Computers allowed researchers to directly simulate the developed forces on, and movement of, each particle in a granular medium, leading to Discrete Element Methods (DEM) (Cundall, 1971). In DEM, each particle in a granular system is modeled as a geometrically simplified object that interacts with other objects through surface contact. Particles are typically considered to be rigid, while the contact points are allowed to deform according to some force-deformation law. At each iteration, objects in contact are distinguished and their contact forces resolved. Afterwards, their positions updated through Newton's second law (Cook et al., 2004).

While many research institutes proposed their own algorithms (Williams and O'Connor, 1995; Gardiner and Tordesillas, 2000), commercial computer programs, such as Particle Flow Code, which models movement and interaction of assemblies of arbitrarily sized particles (Itasca, 1999), are developed. DEM simulations almost always focused on small water contents and pendular ring effects when they aimed to simulate unsaturated granular soils. An example would be Liu et al.'s (2003) two dimensional simulation based on viscoelastic solid behavior at the contacts between rigid circular particles.

While DEM diminishes the up-scaling problem in micromechanics, a new issue of how to realistically define the system at a particle level at manageable complexity arises. Nonetheless, DEM is the only way to capture some very real aspects of granular materials, such as load bearing particle chains stabilized by the rest of the particles (Oda, 1974).

2.4.2 Air Entry Pressure

The neck of a pore, which is known as pore throat, has smallest hydraulic radius along the pore and when air-water interface passes this location, the rest of the pore can be drained easily. The air entry pressure can be defined as the amount of matric suction from which air starts to penetrate into pores (Corey, 1977). The air entry pressure is also called air entry value or bubbling pressure. The AEP can be predicted by considering the capillary rise in a tube with diameter equal to the D_{10} of the soil.

$$AEP = \frac{4\sigma_{st}}{D_{10}} \quad (2.37)$$

A better approximation of AEP is carried out by Toker (2002) as given by,

$$AEP(\text{kPa}) = \frac{0.75(\text{kPa}\cdot\text{mm})}{D_{\text{average}}(\text{mm})} \quad (2.38)$$

where, D_{average} is mean diameter of soil sample.

In experimental approaches, the air entry value of porous disks is considered and measured using Kelvin's equation as,

$$AEP = \frac{2\sigma_{st}}{R_s} \quad (2.39)$$

where, R_s is radius of pore channel in disks. As it can be observed from all of the above-mentioned equations, the AEP of a porous medium depends on size of particles and subsequently, on size of the pore in narrowest passages.

2.4.3 Pore-Scale Drainage

Inside a saturated media, when suction exceeds the AEP of media, the bulk waters start to drain. Once the bulk water is drained, the remaining water in pores will be in the form of liquid bridges (pendular rings) and adsorbed water. With application of higher suctions, liquid bridges also start to diminish and the only remaining pore water will be adsorbed water, which are not likely to drain in atmospheric conditions. Figure 2.11 represents the water in a single pore entrapped between particles. In the case of saturated condition the air water interface will be located at level (1). With increasing the suction, the curvature of air-water surface will increase till the moment that reaches equilibrium ((2), (3)). While considering the air water interface at level (4), which is a pore throat, if the equilibrium cannot be satisfied, the air will penetrate into pore medium and pore water will be drained.

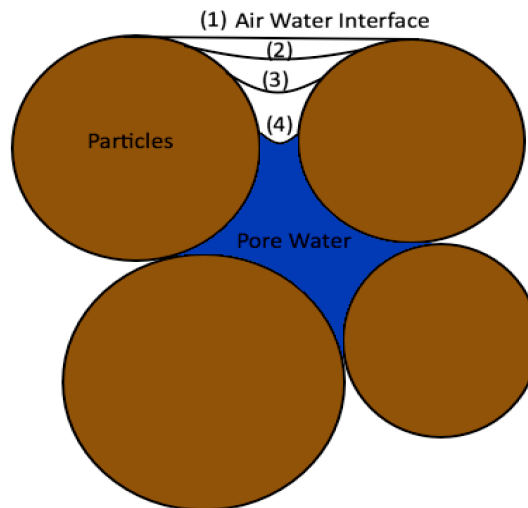


Figure 2.11: Drainage of pore water

2.5 Soil Water Characteristic Curves

The water characteristic of soils is a fundamental property of the partially saturated soils and is presented in form of a graph known as soil water characteristic curves (SWCC). Basically, it defines as a relation between the volume or mass of the retained water in a soil sample with corresponding matric potential (soil suction). The SWCC are also called soil moisture characteristic curves (SMC) or soil water retention curves.

The importance of SWCC is due to their direct relation with hydraulic properties of soils, which are extremely variable with variation of the size, and connectivity of pore media. Therefore, a different soil structure or texture will result in a distinct SWCC and eventually a distinct hydraulic behavior of soil. These curves are essential in understanding the movement of contaminants within the soil media and also in water management. The implementations of SWCC are not just limited to geotechnical engineering and are widely utilized in agricultural engineering. The agricultural engineers use SWCC to obtain the amount of water required for each type of plants by considering the suction applied by roots of plants inside the soil medium.

By increasing the applied suction, the total amount of drained water from pore medium will increase. Figure 2.12 represents the differences of SWCC between fine and coarse textured soils. Fine textured soils require higher suctions to discharge the water from pore. The AEP and residual water content points of both SWCC are also illustrated in Figure 2.12. The residual water content corresponds to a suction value where all bulk waters is drained. In this point, the water volume comprises of liquid bridges (pendular rings) and adsorbed water.

The SWCC is generally used for conducting seepage analysis and determining different properties of soil, such as unsaturated shear strength parameters (Vanapalli et al., 1996), hydraulic properties (Millington et al., 1961; Mualem, 1976; Fredlund et

al., 1993) and relation of degree of saturation with coefficient of aqueous diffusion of unsaturated soils (Lim et al., 1998).

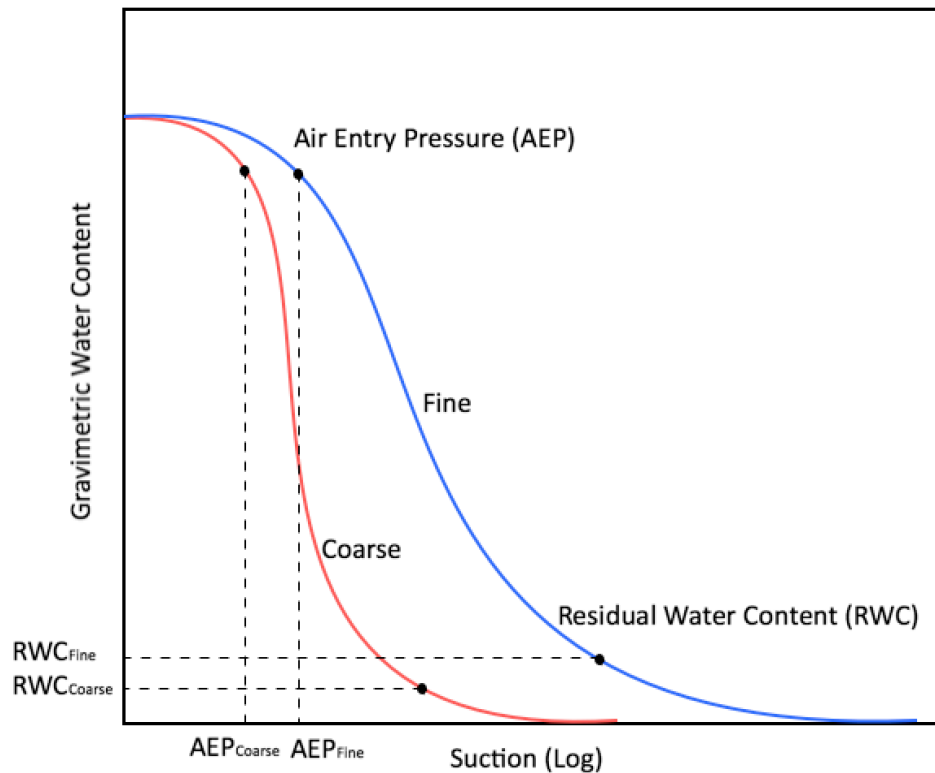


Figure 2.12: SWCC of fine and coarse soils

2.5.1 Hysteretic Effect

The water characteristics of soils are hysteretic. In a given suction the amount of water for a wetting path is less than that for a drying path. Following factors leads in this inequality:

- 1) Irregularity in cross-section of void pathway or the ink-bottle effect (Haines, 1927)
- 2) Greater contact angle in an advancing meniscus

3) Entrapped air which has different volume when suction is increasing or decreasing

In most cases of civil or agricultural engineering, SWCC are assumed to be non-hysteretic due to difficulties in measurements of hysteretic curves, which are time consuming. Figure 2.13 shows the differences of SWCC between drying and wetting phases. Naturally, the SWCC of soil in nature is located between wetting and drying curves.

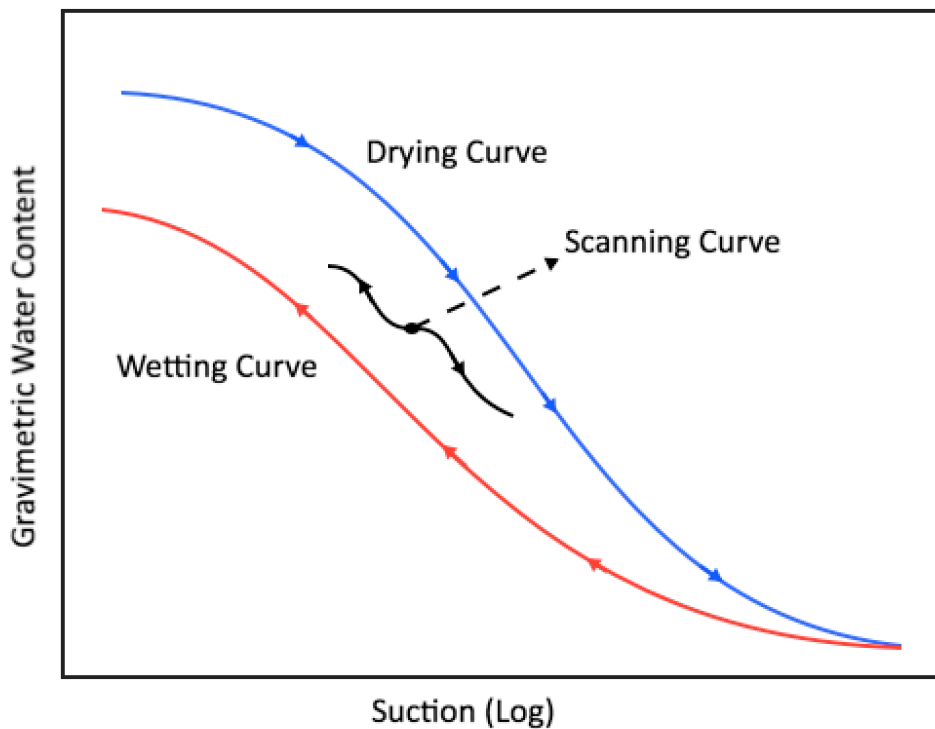


Figure 2.13: Hysteretic effect

2.5.2 Laboratory Measurement Techniques

In 1907, Buckingham proposed the first SWCC. The SWCC can be obtained in laboratory by conducting various kind of tests. The most common approaches are based on measuring discrete points, such as hanging column, pressure chamber, chilled mirror hygrometer and centrifuge methods (ASTM, D6836-02). But there are

also continuous measurements techniques, such as measuring in-out flow in an axis translation setup (Wildenschild et al., 1997), or the MIT method of evaporating on a digital balance (Toker et al., 2004). Only the Methods from which we use data are explained in this section.

2.5.2.1 Hanging Column

In the hanging column approach (Vomocil, 1965), the water inside the saturated sample is subjected to a tension with the weight of hanging water below it. In order to measure the applied suction, manometers are utilized. This method is applicable for lower suctions upto 80 kPa. The time required for equilibrium to be reached in air-water interface is highly dependent on permeability of soil sample, and may take hours or days. Figure 2.14 illustrates the setup of hanging column method.

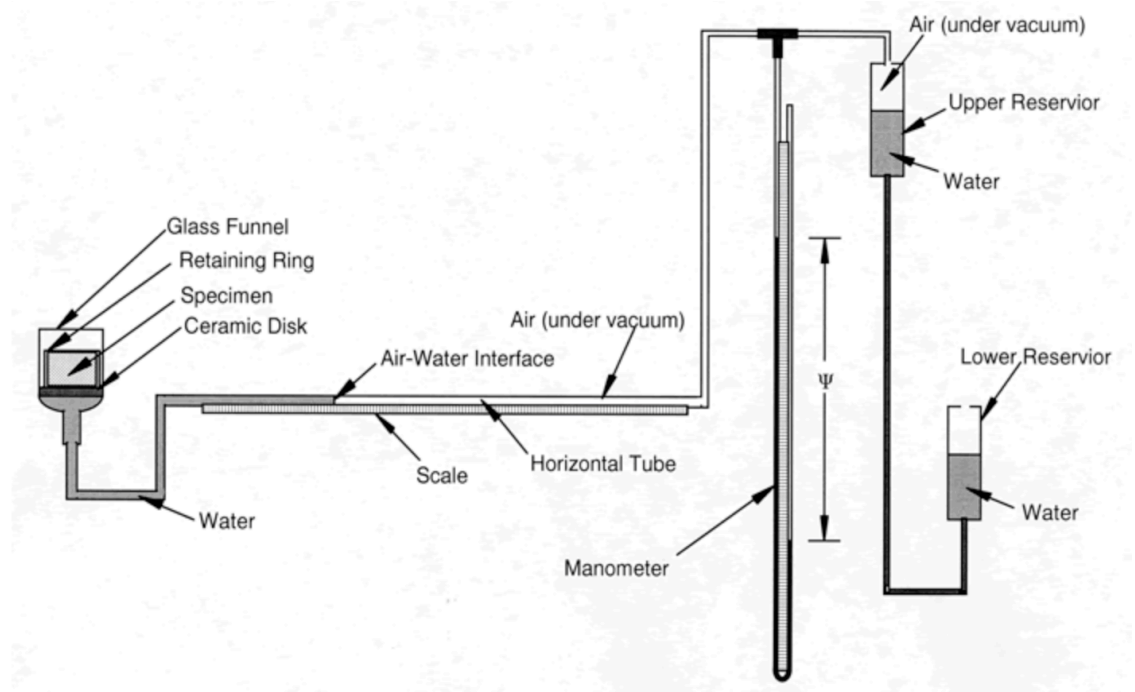


Figure 2.14: Schematic of hanging column setup (ASTM, D6836-02)

2.5.2.2 Pressure Chamber

In this technique, which is the most common SWCC measurement method, the soil specimen is located inside a chamber and air pressure is induced gradually. The specimen is located on a ceramic porous disk and by increasing the pressure inside the chamber amount of drained water is measured. The process will be continued until the cessation of water flow. This method is suitable for suctions lower than 1500 kPa. Figure 2.15 shows the schematic of pressure chamber setup

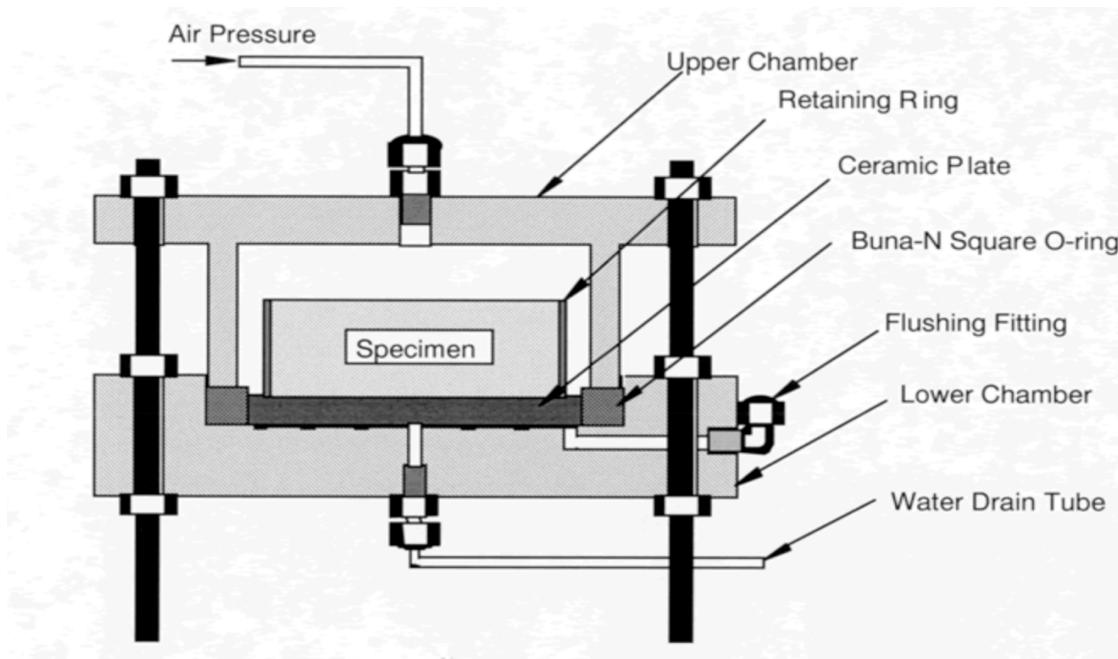


Figure 2.15: Schematic of pressure chamber setup (ASTM, D6836-02)

2.5.2.3 MIT Method

One of the best approaches for obtaining continuous SWCC is known as MIT method, which is developed in 2000 by Sjöblom. In this approach the tensiometers are used because of their ability to directly measure the suction. Reduction of the required time and its ability to result continuous curves are some of the advantages that come along

with this approach. Later, in 2002, Toker proposed improvements in this method, which resulted in more reliable results (Toker et al., 2004). Figure 2.16 depicts the schematic of MIT method setup.

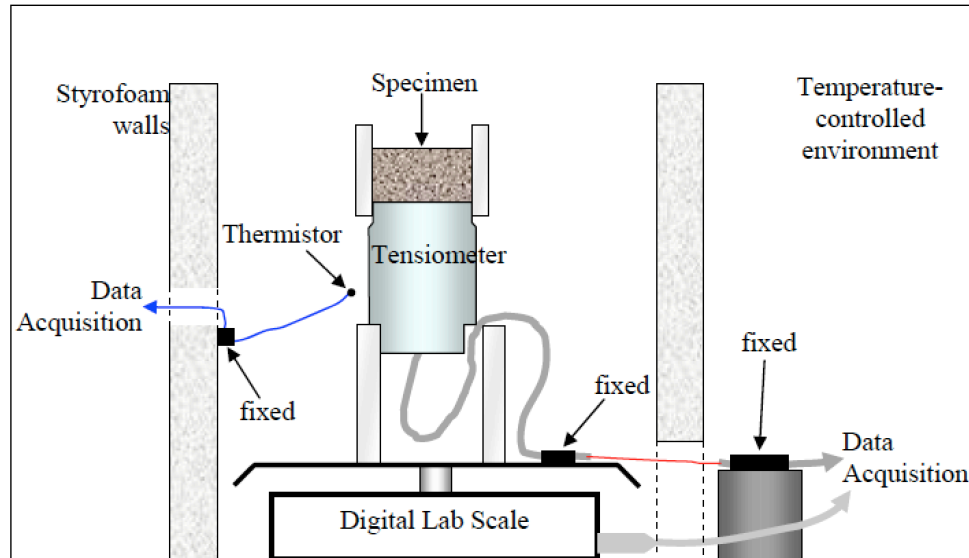


Figure 2.16: Schematic of MIT method setup (Toker, 2007)

2.5.3 Empirical Methods for Predicting the SWCC

2.5.3.1 Fitting Curves

In past few decades, scientists have been utilizing the available SWCC data and proposed an empirical equation that fits into these data points. With application of regression analysis in these methods, analytical equations that can fit to data points are extracted (Gardner, 1958; Brooks et al., 1964; Mualem, 1976; Van Genuchten, 1980; Williams et al., 1983; Fredlund and Xing, 1994; Vereecken et al., 1989; Perera et al., 2005).

Earlier methods of curve fitting techniques were only satisfying uniform soils. As time passed, bimodal and multimodal approaches for obtaining the SWCC of gap-graded

soil structures are proposed. In 2005, Zhang et al. considered multimodal form of SWCC as a combination of smaller unimodal SWCC. Recently, Li et al. (2014) proposed a general bimodal equation considering dual-porosity structure of porous media.

2.5.3.2 Estimation Techniques

Estimation techniques are developed to eliminate the cost and time required to conduct laboratory experiments. The methods considering physical properties of soils, such as particle size distribution (PSD) data to form empirical equations are known as physico-empirical methods (Gupta and Larson, 1979; Arya and Paris, 1981; Fredlund and Wilson, 1997). The Pedo-Transfer functions (PTF) (Bouma, 1989) are also implemented in acquiring SWCC. These functions use the available soil survey data to predict the SWCC of different type of soils. Alternatively, while considering artificial intelligence methods, such as genetic programming and neural networks, SWCC are estimated by training the model with available database (Pachepsky et al., 1996; Koekkoek and Booltink, 1999; Johari et al., 2006).

The most common approaches for estimating SWCC while using PSD data are proposed by Arya and Paris (1981) as well as Fredlund and Wilson (1997).

2.5.3.2.1 Arya and Paris (1981) Method

While considering the physico-empirical methods, Arya and Paris (1981) method is one of the first methods that used particle size distribution data and bulk density for deriving soil water characteristic curves. This method converts particle size distribution data to a pore size distribution data. Following this, an empirical procedure integrated for finding the parameter noted as α using available soil moisture characteristic curves. In this method, particle size distribution curve is divided into small segments and each segment is considered as a single pore. The volume of each pore is calculated by using mass proportion of each segment and

particle density.

$$V_{v_i} = \frac{W_i}{\rho_p} \cdot e, \quad i=1,2, \dots, n \quad (2.40)$$

where, V_v is volume of i^{th} pore, W_i is solid mass per unit sample mass in i^{th} range, ρ_p is particle density and e is void ratio.

The volumetric water content of each segment is calculated using the attained pore volumes.

$$\theta_{v_i} = \sum_{j=1}^{j=i} \frac{V_{v_j}}{V_b}, \quad i=1,2, \dots, n \quad (2.41)$$

where, V_b is,

$$V_b = \frac{1}{\rho_b}$$

And ρ_b is bulk density of considered soil structure. The total amount of particles in each segment (n_i) is determined by,

$$V_{p_i} = n_i \frac{4}{3} \pi R_i^3 = \frac{W_i}{\rho_p} \quad (2.42)$$

where, V_p is total volume of solids in each particle size range, and R_i is mean radius of particles in i^{th} range.

The mean pore radius in i^{th} particle range is given by,

$$r_i = R_i \left(\frac{4 \cdot e \cdot n_i^{(1-\alpha)}}{6} \right)^{0.5} \quad (2.43)$$

where, α is obtained empirically. After obtaining the mean pore radius of each segment, the equivalent soil water pressure (ψ_i) is obtained using the capillary equation.

$$\psi_i = \frac{2\sigma_{st} \cos\theta}{\rho_w \cdot g \cdot r_i} \quad (2.44)$$

where, σ_{st} is surface tension, θ is contact angle, ρ_w is density of water, and g is the acceleration due to gravity.

Eventually, the SWCC is estimated based on volumetric water content (Eq. 2.41) and equivalent soil water pressure (Eq. 2.44) of each segment.

2.5.3.2.2 Fredlund and Wilson (1997) Method

In order to estimate SWCC, Fredlund and Wilson (1997) developed an empirical equation (Eq. 2.45), which fits into particle size distribution (PSD) curve. By dividing PSD into small uniform segments and using SoilVision database for uniform soils, they managed to predict the SWCC of wide range of soils. This method is implemented into SoilVision knowledge base system.

$$P_p(d) = \frac{1}{\ln \left[\exp(1) + \left(\frac{g_a}{d} \right)^{g_n} \right]^{g_m}} \left[1 - \frac{\left[\ln \left(1 + \frac{d_r}{d} \right) \right]^7}{\left[\ln \left(1 + \frac{d_r}{d_m} \right) \right]^7} \right] \quad (2.45)$$

Where;

d = Particle diameter (mm)

d_r = Residual particle diameter (mm)

d_m = Minimum particle diameter (mm)

g_a = Fitting parameter corresponding to the initial break in PSD curve

g_n = Fitting parameter corresponding to the maximum slope of PSD curve

g_m = Fitting parameter corresponding to the curvature of PSD curve

P_p = Percent passing a given particle diameter

2.6 Numerical Methods

In this research, in order to determine the AEP of pore throats, finite difference approximation and Newton-Raphson (Jacobian) method are utilized. Brief description of these methods as well as Taylor series are given in following sections.

2.6.1 Taylor Series

The concept of Taylor series is formally introduced by Taylor (1715). In general, Taylor series is a series expansion of a function about a point. A one dimensional Taylor expansion of a function $f(x)$ about a point $x=x_0$ is given by,

$$f(x) = f(x_0) + \frac{\partial f(x_0)}{\partial x}(x - x_0) + \frac{\partial^2 f(x_0)}{\partial x^2 \cdot 2!}(x - x_0)^2 + \dots + \frac{\partial^n f(x_0)}{\partial x^n \cdot n!}(x - x_0)^n \quad (2.46)$$

where, $\frac{\partial^a f}{\partial x^a}$ is partial derivative of f in respect to x with order of $1, \dots, n$.

2.6.2 Newton-Raphson Method

The Newton-Raphson method (1690) is a powerful technique for solving equations numerically and it's based on linear approximation. The idea of this method starts with assumption of initial guess on a nonlinear function and finding the intercept of

tangent line with considered axis. Iterating the process will result in better answers regarding to root of the function. For a start, lets consider x_0 as an initial guess for the equation of $f(x)=0$ with root of r . From x_0 a better estimation of x_1 is calculated and by iteration of this procedure, closer answer to root value of r is obtained. For iteration of Newton-Raphson lets consider h as the difference between true value of r and initial guess of x_0 . By using Taylor expansion given in Eq. (2.46), Eq. (2.47) is derived.

$$0 = f(r) = f(x_0 + h) \approx f(x_0) + h \frac{\partial f}{\partial x}(x_0) \quad (2.47)$$

Therefore,

$$r = x_0 - \frac{f(x_0)}{\frac{\partial f}{\partial x}(x_0)} \quad (2.48)$$

As a result, the improved estimate x_1 over x_0 can be calculated using following equation,

$$x_1 = x_0 - \frac{f(x_0)}{\frac{\partial f}{\partial x}(x_0)} \quad (2.49)$$

And similarly the successive estimates can be calculated with general equation as written below,

$$x_{n+1} = x_n - \frac{f(x_n)}{\frac{\partial f}{\partial x}(x_n)} \quad (2.50)$$

Eq. (2.50) is applicable for single variable equations. By implementing the Jacobian matrix, the Newton-Raphson method is extended to solve systems of multivariable

functions. With considering the vector X consist of x_1, x_2, \dots, x_n as independent variables and vector $F(X)$ containing the functions $f_i(x_1, x_2, \dots, x_n)=0$, the Jacobian matrix (J) can be written as partial derivatives of functions as,

$$J = \frac{\partial(f_1, f_2, \dots, f_n)}{\partial(x_1, x_2, \dots, x_n)} = \begin{bmatrix} \frac{\partial f_1}{\partial x_1} & \dots & \frac{\partial f_1}{\partial x_n} \\ \vdots & \ddots & \vdots \\ \frac{\partial f_n}{\partial x_1} & \dots & \frac{\partial f_n}{\partial x_n} \end{bmatrix} \quad (2.51)$$

where, n is total number of variables. Finally, the Newton-Raphson (Jacobian) equation can be written as,

$$X_{n+1} = X_n - J^{-1} \cdot F(X_n) \quad (2.52)$$

where, J^{-1} is an inverse of Jacobian matrix, and n is number of iteration.

2.6.3 Finite Difference Approximation

This method is one of the simplest and oldest methods for solving differential equations with approximations of derivatives. The appearance of finite difference approximation (FDA) in numerical methods was concurrent with emergence of computers that offered an adequate framework for dealing with complex science problems.

In FDA the domain is partitioned in space and in time and approximations of the solution are computed at each point. In one-dimensional case, the basic concept behind finite difference approach is related to the definition of the derivative of a function, u , at a point where, $x \in \mathbb{R}$,

$$u_x(x) = \lim_{h \rightarrow 0} \frac{u(x+h) - u(x)}{h} \quad (2.53)$$

And when h tends to zero, the quotient on the right-hand side of equation will provide a close approximation to the exact value of the derivative. By decreasing the magnitude of h better approximations will be computed. While considering the Taylor expansion given in Eq. (2.46), if $u(x)$ have n continuous derivatives over the space of a and b , in a range of $a < x_0$ and $x_0 + h < b$, then,

$$u(x_0 + h) = u(x_0) + h \frac{\partial u(x_0)}{\partial x} + h^2 \frac{\partial^2 u(x_0)}{\partial x^2 \cdot 2!} + \dots + h^{n-1} \frac{\partial^{n-1} u(x_0)}{\partial x^{n-1} \cdot (n-1)!} + O(h^n) \quad (2.54)$$

where, $O(h^n)$ is unknown error, and n is power of error. With approximation on right side of Eq. (2.54) the following relation can be written,

$$u(x_0 + h) = u(x_0) + h \frac{\partial u(x_0)}{\partial x} + O(h^2) \quad (2.55)$$

Rearranging Eq. (2.55) and neglecting the error term results in,

$$\frac{\partial u(x_0)}{\partial x} = u_x(x_0) \approx \frac{u(x_0 + h) - u(x_0)}{h} \quad (2.56)$$

The power of error determines the order of finite difference. Therefore, Eq. (2.56) is known as first order finite difference approximation for $u_x(x_0)$. It's also can be named as first order forward approximation when $h > 0$. In a similar procedure, backward approximation will be,

$$u(x_0 - h) = u(x_0) - h \frac{\partial u(x_0)}{\partial x} + O(h^2) \quad (2.57)$$

As a result,

$$u_x(x_0) \approx \frac{u(x_0) - u(x_0 - h)}{h} \quad (2.58)$$

Subtracting Eq. (2.55) from Eq. (2.57) will result in central approximation of $u_x(x_0)$.

$$u(x_0 + h) - u(x_0 - h) = 2h \frac{\partial u(x_0)}{\partial x} + \frac{h^3}{3} \frac{\partial^3 u(x_0)}{\partial x^3} + O(h^5) \quad (2.59)$$

Rearranging of Eq. (2.59) and considering the highest value of error by minimum order of h gives,

$$u_x(x_0) \approx \frac{u(x_0 + h) - u(x_0 - h)}{2h} \quad (2.60)$$

Interpretation of the equations indicates that central difference approach has an error order of $O(h^2)$ while forward and backward approaches had an error order of $O(h)$ and since $h^2 < h$, using the central formula will result in better approximations. Similarly, obtaining forward, backward and central second derivatives (u_{xx}) requires expansion of Taylor series including terms up to $O(h^5)$ and will result in following equations for central approximation,

$$u_{xx}(x_0) \approx \frac{u(x_0 + h) - 2u(x_0) + u(x_0 - h)}{h^2} \quad (2.61)$$

, Forward approximation,

$$u_{xx}(x_0) \approx \frac{u(x_0 + 2h) - 2u(x_0 + h) + u(x_0)}{h^2} \quad (2.62)$$

, And backward approximation.

$$u_{xx}(x_0) \approx \frac{u(x_0) - 2u(x_0 - h) + u(x_0 - 2h)}{h^2} \quad (2.63)$$

It is also possible to obtain forward and backward FD approximations of the first derivative with second order errors to minimize the existing error. Their equations are given below, respectively.

$$u_x(x_0) \approx \frac{-u(x_0 + 2h) + 4u(x_0 + h) - 3u(x_0)}{2h} \quad (2.64)$$

$$u_x(x_0) \approx \frac{u(x_0 - 2h) - 4u(x_0 - h) + 3u(x_0)}{2h} \quad (2.65)$$

Extracting the mixed derivative formula (u_{xy}) requires both partial derivatives of x and y. The partial derivative of $u_y(y_0)$ in the case of central FD approximation is,

$$u_y(y_0) \approx \frac{u(y_0 + h_y) - u(y_0 - h_y)}{2h_y} \quad (2.66)$$

where, h_y is step size in y direction. As a result, mixed derivative can be extracted using Eq. (2.60) and Eq. (2.66) as given by,

$$u_{xy}(x_0, y_0) \approx \frac{u(x_0 + h_x, y_0 + h_y) - u(x_0 - h_x, y_0 + h_y) - u(x_0 + h_x, y_0 - h_y) + u(x_0 - h_x, y_0 - h_y)}{4h_x h_y} \quad (2.67)$$

where, h_x is step size in x direction.

CHAPTER 3

PORE-SCALE MODELING OF DRAINAGE

3.1 Outline

This chapter attempts to establish an accurate drainage model of soil structure in the form of a MATLAB simulation code with incorporating physical properties of soils into simulation process. Particle size distribution (PSD) and void ratio of soils are considered as input of simulation process. To begin with, spherical particles are generated and packed in respect to PSD. The packing process is calibrated by comparing the void ratio (e) of packed medium to that of considered soil sample (e_d). Next, the porous medium is divided into small bulk pores by means of pore throats. By taking into account that pore throats are the interfaces between two bulk pores, the connectivity of bulk pores are distinguished. The volume of bulk pores and pendular rings are calculated subsequently. Afterwards, the AEP of each pore throat are determined by incorporating finite difference approximation with Newton-Raphson approach.

In drainage process, initially, the simulated medium is considered to be saturated and air-water interfaces are located at upper boundary of the defined medium. In order to drain the medium, a constant suction is applied. If applied suction overpasses the AEP value of a pore throat, continuum air will fill into the associated pore and pore water will be drained. Once the air-water interfaces in all pore throats are in equilibrium, the total volume of drained pore water and developed pendular rings are calculated. Subsequently, the suction is increased and same procedure will be repeated till suction reaches the pre-defined maximum value. Finally, the water content of the medium

after each suction increment is illustrated with SWCC. Figure 3.1 illustrates the flow chart of proposed method.

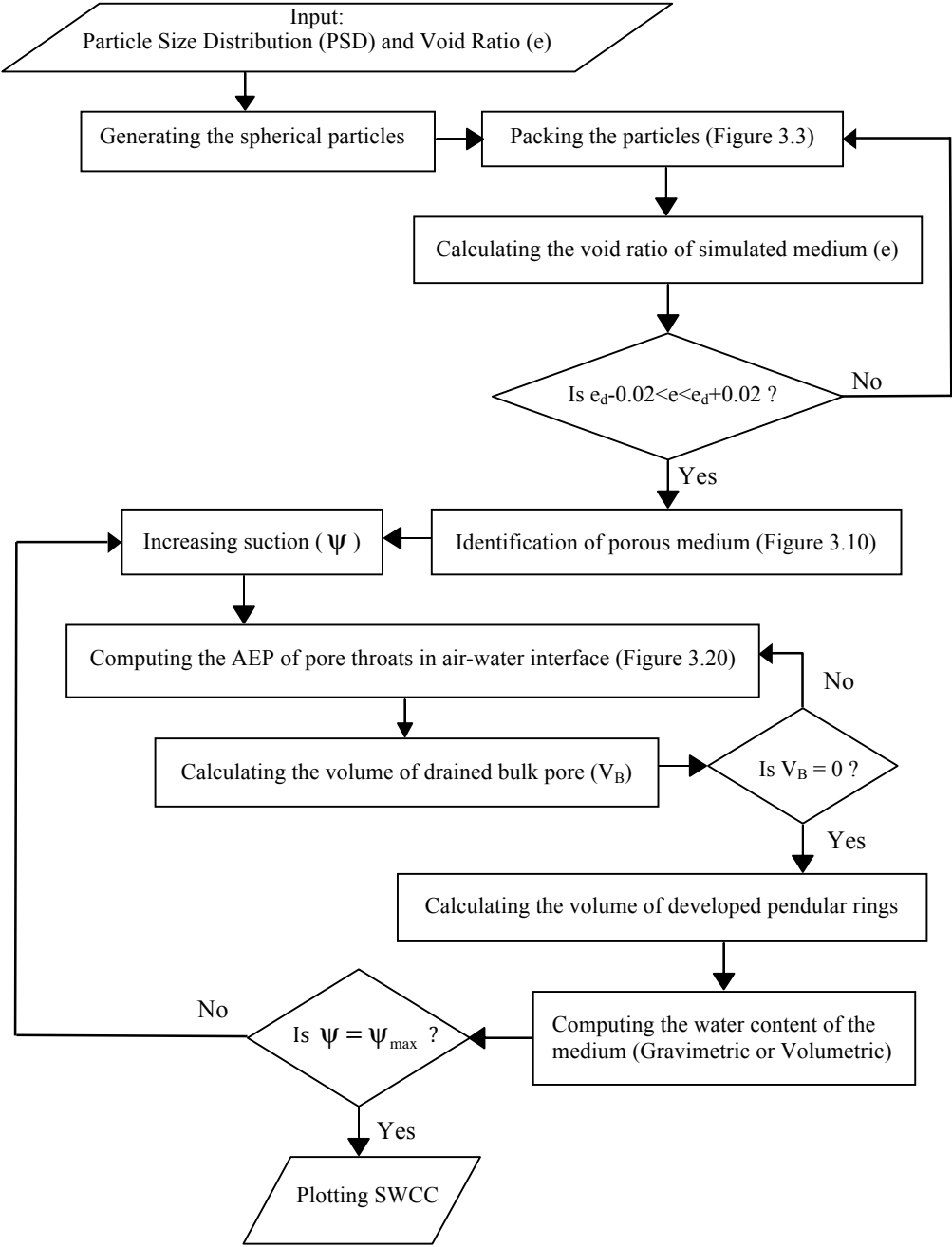


Figure 3.1: Flow chart of proposed algorithm

3.2 Solid Phase of Soil Structure

3.2.1 Generating the Particles

The solid phase of soil consists of different sized particles. In this research, all particles are considered to be spherical. The necessity of a relation between PSD data and total number of particles leads to division of the PSD curve into small segments where the specific gravity of all segments is assumed to be equal. Therefore, the relation between mass (M) and diameter (D) of particles is as follows,

$$M \propto D^3 \quad (3.1)$$

While considering Figure 3.2, which is an arbitrary PSD, and assuming the total number of particles in the coarsest segment (N_1), the total number of particles in each segment with respect to the previous segments is given by,

$$N_i = N_{i-1} \frac{M_i - M_{i+1}}{M_{i-1} - M_i} \left(\frac{D_{i-1} - D_i}{2} \right)^3 \quad (3.2)$$

Where;

$$i = 2, \dots, n$$

n = Total number of segments

M_i = Mass percent for a sieve diameter of D_i

N_i = Total number of particles in the i^{th} segment

The diameter of each particle (d_j) is determined randomly with respect to diameter range of each segment.

$$D_i \leq d_j \leq D_{i+1} \quad (3.3)$$

where, $i=1, \dots, n$, and $j=1, \dots, N_i$.

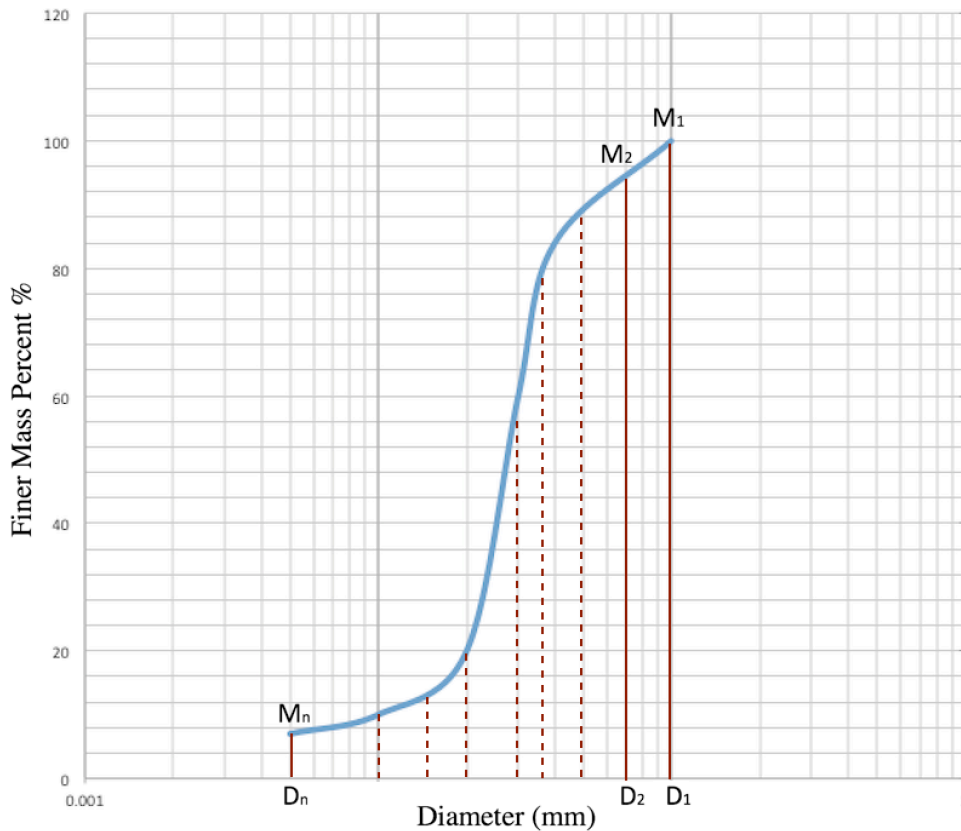


Figure 3.2: Arbitrary PSD and Defined Segments

3.2.2 Packing the Particles

The soil structure is composed of particles and porous medium among the particles. Therefore, an accurate packing of particles will lead to an accurate porous medium. In order to pack the particles, generated particles should be arranged inside a pre-defined medium and desired void ratio of any given soil should be satisfied. The packing procedure of particles can be summarized as follows: (i) arrangement of particles inside a pre-defined medium, (ii) stability control, (iii) application of periodic boundary condition and (iv) iteration process to match the desired void ratio. Figure 3.3 presents the flow chart of packing procedure.

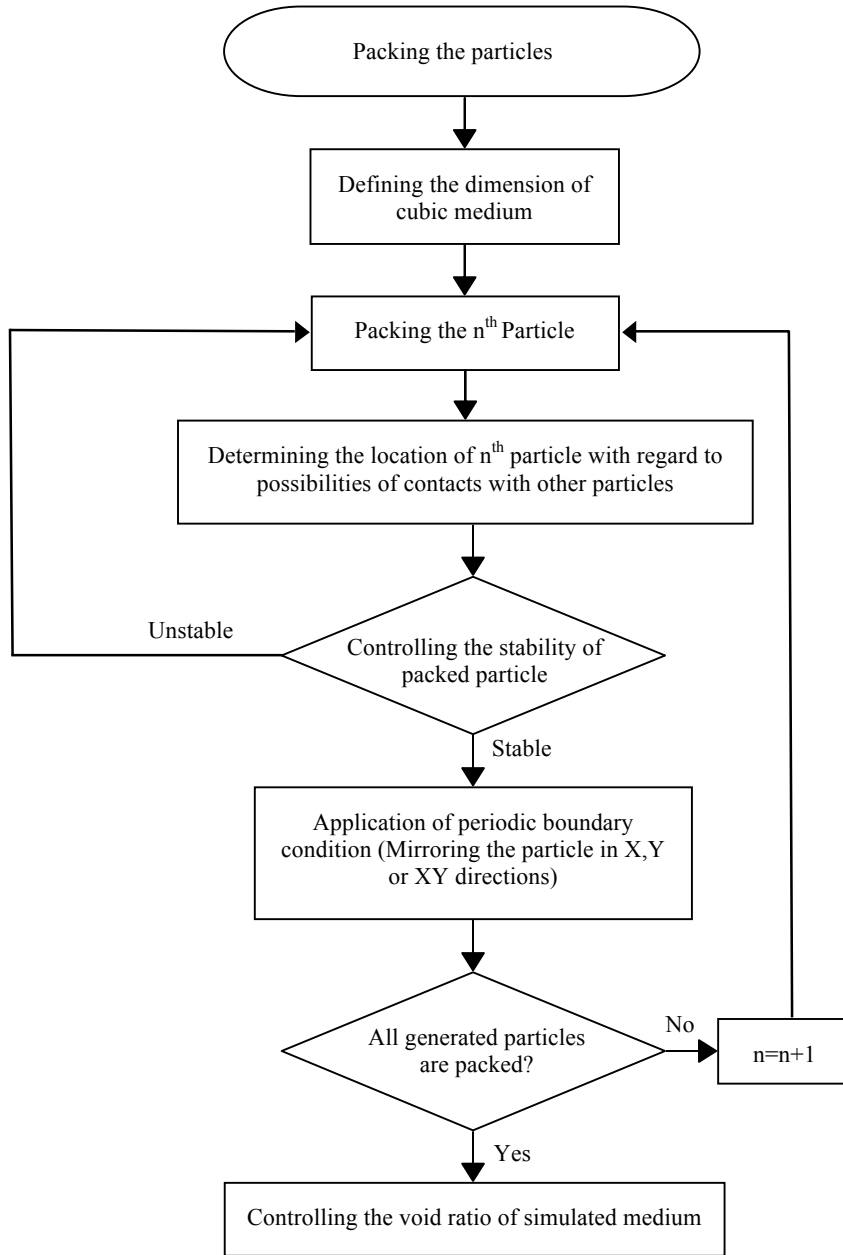


Figure 3.3: Flow chart of particle packing process

3.2.2.1 Particle Arrangement

In order to start with particle packing procedure, domain of the medium in which particles will be placed, should be defined. The volume of the cubic medium is considered to be equal to total volume of particles. As a result of this sizing, fullness

of the domain is ascertained and dimension of the sides of this cubic medium (b) is equal to,

$$b = \sqrt[3]{\sum_{i=1}^N \frac{4}{3} \pi r_i^3} \quad (3.4)$$

where, r_i is radius of each particle, and N is total number of particles. This means there will still be many unplaced particles left when the domain is full. Nevertheless, the algorithm continues to pack particles into the box area higher and higher, but it the end trims this excess portion back to the cubic medium.

In considered Cartesian coordinate (X,Y,Z), particles coordinates are defined with their center points (x,y,z) and radius (r). The upper and lower boundaries of the medium are defined at $Z=b$ and $Z=0$. But, in order to pack all the particles and generate continuous pores in upper and lower boundaries, the range of Z coordinates varies from $Z=2b$ to $Z=-(b/5)$. The primary X and Y coordinates of particles are generated randomly in the range of the medium domain and Z coordinates are controlled in small steps in their defined range. Therefore, the primary coordinate of n^{th} particle is given by,

$$x(n) = \text{Rand} \cdot b \quad (x \in X), \quad y(n) = \text{Rand} \cdot b \quad (y \in Y), \quad z(n) = 2b - m \frac{r(n)}{2} \quad (z \in Z) \quad (3.5)$$

where, $m = 0, \dots, \frac{22b}{5r(n)}$, and $0 \leq \text{Rand} \leq 1$.

The Euclidean distance (E_d) between surface of n^{th} and already packed particles (n-1) is given by,

$$E_d = \sqrt{(x(n) - x(i))^2 + (y(n) - y(i))^2 + (z(n) - z(i))^2} - r(n) - r(i) \quad (3.6)$$

where, $i = 1, \dots, n-1$ ($n \neq 1$). For all m and i values, if E_d remains positive, n^{th} particle will be located at $z(n) = -(b/5)$. Otherwise, at an intersection with i^{th} particle, the procedure will stop and primary Z coordinates of n^{th} particle ($z(n)$) will be attained at colliding point. While arranging the particles inside the medium, particles can encounter different arrangement conditions. These statuses can be categorized according to number of contacts for n^{th} particle.

1) No-Contact

Considered particle (n), has no contact with any other particles. This condition occurs when E_d , which is given in Eq. (3.6), stays positive for all m and i values. The final coordinates of the n^{th} particle in X and Y coordinates will be equal to primary coordinates given in Eq. (3.5), and Z coordinates is $z(n) = -(b/5)$.

2) One-Contact

When n^{th} particle collides with i^{th} particle, according to Eq. (3.6), i^{th} particle is considered to be the first contact for n^{th} particle. It is important to check the availability of other particles in vicinity of a first contact. If n^{th} particle could establish other contacts with other particles, while keeping its first contact with i^{th} particle, the second contact will be formed. For n^{th} particle the procedure is controlled with following equation.

$$F = \sqrt{(x(i) - x(j))^2 + (y(i) - y(j))^2 + (z(i) - z(j))^2} - (r(i) + r(j) + 2r(n)) \quad (3.7)$$

where, i is number of the particle that forms the first contact with n^{th} particle, and $j = 1, \dots, n-1$ ($n \neq 1, j \neq i$). For all j values, if F remains positive, the n^{th} particle cannot form second contact with j^{th} particle, which is the case in One-Contact condition. All of the points on surface of i^{th} particle can be considered as contact point of n^{th} particle with i^{th} particle. The final coordinates of n^{th} particle can be obtained as given by,

$$\begin{aligned}
x(n) &= x(i) + (r(i) + r(n))\cos(\phi)\sin(\beta) \\
y(n) &= y(i) + (r(i) + r(n))\cos(\phi)\sin(\beta) \\
z(n) &= z(i) + (r(i) + r(n))\cos(\beta)
\end{aligned} \tag{3.8}$$

where, $\beta \in [0, \pi]$, and $\phi \in [0, 2\pi]$. Figure 3.4 depicts defined β and ϕ angles in Cartesian coordinate.

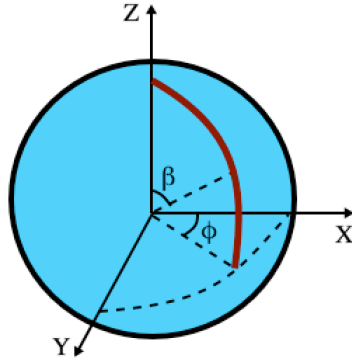


Figure 3.4: Defined β and ϕ angles in Cartesian coordinate

In order to simulate a dense medium, the n^{th} particle is located at minimum value of $z(n)$ while $z(n) > -(b/5)$.

3) Two-Contact

For any j^{th} particle, if F , given in Eq. (3.7), becomes negative, n^{th} particle can instate two contacts with i^{th} and j^{th} particles. In a similar procedure described before, the availability of third contact will be checked. Note that n^{th} particle will keep its contacts with i^{th} and j^{th} particles, while the algorithm looks for the third contact.

$$F_a = \sqrt{(x(i) - x(k))^2 + (y(i) - y(k))^2 + (z(i) - z(k))^2} - (r(i) + r(k) + 2r(n)) \tag{3.9}$$

$$F_b = \sqrt{(x(k) - x(j))^2 + (y(k) - y(j))^2 + (z(k) - z(j))^2} - (r(k) + r(j) + 2r(n)) \tag{3.10}$$

where, i and j are number of the particles that n^{th} particle established its first and second contacts, respectively, and $k = 1, \dots, n-1$ ($n \neq 1, k \neq i, k \neq j$). In Two-Contact situation, for any k , F_a or F_b will have positive value. In this case, the center of n^{th} particle will be located on intersection of two spheres with center coordinates same as those of i^{th} and j^{th} particles and greater radii of $r(i)+r(n)$ and $r(j)+r(n)$, respectively. The equations of these spheres are,

$$(x(n) - x(i))^2 + (y(n) - y(i))^2 + (z(n) - z(i))^2 = (r(i) + r(n))^2 \quad (3.11)$$

$$(x(n) - x(j))^2 + (y(n) - y(j))^2 + (z(n) - z(j))^2 = (r(j) + r(n))^2 \quad (3.12)$$

An intersection of two spheres is a circle. The center and radius of this circle can be derived from equation of a plane which circle lies on. The equation of the plane can be obtained from subtracting Eq. (3.11) from Eq. (3.12).

$$(x(j) - x(i))x(n) + (y(j) - y(i))y(n) + (z(j) - z(i))z(n) = L \quad (3.13)$$

where, L is,

$$L = \frac{(x^2(j) - x^2(i)) + (y^2(j) - y^2(i)) + (z^2(j) - z^2(i)) + (r(i) + r(n))^2 - (r(j) + r(n))^2}{2}$$

The center coordinate of circle (x_c, y_c, z_c) and its radius (r_c) are,

$$x_c = x(i) + (x(j) - x(i))t, \quad x_c \in X$$

$$y_c = y(i) + (y(j) - y(i))t, \quad y_c \in Y$$

$$z_c = z(i) + (z(j) - z(i))t, \quad z_c \in Z$$

$$r_c = \sqrt{(r(i) + r(n))^2 - ((x(i) - x(j))^2 + (y(i) - y(j))^2 + (z(i) - z(j))^2)t^2} \quad (3.14)$$

where, t is equal to,

$$t = \frac{L + x^2(i) + y^2(i) + z^2(i) - x(i)x(j) - y(i)y(j) - z(i)z(j)}{(x(i) - x(j))^2 + (y(i) - y(j))^2 + (z(i) - z(j))^2}$$

The n^{th} particle can be located at any point on the circumference of derived circle. While supposing the \vec{V} as a vector between center point of derived circle and a random point on the circle's plane, and \vec{U} as a vector along the line joining the centers of i^{th} and j^{th} particles, n^{th} particle coordinate will be equal to,

$$\begin{aligned} x(n) &= x_c - r_c \cdot \cos(\alpha) \hat{V}(1) + r_c \cdot \sin(\alpha) \vec{C}(1) \\ y(n) &= y_c - r_c \cdot \cos(\alpha) \hat{V}(2) + r_c \cdot \sin(\alpha) \vec{C}(2) \\ z(n) &= z_c - r_c \cdot \cos(\alpha) \hat{V}(3) + r_c \cdot \sin(\alpha) \vec{C}(3) \end{aligned} \quad (3.15)$$

where, $\alpha \in [0, 2\pi]$, \hat{V} is a unit vector of \vec{V} , and \vec{C} is a cross product of \hat{V} and \hat{U} . In order to form a dense medium, the n^{th} particle is located at minimum value of $z(n)$ while $z(n) > -(b/5)$.

4) Three-Contact

According to Eq. (3.9) and Eq. (3.10), for k^{th} particle, if both F_a and F_b have negative quantities, the third contact between n^{th} and k^{th} particle can be formed. Thus, n^{th} particle will have three contacts with i^{th} , j^{th} and k^{th} particles. In order to determine the center coordinates of n^{th} particle, an intersection of the circle (all possible locations for center of n^{th} particle, contacting i and j particles), which is described in previous part, with a sphere with coordinates of k^{th} particle and modified radius of $r(k) + r(n)$ is considered. Intersection of a circle and sphere will result in two points. In both of these points, n^{th} particle can establish three contacts. In order to find these points, the equation of the circle, Eq. (3.16), and sphere, Eq. (3.17), are considered.

$$(x(n) - x_c)^2 + (y(n) - y_c)^2 + (z(n) - z_c)^2 = (r_c)^2 \quad (3.16)$$

$$(x(n) - x(k))^2 + (y(n) - y(k))^2 + (z(n) - z(k))^2 = (r(k) + r(n))^2 \quad (3.17)$$

Subtracting these equations results in a plane equation, where coordinate of n^{th} particle is located on. The equation of the plane is,

$$(x_c - x(k))x(n) + (y_c - y(k))y(n) + (z_c - z(k))z(n) = W \quad (3.18)$$

where, W is,

$$W = \frac{(x^2(k) - x_c^2) + (y^2(k) - y_c^2) + (z^2(k) - z_c^2) + r_c^2 - (r(n) + r(k))^2}{2}$$

While considering Eq. (3.13), Eq. (3.16), Eq. (3.17) and Eq. (3.18), following quadratic equation will result:

$$a_1 \cdot z^2(n) + a_2 \cdot z(n) + a_3 = 0 \quad (3.19)$$

where, a_1 , a_2 and a_3 are parameters as given by,

$$a_1 = 1 + \left(\frac{(z(k) - z_c) - a_7}{x(k) - x_c} \right)^2 + \left(\frac{a_4}{a_5} \right)^2$$

$$a_2 = -2 \left(\frac{a_4 a_6}{a_5^2} \right) + 2y_c \left(\frac{a_4}{a_5} \right) - 2 \left(\frac{((z(k) - z_c) - a_7)(W + a_8)}{(x(k) - x_c)^2} \right) + 2x_c \left(\frac{(z(k) - z_c) - a_7}{x(k) - x_c} \right) - 2z_c$$

$$a_3 = z_c^2 + y_c^2 + x_c^2 + \left(\frac{a_6}{a_5} \right)^2 + \left(\frac{W + a_8}{x(k) - x_c} \right)^2 - 2x_c \left(\frac{W + a_8}{x(k) - x_c} \right) - 2y_c \left(\frac{a_6}{a_5} \right) - r_c^2$$

where, a_4 , a_5 , a_6 , a_7 , and a_8 are as written,

$$\begin{aligned}
 a_4 &= (z(k) - z_c) \cdot (x(j) - x(i)) - (z(j) - z(i)) \cdot (x(k) - x_c) \\
 a_5 &= (y(k) - y_c) \cdot (x(j) - x(i)) - (y(j) - y(i)) \cdot (x(k) - x_c) \\
 a_6 &= W \cdot (x(j) - x(i)) - L \cdot (x(k) - x_c) \\
 a_7 &= \frac{(y(k) - y_c) \cdot a_4}{a_5} \\
 a_8 &= \frac{(y_c - y(k)) \cdot a_6}{a_5}
 \end{aligned}$$

The greater root of Eq. (3.19) is considered to be the final Z coordinate of n^{th} particle. Afterwards, the final X and Y coordinates of n^{th} particle can be obtained from Eq. (3.16) and Eq. (3.17).

3.2.2.2 Stability Control

In order to form denser and realistic particle medium, stability control criterion is defined. Figure 3.5 shows differences between stable and unstable conditions for a particle illustrated with red sphere. If a particle is unstable, it will move deeper inside the medium (as if by gravity). The stability of n^{th} particle is controlled with coordinates of three contacted particles (i, j and k). A triangle plane formed from center of these particles is projected into XY plane. If projection of n^{th} particle to XY plane is inside the projected triangle, n^{th} particle is considered to be stable. Figure 3.6 shows the differences of stable and unstable conditions of n^{th} particle. i, j, k and n are projected points of corresponding particles.

3.2.2.3 Periodic Boundary Condition

In laboratory, the mechanical properties of soils are determined with conducting tests on soil samples. Procedures generally involve confinement of a sample inside the

containers or membranes. This confinement leads to minuscule errors due to development of additional interfaces (solid-water) and discontinuity of pores inside a soil sample. In a laboratory test, the specimen's dimensions are much larger than the particles, so the particles and pores that are affected by the boundaries are much smaller than the overall specimen. However, modeling such a domain with large number of particles would require a computing power that is currently not feasible.

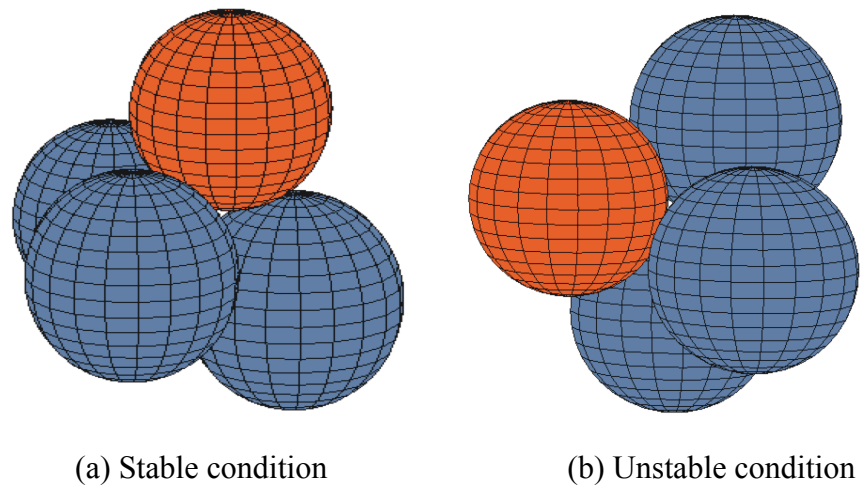


Figure 3.5: (a) Stable and, (b) unstable conditions of red particle

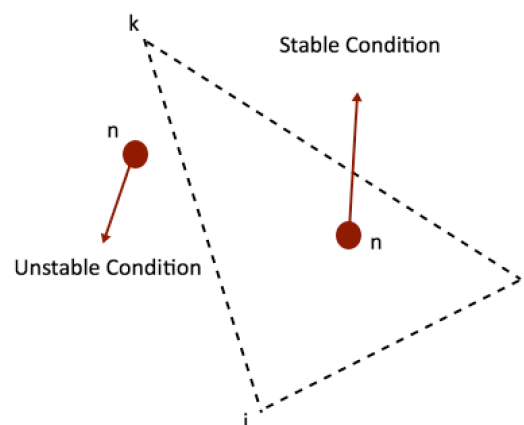


Figure 3.6: Projection of center points of relevant particles for stability control of n^{th} particle

In order to eliminate boundary effects and establish continuous pores, periodic boundary condition (PBC) is considered. The PBC is utilized when considered medium is infinite (soil) or extremely large. In order to form a PBC, the particles, which are located adjacent to the medium borders, are mirrored in X or Y directions. Figure 3.7 depicts the generated medium in XY plane. The packed particles are shown with gray color, while mirrored particles are in blue. Packed particles, whose centers are located inside the mirroring range (M_R), are mirrored. For example, i^{th} particle is mirrored in X, Y and XY directions. The total volume of segments of i^{th} and its mirrored particles that is inside the medium is equal to volume of i^{th} particle. M_R defines the mirroring range, which is set to establish the continuity of pores and also eliminate the intersection of the particles.

$$M_R = 2r_{max} \tag{3.20}$$

where, r_{max} is maximum radius of particles.

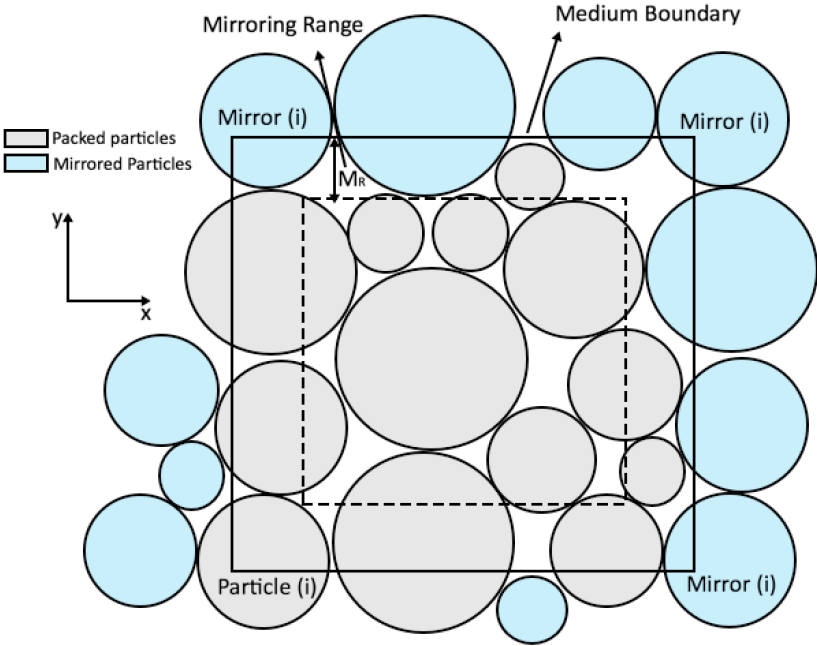


Figure 3.7: Particle mirroring in XY plane

As it can be observed from Figure 3.7, for any n^{th} particle, mirroring in X direction will be established,

$$\begin{aligned} \text{if } x(n) \leq M_R &\rightarrow x(n+1) = x(n) + b \\ \text{if } x(n) \geq b - M_R &\rightarrow x(n+1) = x(n) - b \end{aligned} \quad (3.22)$$

Similarly, these equations can be extended to Y and XY directions. Application of PBC provides some advantages such as, elimination of boundary effects, continuity of pores, and ability to duplicate the simulated medium in X and Y directions to form an infinite medium.

3.2.2.4 Void Ratio of Simulated Medium

After arrangement of the particles inside the medium, the void ratio of simulated medium will be determined. The total volume of the defined cubic medium (V_t) is equal to,

$$V_t = b^3 \quad (3.23)$$

where, b is dimension of the sides of defined cubic medium. For each particle, its volume (v_s) within the domain is,

$$v_s(i) = \begin{cases} \frac{4}{3} \pi r(i)^3 & , \text{if } z(i) > r(i) \ \& \ z(i) < b - r(i) \\ 0 & , \text{if } z(i) < -r(i) \ \text{or } z(i) > b + r(i) \ \text{or particle is mirrored} \\ V_{\text{cap}} & , \text{if } \left(z(i) < r(i) \ \& \ z(i) > -r(i) \right) \ \text{or} \ \left(z(i) < b + r(i) \ \& \ z(i) > b - r(i) \right) \end{cases} \quad (3.24)$$

where, $i=1, \dots, N$ (Note that N is total number of packed and mirrored particles), and V_{cap} is volume of spherical cap that is located inside the medium, which can be calculated according to Eq. (2.33).

Finally, the total volume of the particles inside the medium (V_s) will be equal to,

$$V_s = \sum_{i=1}^N v_{s(i)} \quad (3.25)$$

The void ratio of the medium is given by,

$$e = \frac{V_t - V_s}{V_s} = \frac{V_v}{V_s} \quad (3.26)$$

where, V_v is volume of voids. If the calculated void ratio is greater or smaller than acceptable range of desired void ratio (e_d), given by Eq. (3.27), the particles arrangement procedure will be repeated.

$$e_d - 0.02 \leq e \leq e_d + 0.02 \quad (3.27)$$

The generated medium with described method will result in dense packing. In order to pack a looser medium, the stability check (section 3.2.2.2) of n^{th} particle will be ignored if,

$$\frac{n}{D_f} \neq \text{integer} \quad (3.28)$$

where, D_f is density factor. This variable is input of the algorithm and in the case of dense packing it is equal to 1. By increasing the D_f value a looser medium will be formed, and vice versa. By iteration of the packing procedure, the desired void ratio of soil sample is obtainable. If the void ratio of medium is loosed or denser than

acceptable range (Eq. 3.27), in the next iteration of packing algorithm D_f is altered as given by.

$$\begin{aligned} \text{If } e < e_d - 0.02 &\rightarrow D_f = D_f + 3 \\ \text{If } e > e_d + 0.02 \text{ and } D_f \neq 1 &\rightarrow D_f = D_f - 1 \end{aligned} \quad (3.29)$$

After 10 times of packing iteration, if the void ratio of simulated medium cannot satisfy the acceptable range of target void ratio the process will stop and the medium with closest void ratio to target void ratio will be considered.

3.2.3 Results of Packing Algorithm

Two examples of specimens that are packed with the described method are presented in Figure 3.8. In first example the uniform specimen is simulated (Figure 3.8a). All the particles are in diameter range of 125-150 μm and the void ratio of simulated medium is 0.66. Similarly, the non-uniform specimen with diameter range of 100-300 μm is simulated (Figure 3.8b). The PSD of this specimen is given in Figure 3.9. The void ratio of simulated medium is 0.68.

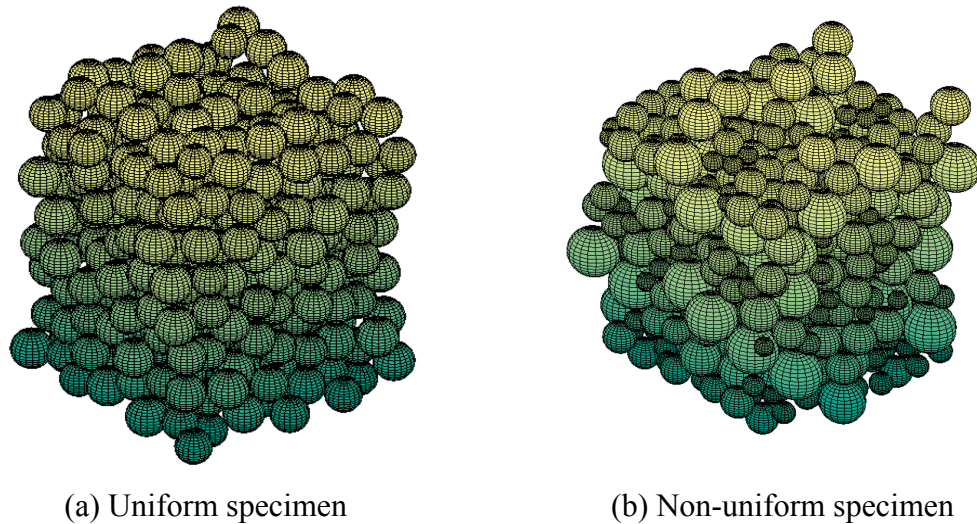


Figure 3.8: The simulated (a) uniform and, (b) non-uniform specimens

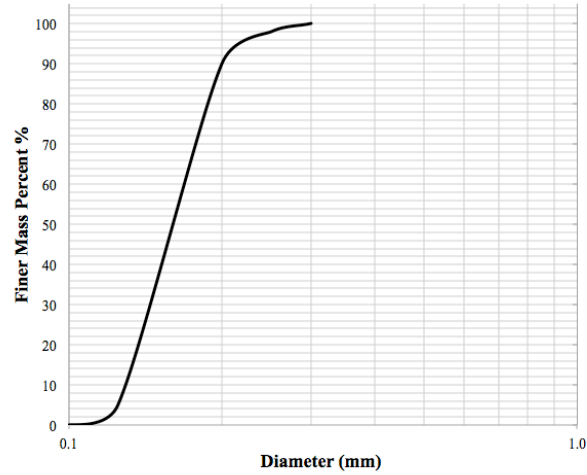


Figure 3.9: PSD of non-uniform specimen

3.2.3.1 Variability of Void Ratio

The generated particles are packed randomly inside the defined medium. Therefore, the void ratio of simulated medium after each packing iteration will be different. In this regard, the standard deviation and variance of void ratio of specimens given in Figure 3.8 is determined. To this end, particles are generated according to the PSD of specimens. Subsequently, for each specimen spherical particles are packed in 5 different iterations. Table 3.1 shows the resulted void ratios of specimens in each iteration.

Table 3.1: Void ratios of simulated media

Iteration	(a) Void ratio of uniform specimen (125-150 μ m)	(b) Void ratio of non-uniform specimen (100-300 μ m)
1	0.634	0.684
2	0.647	0.634
3	0.658	0.647
4	0.661	0.691
5	0.669	0.639

The variance (v) and standard deviation (σ) of void ratio of both specimens are calculated with following equations and presented in Table 3.2.

$$v = \frac{1}{5} \sum_{i=1}^5 (e_i - \bar{e})^2 \quad (3.30)$$

$$\sigma = \sqrt{v} \quad (3.31)$$

where, \bar{e} is mean void ratio.

Table 3.2: Standard deviation (σ) and variance (v) of void ratio

Specimen	v	σ
(a) Uniform specimen	0.000147	0.0121
(b) Non-uniform specimen	0.00038	0.0194

According to Table 3.2, with decreasing the uniformity of the specimen, the standard deviation is increased.

3.2.3.2 Homogeneity of Simulated Medium

In order to visualize the distribution of particles inside the simulated medium, the simulated non-uniform specimen (Figure 3.8b) is divided in to half. The void ratios and the PSDs of upper and lower rectangular prisms are determined and presented in Table 3.3 and Table 3.4, respectively. Resulted void ratios demonstrate the uniformity of particles distribution inside the medium. According to Table 3.4, the distribution of particles inside the medium is almost uniform.

Table 3.3: Void ratios of simulated non-uniform medium and divided halves

Void ratio of cubic medium	Void ratio of top prism	Void ratio of bottom prism
0.684	0.687	0.681

Table 3.4: PSDs of simulated cubic medium and divided halves

Diameter (mm)	Finer Mass percent %			
	Input	Cubic medium	Top prism	Bottom prism
0.3	100	100	100	100
0.25	98	97.74	97.34	98.14
0.2	90	89.98	87.92	92.04
0.15	30	28.57	28.43	28.71
0.125	5	4.98	5.28	4.68
0.1	0	0	0	0

3.3 Identification of Porous Medium

According to section 2.3.2, in pore-scale modeling of the medium, each of the pores will have different size and irregular shape. Thus, each pore should be evaluated individually. The pore water consists of three phases: Bulk water, pendular rings and adsorbed water. While considering the volume of these phases, volume of adsorbed water is negligible. Therefore, in this research, the pore water is assumed to only consist of bulk waters and pendular rings. Throughout this research, portion of the pore containing the bulk water is named as bulk pore. Figure 3.10 shows the flow chart of porous identification procedure.

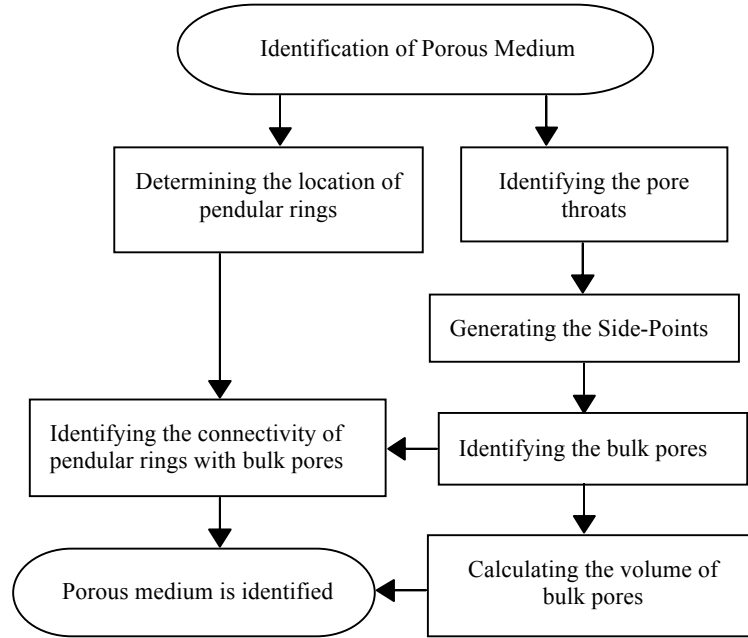


Figure 3.10: Flow chart of porous medium identification

3.3.1 Defining the Pore Throats

Pore throats are narrow passages between the particles. In general, pore throats are interfaces between two bulk pores. Therefore, identifying the pore throats will result in not only the spatial limits of bulk pores, but also characterizations of interconnectivity of pores. In this algorithm, a pore throat is developed among three adjacent particles. Maximum size of the passage to be considered as pore throat is deemed important. Consequently, the criterion to check the possibility of pore throat development is defined in regard to distances between surfaces of particles. The pore throat will be defined between three particles (i, j and k), if following relations can be satisfied.

$$\sqrt{(x(i) - x(j))^2 + (y(i) - y(j))^2 + (z(i) - z(j))^2} - r(i) - r(j) \leq 2 \times \min(r(i), r(j))$$

$$\sqrt{(x(i) - x(k))^2 + (y(i) - y(k))^2 + (z(i) - z(k))^2} - r(i) - r(k) \leq 2 \times \min(r(i), r(k))$$

$$\sqrt{(x(k)-x(j))^2+(y(k)-y(j))^2+(z(k)-z(j))^2}-r(k)-r(j)} \leq 2 \times \min(r(k),r(j)) \quad (3.32)$$

where, $i = 1, \dots, N$, $j = 1, \dots, N$ and $k = 1, \dots, N$ ($j \neq i$, $k \neq i$ and $k \neq j$). For any i, j and k that can satisfy above-mentioned relations, the pore throat can be identified only if other particles don't intersect the considered pore throat region. To this end, the plane is passed from center points of considered particles. This plane is known as throat plane. Figure 3.11 depicts the throat plane formed between three particles. If throat plane intersects with any particles other than i, j and k , the throat plane will not be formed. This situation can occur in non-uniform soils. Figure 3.12 represents the described problem in XY plane. The pore throat cannot be formed between particles i, j and k , because of its intersection with particle noted by p . Instead, three smaller pore throats as shown are developed. Eventually, in the end of throat identification process, all possible pore throats and their equivalent throat planes will be identified and labeled.

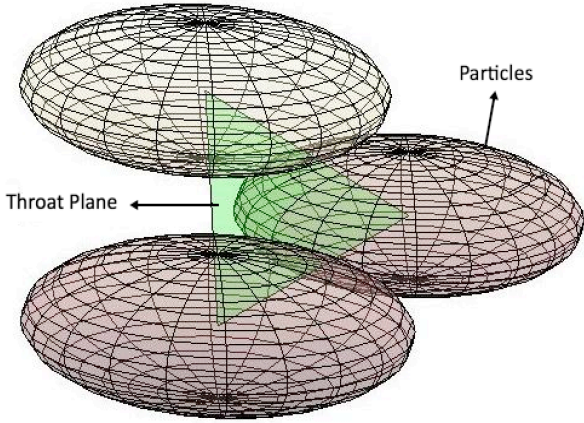


Figure 3.11: Defined throat plane

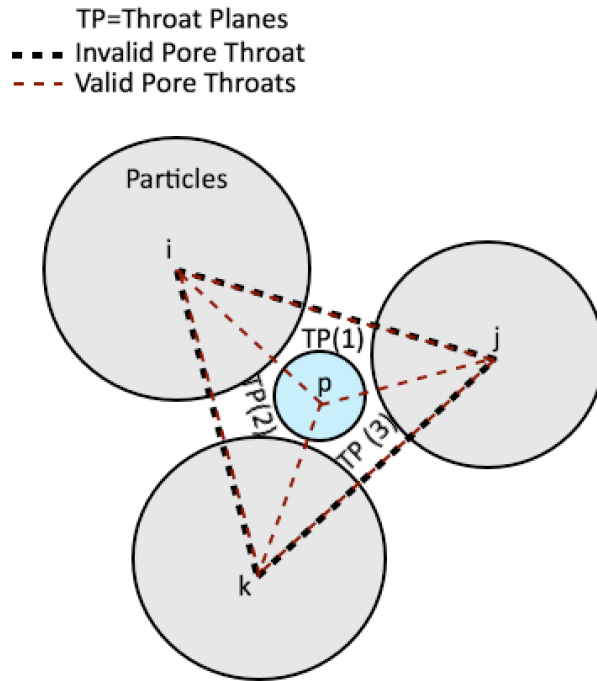


Figure 3.12: Invalid and valid throat planes in XY plane

As mentioned in section 3.2.2.3, application of the PBC will provide continuous pores. By mirroring the particles, pores among them are also mirrored. While considering the particles forming the pore throats, mirrored pore throats are determined. These pore throats are located outside of considered cubic medium and will provide continuity of pores in X and Y directions.

3.3.2 Throat Side-Points

Throat planes will be used to identify bulk pores and their connectivity. As mentioned before, a throat plane is an interface between two bulk pores. Therefore, properties of pores will be different in opposite sides of a throat plane. For an instance, for a single throat plane, which is connecting two pores, the pore located on the right side of the plane can be full of water while the pore on the left side is drained. In this regard, two points on opposite sides of throat planes are generated. These points are called Side-Points and are generated near the center of inverse masses of the particles forming the

throat planes. The radius of the particles is considered as mass parameter. Thus, the center mass coordinate (x_m , y_m and z_m) of pore throat particles i , j and k is equal to,

$$\begin{aligned}
 x_m &= \frac{\frac{x(i)}{r(i)} + \frac{x(j)}{r(j)} + \frac{x(k)}{r(k)}}{\frac{1}{r(i)} + \frac{1}{r(j)} + \frac{1}{r(k)}} , & x_m \in X \\
 y_m &= \frac{\frac{y(i)}{r(i)} + \frac{y(j)}{r(j)} + \frac{y(k)}{r(k)}}{\frac{1}{r(i)} + \frac{1}{r(j)} + \frac{1}{r(k)}} , & y_m \in Y \\
 z_m &= \frac{\frac{z(i)}{r(i)} + \frac{z(j)}{r(j)} + \frac{z(k)}{r(k)}}{\frac{1}{r(i)} + \frac{1}{r(j)} + \frac{1}{r(k)}} , & z_m \in Z
 \end{aligned} \tag{3.33}$$

This point is located on throat planes. By adding the epsilon value (ϵ) to z_m , a positive or negative distance of considered point from its throat plane will be gained.

$$z_m = z_m + \epsilon \tag{3.34}$$

The generated point is first Side-Point of throat plane. Thence, this point will be mirrored in respect to relative throat plane and this will result in second Side-Point in opposite side of throat plane. The distance sign of mirrored point will be opposite of original point. For all throat planes defined in previous section, these Side-Points will be defined. Figure 3.13 shows the generated Side-Points for a single throat plane. If a distance sign of blue Side-Point from its throat plane is positive, the red one will have negative distance sign.

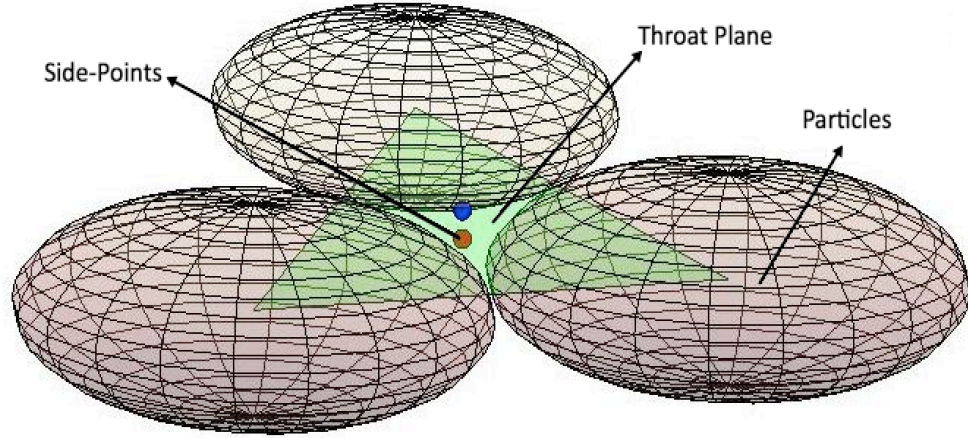


Figure 3.13: Generated Side-Points

For a throat plane formed between particles i , j and k , the distance of a Side-Point from this throat plane, F_d , will be,

$$F_d = \frac{x_m \cdot \bar{C}(1) + y_m \cdot \bar{C}(2) + z_m \cdot \bar{C}(3) + T}{\sqrt{\bar{C}(1)^2 + \bar{C}(2)^2 + \bar{C}(3)^2}} \quad (3.35)$$

where, \bar{C} is cross product of vectors $\bar{V}(i,j)$ and $\bar{V}(i,k)$,

$$\bar{C} = \bar{V}(i,j) \times \bar{V}(i,k) = \begin{bmatrix} (1) & (2) & (3) \\ x(i) - x(j) & y(i) - y(j) & z(i) - z(j) \\ x(i) - x(k) & y(i) - y(k) & z(i) - z(k) \end{bmatrix}$$

, and T is,

$$T = -x(i) \cdot \bar{C}(1) - y(i) \cdot \bar{C}(2) - z(i) \cdot \bar{C}(3)$$

It is essential to identify the mirrored Side-Points. For any mirrored pore throat, their relevant Side-Points will be marked as mirrored Side-Points.

3.3.3 Identifying Bulk Pores

The algorithm identifies, bulk pores with throat planes and their associated Side-Points. In respect to number of the throat planes enclosing the bulk pores, the bulk pores are separated into two types: Bulk pores entrapped between four throat planes (common case in Three-Contact particle arrangement given in section 3.2.2.1), and bulk pores enclosed between more than four throat planes.

When the bulk pore is entrapped between four throat planes, only eight Side-Points will be considered in total. The challenge is to identify the Side-Points located inside the bulk pores. As mentioned in section 3.3.2, each throat plane has two Side-Points defined on its in opposite sides. The distance signs of Side-Points, Eq. 3.35, are not only calculated for their respective throat plane, but all adjacent throat planes that possibly bound a pore. The distances of all nearby Side-Points from each throat plane are calculated. For a single throat plane only one of the Side-Points around a single pore will have distance sign opposite of the rest. This Side-Point is located outside of the considered bulk pore. By repeating the same procedure for other throat planes, all of the four Side-Points located outside of the considered bulk pore are distinguished. Remaining Side-Points are located inside the same bulk pore and are marked with number of the bulk pore. According to Figure 3.14, for a throat plane TP_1 , all of the Side-Points will have similar distance sign apart from SP_2 . Similarly, for throat planes of TP_2 , TP_3 and TP_4 , respectively SP_4 , SP_5 and SP_9 will have distance signs different from the rest. These Side-Points are shown with red points. Figure 3.15 illustrates the bulk pore identified with this procedure in 3D. This method of bulk pore identification is precise and will increase the accuracy of next approach.

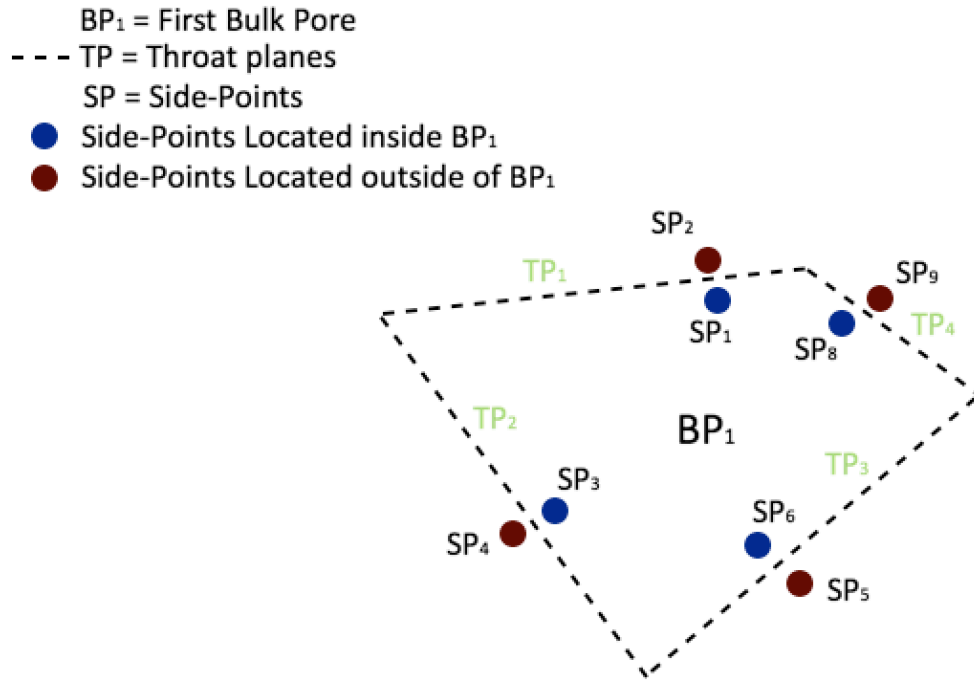


Figure 3.14: Schematic of the bulk pore identification process, 1th method

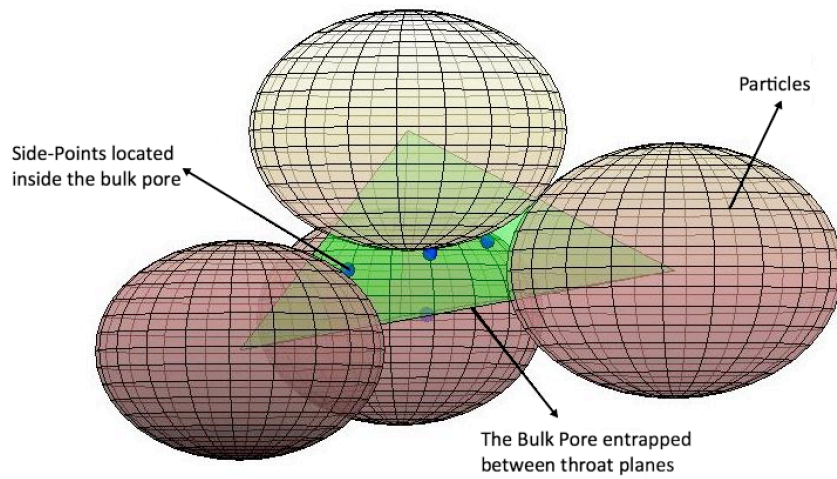


Figure 3.15: The bulk pore entrapped between four particles and relevant Side-Points in 3D

The rest of the bulk pores will be determined with different approach. In second method of bulk pore identification, for a single Side-Point, which is not marked in pre-mentioned method, four closest Side-Points will be determined in a way that, all of these Side-Points will have similar distance signs from throat plane of considered Side-Point. The reason for choosing four Side-Points is to consider at least three throat planes in identification process. According to Figure 3.16, for SP₁, four closest Side-Points with similar distance sign from TP₁ will be SP₃, SP₄, SP₉ and SP₁₀. The relevant throat planes of Side-Points will be TP₁, TP₂ and TP₅. Next, for each of relevant throat planes, the distance signs of Side-Points will be compared to distance sign of Side-Point SP₁. For TP₂, the distance sign of SP₄ will be opposite of SP₁. As a result, the Side-Point of SP₄ is located in different bulk pore than SP₁. The distance sign of SP₁, SP₃ and SP₉ will be similar for all of the three throat planes TP₁, TP₂ and TP₅. Thus, these Side-Points are located in a same bulk pore noted by BP₁. By continuing the process the rest of Side-Points, which are located inside BP₁, will be determined. These points are represented with blue points in Figure 3.16. In order to avoid errors engendered in this method, following control sequences for the Side-Point in consideration and each of its closest Side-Points are applied.

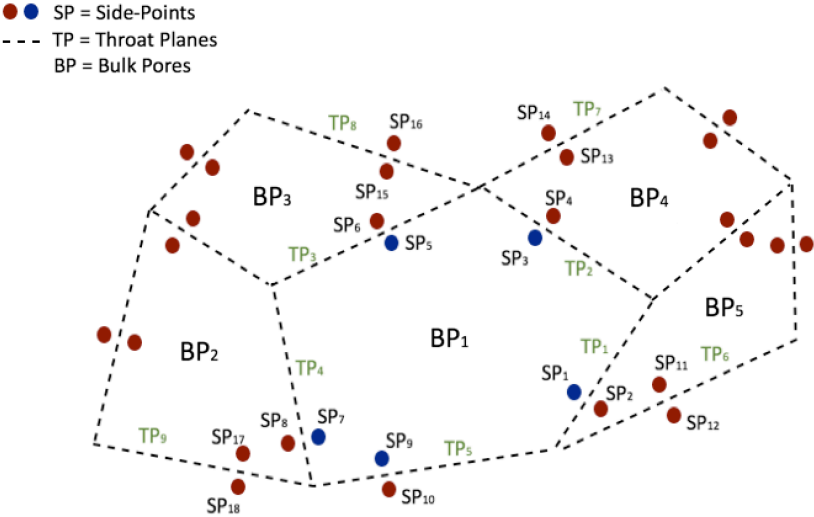


Figure 3.16: Schematic of bulk pore identification process, 2nd method

- 1) Both of the Side-Points are unidentified: In this case, these Side-Points do not belong to any bulk pore. Thus, they will be marked as a new bulk pore.
- 2) Only one of the Side-Points is identified: In this situation, the unidentified Side-Point will be marked as it is located inside a same bulk pore as identified one.
- 3) Both of the Side-Points are identified and located inside a same bulk pore: if both of the Side-Points located inside a same bulk pore, no alteration will be made.
- 4) Side-Points are previously identified and located in different bulk pores: In this condition, previously identified bulk pores will merge to form a single bulk pore and as a result, these Side-Points will be located in a similar bulk pore.

This method is visually checked and observed to be accurate. Figure 3.17 and Figure 3.18 are examples of bulk pores defined with this method.

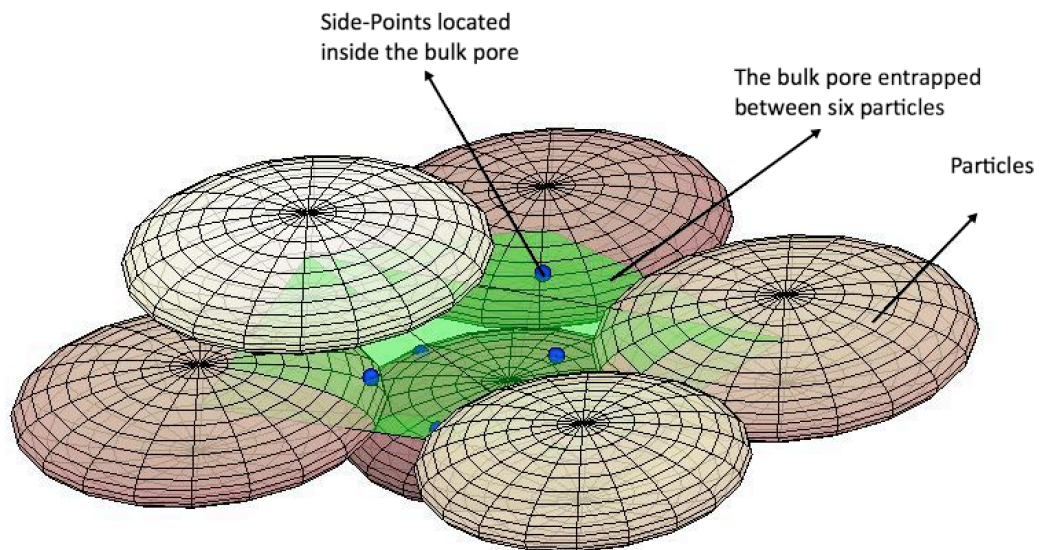


Figure 3.17: The bulk pore entrapped between six particles

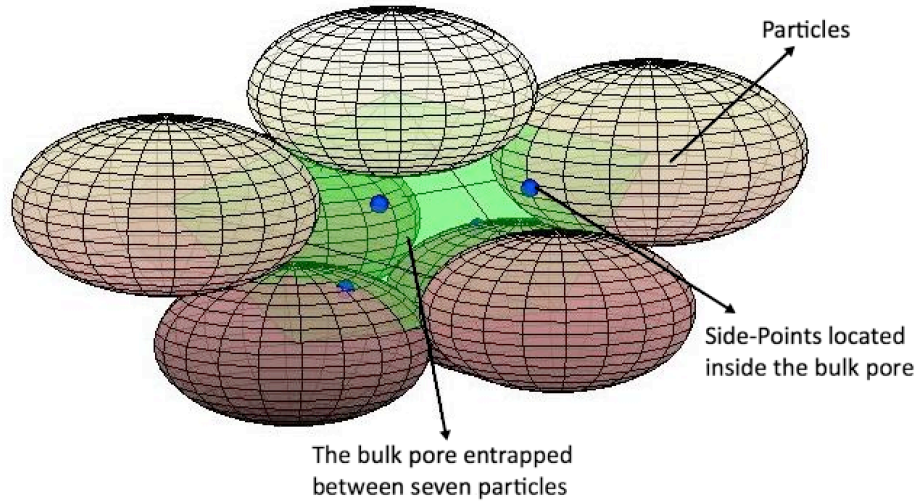


Figure 3.18: The bulk pore entrapped between seven particles

When all of the Side-Points located inside the single bulk pore are mirrored Side-Points, the bulk pore is also considered as mirrored. This means the bulk pore is located completely outside of the considered cubic medium. However, if portion of the Side-Points are mirrored and some not, the bulk pore is located at boundaries of medium. These bulk pores will provide the continuity between the pores located inside and outside of the medium.

3.3.4 Volume of Bulk Pores

The shapes of bulk pores are irregular, which makes the calculation of the volume more complex. For obtaining SWCC, the water content of the medium after each suction increment is needed. The water content of the medium is the ratio of remaining water after each suction increment to total volume of water in saturation condition. Therefore, obtaining the ratio between volumes of the bulk pores will also be sufficient. In order to determine the proportion volume of the bulk pores, the identified Side-Points of each bulk pore are assumed to be vertices of tetrahedrons and subsequently, volumes of tetrahedrons are ascribed to volume of each bulk pore. In an instance, for a bulk pore consist of four Side-Points only one tetrahedron can be

formed. Similarly, for a bulk pore composed of five Side-Points two tetrahedrons can be defined. The resulting volumes are smaller than actual size of the bulk pores. However, proportion of volume of bulk pores with respect to other pores is preserved. The volumes of the tetrahedrons are determined by means of Delaunay triangulation and convex hull functions ('DelaunayTri' and 'convexHull'), which are available in MATLAB program. Basically, these functions generate the feasible discrete tetrahedrons from identified Side-Points of each bulk pore and subsequently calculate the volume of each tetrahedron. The proportion volume of each bulk pore (v_B) is equal to,

$$v_B = \sum_{i=1}^n \text{Volume}(\text{Tetrahedron})_i \quad (3.36)$$

where, n is total number of tetrahedrons that constitute the bulk pore. In drainage process (section 3.5), these volumes will be normalized with regard to total volume of voids of simulated medium. This will lead to negligible error in final results.

3.3.5 Pendular Rings

3.3.5.1 Possibility of Pendular Rings Formation

The pendular rings will be formed between two adjacent particles due to capillary action. The challenge is to determine the maximum distance between the particles that results in pendular ring formation. Dependency of this distance to induced suction, results in more complex problem. To be on the safe side, for any two particles satisfying Eq. (3.37), the pendular rings will be formed.

$$\sqrt{(x(i) - x(j))^2 + (y(i) - y(j))^2 + (z(i) - z(j))^2} - r(i) - r(j) \leq \min(r(i), r(j)) \quad (3.37)$$

where, $i = 1, \dots, N$, $j = 1, \dots, N$ ($j \neq i$), and N is total number of particles inside the simulated medium.

The pendular rings will emerge after drainage of bulk waters. Therefore, the connectivity of pendular rings to bulk pores should be determined. Figure 3.19 depicts the pendular ring formed between particles of i and j in XY plane. When bulk pore BP_1 contains water and BP_2 is drained, the semi-pendular ring is formed only on the side connected to BP_2 . In this regard, the total number of the bulk pores surrounding both particles of pendular rings is determined. This identification is useful in calculation of pendular rings volumes in drainage process. It determines when pendular rings will be formed and which shape they will have (full pendular ring or semi-pendular ring).

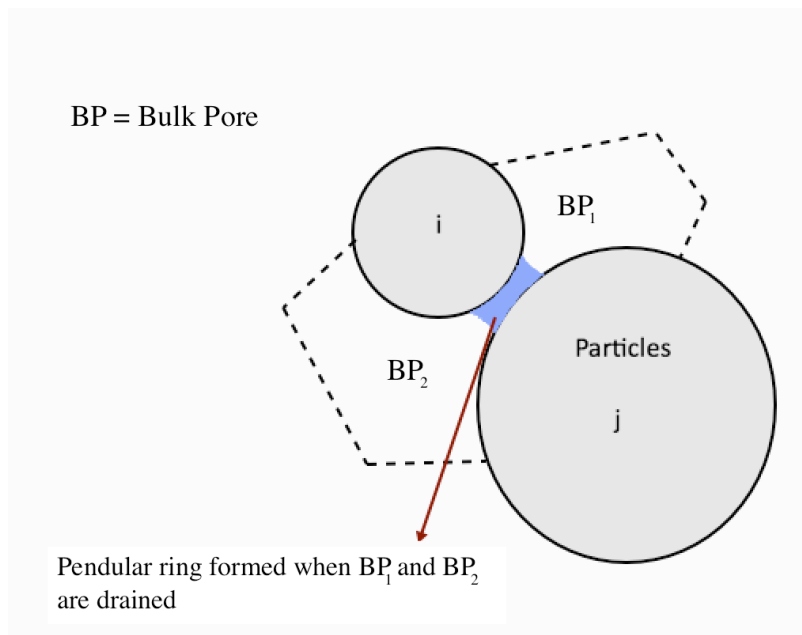


Figure 3.19: Schematic of connectivity of pendular rings

3.3.5.2 Volume of Pendular Rings

As mentioned in section 2.3.3.1, the volume of pendular rings can be calculated with assumption of circular surface. While assuming the filling angle of ϕ_1 , the volume of pendular rings can be calculated. However, the filling angle varies with amount of applied suction. In order to form a relation between filling angle and suction value, the Young-Laplace equation for air-water interfaces is considered.

$$\text{suction} = \psi = \sigma_{st} \left(\frac{1}{R_1} - \frac{1}{R_2} \right) \quad (3.38)$$

where, R_1 and R_2 are principal radii of pendular ring.

For two particles between which a pendular ring can be formed (Eq. (3.37)), the principal radii are calculated with Eq. (2.25) and Eq. (2.27), which are given in section 2.3.3.1. Finally, volume of a pendular ring (v_p) will be equal to,

$$v_p = V_1 - V_2 \quad (3.39)$$

where, V_1 and V_2 are presented in Eq. (2.32) and Eq. (2.35), respectively.

With regard to possibility of pendular ring formation, the distance criterion defined in Eq. (3.37) is considered large enough to cover all the possibilities. But, dependency of this distance to suction should be characterized. Thus, the second criterion is defined corresponding to amount of applied suction. A pendular ring can be formed, if $R_2 > R_1$. Otherwise, the suction is large enough to drain the considered pendular ring. Eventually, for different filling angles, the suction value, Eq. (3.38), and associated volume of pendular rings, Eq. (3.39), can be measured. Therefore, volume of pendular rings at any suction value can be determined.

3.4 Air Entry Pressure of Pore Throats

In this algorithm the AEP of the medium is represented with combination of individual AEPs of pore throats. Hence, superior approximation of AEP of the medium is obtained. This also led to more accurate SWCC results. Figure 3.20 illustrates the flow chart of AEP determination process.

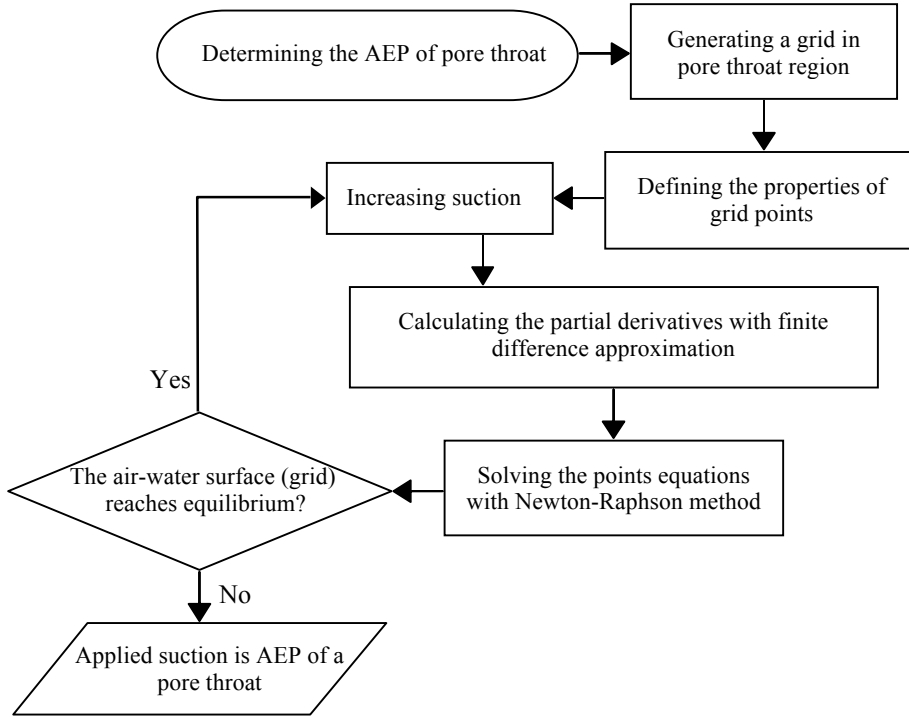


Figure 3.20: Flow chart of AEP determination process

3.4.1 Grid Placement in Pore Throat Region

To begin with AEP acquisition process, initially, grids will be defined and located in pore throat regions (Figure 3.21). These grids represent the air-water interfaces in considered regions. The air medium is considered to be above the grid and water under it. Initially, the coordinates of particles i , j and k , which form the pore throat, will be transformed to local coordinates in a way that their centers have the same elevation ($z(i)=z(j)=z(k)$). This will speed up the convergence procedure of Newton-Raphson method, which will be discussed in section 3.4.4. Afterwards, for a single grid, step sizes in X and Y directions (ΔX and ΔY) are obtained as given by,

$$\Delta X = \frac{\max \left[x(i) \quad x(j) \quad x(k) \right] - \min \left[x(i) \quad x(j) \quad x(k) \right]}{A}$$

$$\Delta Y = \frac{\max \left[y(i) \quad y(j) \quad y(k) \right] - \min \left[y(i) \quad y(j) \quad y(k) \right]}{A} \quad (3.40)$$

where, A is the number of grid intervals.

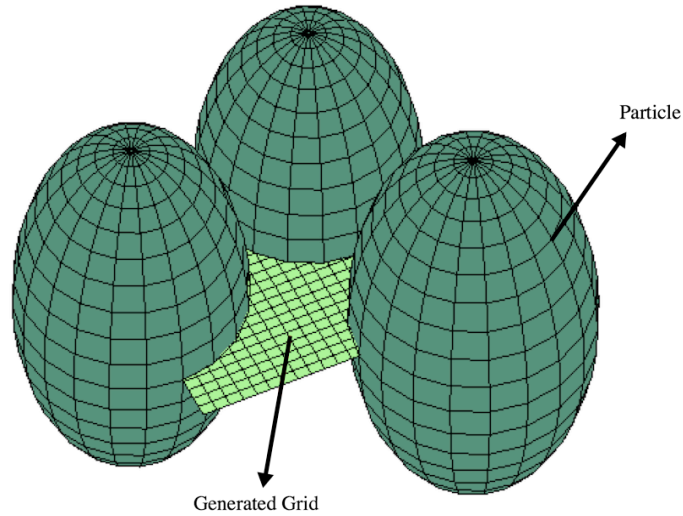


Figure 3.21: Grid defined in pore throat region

With larger A values, more grid points will be generated. Therefore, it will lead to more accurate results. However, larger A values slows down the calculation procedure of AEP, which will be performed thousands of times in one run of the algorithm. In the algorithm, iteration of the A value continues until grid can cover pore throat region with minimum number of points (B). Studying the effect of grid intervals (section 3.4.5.1) led to the optimum number of B to be 50.

The primary coordinates of grid points (x_p , y_p and z_p) are given by,

$$\begin{aligned}
 x_p(m+1,t+1) &= \min \left[x(i) \quad x(j) \quad x(k) \right] + \Delta X \cdot m \quad , \quad x_p \in X \\
 y_p(m+1,t+1) &= \min \left[y(i) \quad y(j) \quad y(k) \right] + \Delta Y \cdot t \quad , \quad y_p \in Y \\
 z_p(m+1,t+1) &= z(i) = z(j) = z(k) \quad , \quad z_p \in Z
 \end{aligned}
 \tag{3.41}$$

where, $m=0, \dots, A$ and for each m value $t=0, \dots, A$.

3.4.2 Characteristics of Grid Points

For grid points located inside the considered throat plane, two distinct conditions will be encountered. The grid points located on surface of particles will be used to satisfy the contact angle of air-water surface with particles. Meanwhile, the grid points located inside the pore throat region will fulfill the curvature of air-water surface for an applied suction.

Initially, grid points located outside of the pore throat region are determined. These points are not considered in AEP measurement process. These grid points are located outside of the triangle formed by centers of three particles. Figure 3.22 shows the grid points located inside the throat plane in XY plane.

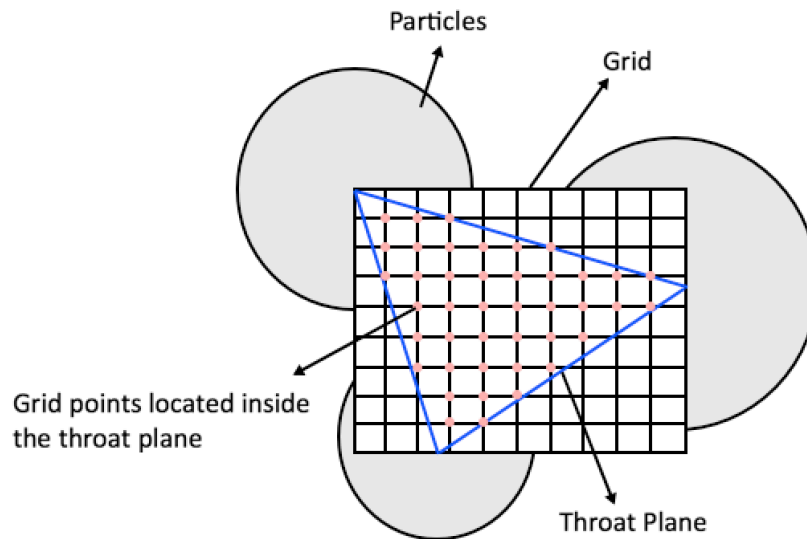


Figure 3.22: Grid points located inside throat plane

The grid points, which are located inside the throat plane, will encounter three distinct situations: located inside the particle, near a particle surface, which are approximated to be on the particle surface, or inside pore throat region. Figure 3.23 shows these points in pink, blue and red, respectively.

- Grid points inside pore throat region (Curvature Points)
- Grid points inside the particles (may become boundary points in next iterations)
- Grid points approximated to be on surface of particles (Boundary Points)

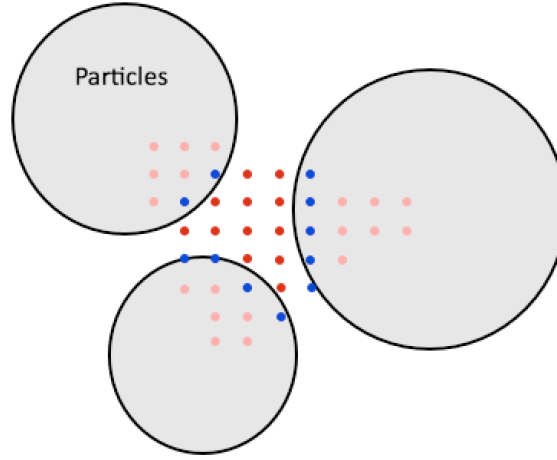


Figure 3.23: Properties of grid points

The X and Y coordinates of grid points are assumed to be stationary. Therefore, they can only move in Z direction. Variation of grid interval (ΔX or ΔY) would require more complex finite difference approximation method. In order to avoid this complexity, the grid points that are located closest to surface of the particles from the inside are approximated to be on surface of particles. These points are designated as boundary points. The distance of grid points to surface of i^{th} particle is controlled as given by,

$$F_c = \sqrt{(x_p(m+1, t+1) - x(i))^2 + (y_p(m+1, t+1) - y(i))^2 + (z_p(m+1, t+1) - z(i))^2} - r(i) \quad (3.42)$$

where, $m=0, \dots, A$, and for each m value $t=0, \dots, A$. For any grid point, which is located inside triangle throat plane, if $F_c < 0$, the point is located inside the i^{th} particle. In contrast, if $F_c > 0$, the point is located in pore throat region. For i^{th} particle, the closest points to surface of the particle from inside will be marked as boundary points.

The points located inside the pore throat region are designated as curvature points. Therefore, the air-water surface is composed of boundary and curvature points.

3.4.2.1 Boundary Points

The points located on surfaces of the particles or close to it are considered as boundary points. These points are set to satisfy the contact angle of air-water surface with particle surfaces. Figure 3.24 depicts the contact angle (θ) between air-water and particle surfaces in XZ plane. The \vec{N}_p and \vec{N}_{a-w} are normal vectors to surface of the i^{th} particle and air-water interface in the contact point of Q, respectively.

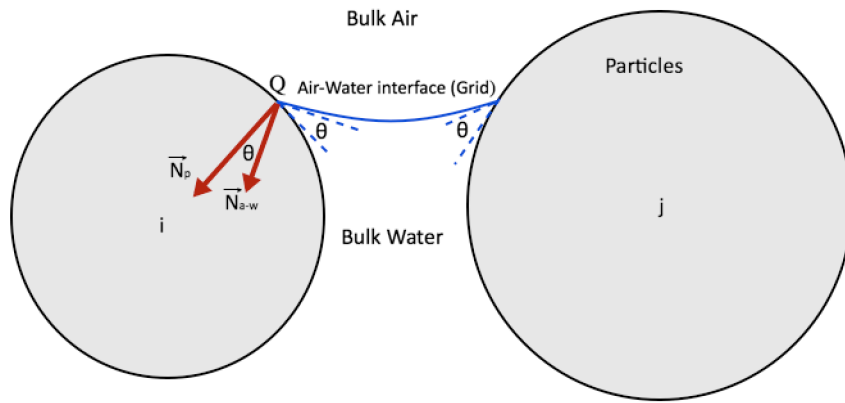


Figure 3.24: Contact angle in particle-air-water interface

In equilibrium condition, the contact angle between the normal vectors will be equal to θ . The dot product of normal vectors will be as given by,

$$\vec{N}_p \cdot \vec{N}_{a-w} = \left| \vec{N}_p \right| \left| \vec{N}_{a-w} \right| \cos(\theta) \quad (3.43)$$

The equation of i^{th} particle is,

$$(X - x(i))^2 + (Y - y(i))^2 + (Z - z(i))^2 = r(i)^2 \quad (3.44)$$

As a result, the normal vector to surface of i^{th} particle will be,

$$\vec{N}_p = \begin{bmatrix} -\frac{\partial f_p}{\partial X} \\ -\frac{\partial f_p}{\partial Y} \\ -\frac{\partial f_p}{\partial Z} \end{bmatrix} = \begin{bmatrix} -2(X - x(i)) \\ -2(Y - y(i)) \\ -2(Z - z(i)) \end{bmatrix} \quad (3.45)$$

where, f_p is,

$$f_p = (X - x(i))^2 + (Y - y(i))^2 + (Z - z(i))^2 - r(i)^2$$

While representing the air-water surface with explicit equation,

$$Z = Z(X, Y) \quad (3.46)$$

The \vec{N}_{a-w} can be written as,

$$\vec{N}_{a-w} = \begin{bmatrix} \frac{\partial f_{a-w}}{\partial X} \\ \frac{\partial f_{a-w}}{\partial Y} \\ \frac{\partial f_{a-w}}{\partial Z} \end{bmatrix} = \begin{bmatrix} Z_X \\ Z_Y \\ -1 \end{bmatrix} \quad (3.47)$$

where, Z_X and Z_Y are partial derivatives of Z in X and Y directions, respectively, and f_{a-w} is equal to,

$$f_{a-w} = Z(X, Y) - Z \quad (3.48)$$

Substituting Eq. (3.45) and Eq. (3.47) into Eq. (3.43) results in,

$$\begin{bmatrix} -2(X-x(i)) \\ -2(Y-y(i)) \\ -2(Z-z(i)) \end{bmatrix} \cdot \begin{bmatrix} Z_x \\ Z_y \\ -1 \end{bmatrix} = 2\sqrt{(X-x(i))^2 + (Y-y(i))^2 + (Z-z(i))^2} \sqrt{Z_x^2 + Z_y^2 + 1} \cdot \cos(\theta) \quad (3.49)$$

Eventually, the equation of boundary points will be equal to,

$$f(Z) = (x(i) - X)Z_x + (y(i) - Y)Z_y + (Z - z(i)) - \sqrt{(X-x(i))^2 + (Y-y(i))^2 + (Z-z(i))^2} \sqrt{Z_x^2 + Z_y^2 + 1} \cdot \cos(\theta) \quad (3.50)$$

where, X, Y, and Z are coordinates of boundary points, and i is index of the particles forming the pore throat. Note that in equilibrium condition, for a given contact angle the value of f(Z) in Eq. (3.50) will be zero.

3.4.2.2 Curvature Points

The points located inside pore throat region are designated as curvature points. These points represent the curvature of air-water surface. While considering the variational derivatives of Young-Laplace equation (Section 2.1.1), the curvature equation of grid points will be equal to,

$$f(Z) = \frac{(Z_{xx}(1+Z_y^2)) - 2Z_x Z_y Z_{xy} + (Z_{yy}(1+Z_x^2))}{(\sqrt{1+Z_x^2+Z_y^2})^3} - \frac{\psi}{\sigma_{st}} \quad (3.51)$$

In equilibrium condition, for a given suction value (ψ), the value of Eq. (3.51) will be zero. Eq. (3.50) and Eq. (3.51) are partial differential equations and their exact solutions are not available. In order to solve these equations, finite difference approximation is utilized.

3.4.3 Finite Difference Approximation

In order to calculate the partial derivatives given in Eq. (3.50) and Eq. (3.51), finite difference approximation method is considered. Figure 3.25 is an example of defined grid in XY plane. According to this figure and equations given in section 2.6.3, the central approximations of Z_X , Z_Y , Z_{XX} , Z_{YY} and Z_{XY} are given by,

$$\begin{aligned}
 Z_X(m,t) &= \frac{Z(m+1,t) - Z(m-1,t)}{2\Delta X} \\
 Z_Y(m,t) &= \frac{Z(m,t+1) - Z(m,t-1)}{2\Delta Y} \\
 Z_{XX}(m,t) &= \frac{Z(m+1,t) - 2Z(m,t) + Z(m-1,t)}{\Delta X^2} \\
 Z_{YY}(m,t) &= \frac{Z(m,t+1) - 2Z(m,t) + Z(m,t-1)}{\Delta Y^2} \\
 Z_{XY}(m,t) &= \frac{Z(m+1,t+1) - Z(m-1,t+1) - Z(m+1,t-1) + Z(m-1,t-1)}{4\Delta X\Delta Y}
 \end{aligned}
 \tag{3.52}$$

where, $m=2,\dots,A$, $t=2,\dots,A$, and grid point indices (ΔX and ΔY) are given in Eq. (3.40).

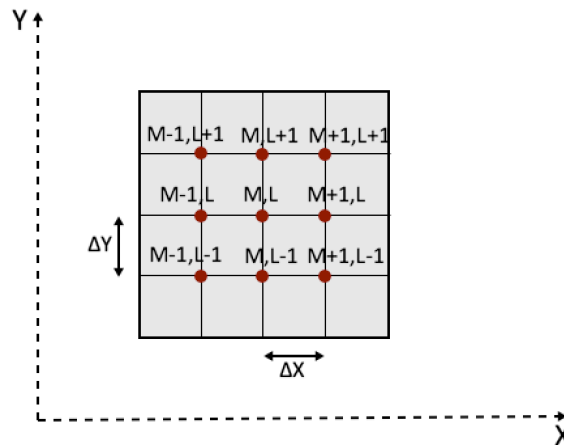


Figure 3.25: Grid points in XY plane

While considering the relations given for backward and forward approximations, given in section 2.6.3, partial derivatives in X, Y and XY directions can be obtained. These approximations will be implemented when central approximation is not applicable. Such as at grid points located on the edge of the grid.

For a given suction across the interface, this transforms the problem into a system of non-linear equations where Z's of grid points (z_p) are unknowns and each point has an equation from the finite difference approximation of either 3.50 or 3.51. These equations are solved with application of Newton-Raphson (Jacobian) method.

3.4.4 Newton-Raphson (Jacobian) Method

For a given suction value, the location of air-water interface (grid) inside the pore throat should be determined. The boundary condition imposes a unique air-water surface at equilibrium for each value of suction. The AEP of pore throat will be obtained when the air-water surface curvature and its contact angle with particles surface cannot reach equilibrium. Otherwise, the interface is able to withstand the pressure differences and the air cannot penetrate into the pore medium located below the air-water surface. While considering the Z coordinates of grid points (z_p) as only variable, the Newton-Raphson (Jacobian) equation given by Eq. (2.52) can be modified as written.

$$\begin{bmatrix} z_p^{a+1}(1,1) \\ z_p^{a+1}(1,2) \\ \vdots \\ z_p^{a+1}(A+1,A+1) \end{bmatrix} = \begin{bmatrix} z_p^a(1,1) \\ z_p^a(1,2) \\ \vdots \\ z_p^a(A+1,A+1) \end{bmatrix} - J^{-1} \begin{bmatrix} f(z_p^a(1,1)) \\ f(z_p^a(1,2)) \\ \vdots \\ f(z_p^a(A+1,A+1)) \end{bmatrix} \quad (3.53)$$

where, J^{-1} is,

$$J^{-1} = \begin{bmatrix} \frac{\partial f(z_p^a(1,1))}{\partial z_p^a(1,1)} & \frac{\partial f(z_p^a(1,1))}{\partial z_p^a(1,2)} & \dots & \frac{\partial f(z_p^a(1,1))}{\partial z_p^a(A+1,A+1)} \\ \frac{\partial f(z_p^a(1,2))}{\partial z_p^a(1,1)} & \frac{\partial f(z_p^a(1,2))}{\partial z_p^a(1,2)} & \dots & \frac{\partial f(z_p^a(1,2))}{\partial z_p^a(A+1,A+1)} \\ \vdots & \vdots & \ddots & \vdots \\ \frac{\partial f(z_p^a(A+1,A+1))}{\partial z_p^a(1,1)} & \frac{\partial f(z_p^a(A+1,A+1))}{\partial z_p^a(1,2)} & \dots & \frac{\partial f(z_p^a(A+1,A+1))}{\partial z_p^a(A+1,A+1)} \end{bmatrix}^{-1}$$

, a is number of iterations, and $f(z_p)$ is obtained from either Eq. (3.50) or Eq. (3.51). (Depends on type of grid points; Curvature or boundary). Note that at $a=1$, the coordinates of grid points are same as given in Eq. (3.41). (i.e. coplanar with centers of the three particles)

3.4.4.1 Convergence of Newton-Raphson Method

As mentioned, the location of grid points will determine if a point is a boundary or curvature point. As a result of iteration process of Newton-Raphson method, properties of points are changeable. In other words, if in the first iteration a point is a boundary point, in the next iteration this point can change to curvature point (GP₁ in Figure 3.26). In order to fulfill the contact angle criterion, in beginning of second iteration, Z coordinates of GP₂ is altered and considered to be equal to Z coordinates of GP₁. This will preserve the boundary condition at particle-air-water interface.

Unavailability of stationary boundaries leads to inability of convergence with Newton-Raphson method. To this end, the C parameter is defined. When an iteration number is divisible by C , boundary points are considered as fixed points. As a result, curvature points will start to converge with respect to fixed boundary points. The effect of C value on AEP acquisition process of pore throats is studied and presented in section 3.4.5.2. With increasing the C value, the processing time for determining the AEP of a single pore throat is increased. However, smaller C values will lead to invalid AEP of

pore throats. When C is considered to be 5, the reliable results in reasonable period of time are obtained.

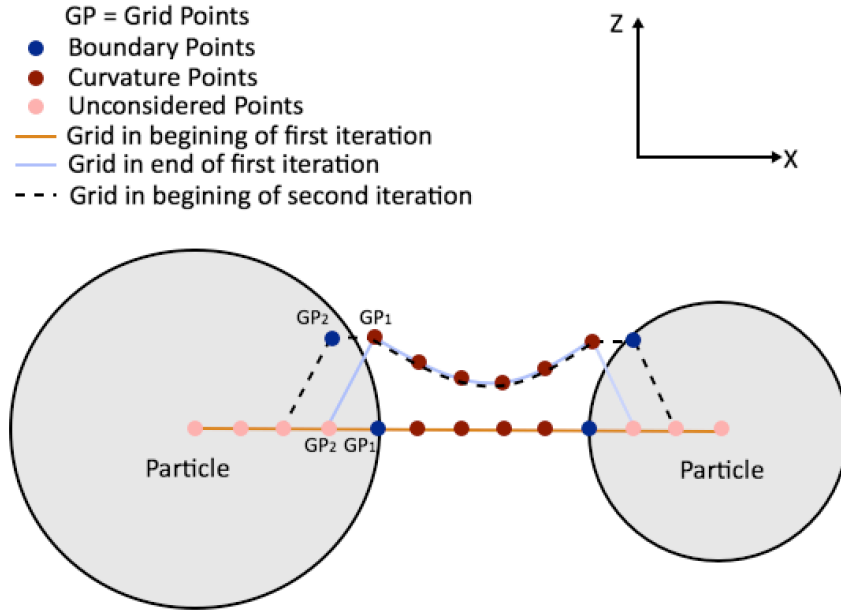


Figure 3.26: Properties of grid points after each iteration

Another issue causing the divergence of Newton-Raphson method is related to the limitation in Z coordinates. In each iteration, if a grid point locates out of the pore throat domain it will lead to divergence of proposed method. This is because of the fact that properties of points are determined in regard to their location in pore throat. To eliminate this problem, D parameter, which is under-relaxation factor, is integrated to Newton-Raphson equation as written by,

$$\left[Z_p^{a+1} \right] = \left[Z_p^a \right] - D \cdot J^{-1} \left[F(Z_p^a) \right] = \left[Z_p^a \right] - D \cdot \left[F_w \right] \quad (3.54)$$

where, D is,

$$D = \frac{R_{\min}}{50 \cdot \left| F_w \right|_{\max}}$$

, R_{\min} is minimum radius of particles forming the pore throat, and $|F_w|_{\max}$ is maximum absolute value of F_w . The D parameter prevents sudden changes in Z coordinates between two iterations. This parameter considers various sizes of pore throat media with integrated R_{\min} parameter. Meanwhile, in each iteration its value is distinct due to changes in maximum absolute value of F_w . With application of this parameter, the grid points will stay inside the pore throat region as long as they can converge (i.e. reach equilibrium).

Eventually, the iteration will stop if most of the grid points have $f(z_p) < 0.01$ (more than 90% of curvature and boundary points) or start to locate out of the pore throat region. In the first case, the air-water surface was able to reach the equilibrium for the given suction, and suction can be increased to the next level. However, in second case, the contact angle is not satisfied and grid points started to move out of the pore throat region in order to reach equilibrium. In this case, the current suction value is AEP of considered pore throat.

3.4.5 Parametric Study

3.4.5.1 Effect of B Variable on AEP Results

As mentioned in section 3.4.1, the number of grid intervals (A) is defined in a way that they can cover pore throat regions with minimum number of points (B). Here, the effect of B parameter on AEP of a single pore throat, which is developed between three particles with diameter range of 125-150 μm , is presented. The contact angle between air-water interface and particles surface is considered to be 30 degrees. The results of AEP of this pore throat with various B values (varying from 10 to 200) are presented in Table 3.5. The C parameter defined in section 3.4.4.1 is equal to 5.

As it can be observed from Table 3.5, with increasing the B value the computing time is increased. After B=50, not only the changes in AEP of the pore throat are small, but

also the computing time is increased significantly. Therefore, the optimum value of B is estimated to be 50.

Table 3.5: Effect of B variable on AEP results and average computing time

B	A	AEP (kPa)	Average computing time for single suction value (s)
10	10	5.01	1.08
20	14	3.58	1.86
30	16	4.03	1.1
40	18	3.96	1.8
50	20	4	2.1
60	22	4.09	4.64
70	24	4.05	5.2
80	26	4	6.54
100	30	3.98	7.32
150	38	4.02	10.73
200	46	4.01	13.5

3.4.5.2 Effect of C Variable on AEP Results

According to section 3.4.4.1, the C parameter speeds up the convergence of Newton-Raphson method by fixing the boundary points when iteration number is divisible by C. While considering the same pore throat as previous section, the effect of C on AEP results and average time for reaching the equilibrium (for an applied suction) is studied and presented in Table 3.6. The optimum B parameter obtained from previous section is considered (B=50). According to Table 3.6, the optimum value of C is 5. When C is larger than this value, the computing time is increased significantly.

For three suction values, resulting air-water surfaces of the pore throat are presented in Figure 3.27. In this figure, the B parameter is 200 and C is 5. In Figure 3.27c, the air-

water surface fails to reach the equilibrium and as a result this suction value (4.01 kPa) is AEP of the pore throat.

Table 3.6: Effect of C variable on AEP results and average computing time

C	AEP (kPa)	Average computing time for single suction value (s)
1	3.81	0.53
2	4.01	0.87
3	4.12	1.3
5	4	2.1
10	3.98	3.3
20	4.01	3.5
50	4.04	3.65

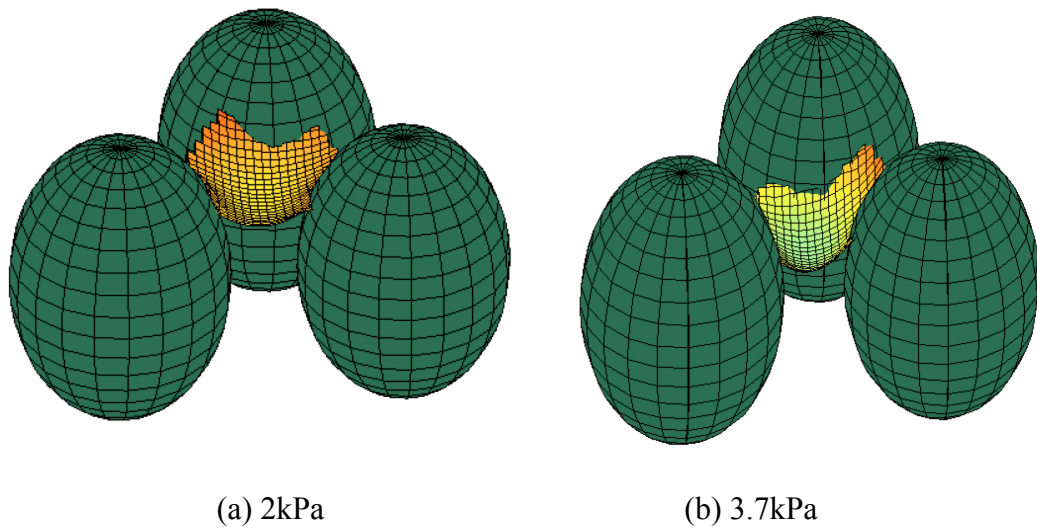
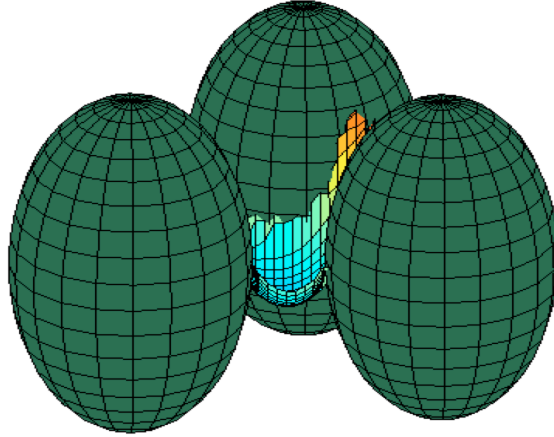


Figure 3.27: The air-water surfaces when the applied suction is (a) 2, (b) 3.7 and, (c) 4.01 kPa



(c) 4.01 kPa (AEP of pore throat)

Figure 3.27: Continue

3.5 Drainage of Simulated Medium

To begin with drainage process, simulated cubic medium is considered to be saturated. Thus, the air-water interface is located in upper boundary of the medium ($Z= b$). The total volume of voids (V_v) is,

$$V_v = V_t - V_s = V_w + V_a \quad (3.55)$$

where, V_t and V_s are given in Eq. (3.23) and Eq. (3.25), respectively, V_w is total volume of pore water, and V_a is total volume of pore air. In saturation state, $V_a=0$.

The Side-Points will represent the content of pores: water or air. As shown in Figure 3.28, first bulk pore BP_1 contains air and rest of the bulk pores contain water. If the suction value passes the AEP of first throat plane (TP_1), which is located at air-water interface, bulk pore BP_2 will drain and air will penetrate inside considered pore. In this case, TP_2 and TP_5 will be subjected to air and all of the Side-Points located inside bulk

pore BP₂ will represent the air compound. Continuing the described procedure will gradually expel the water from simulated medium.

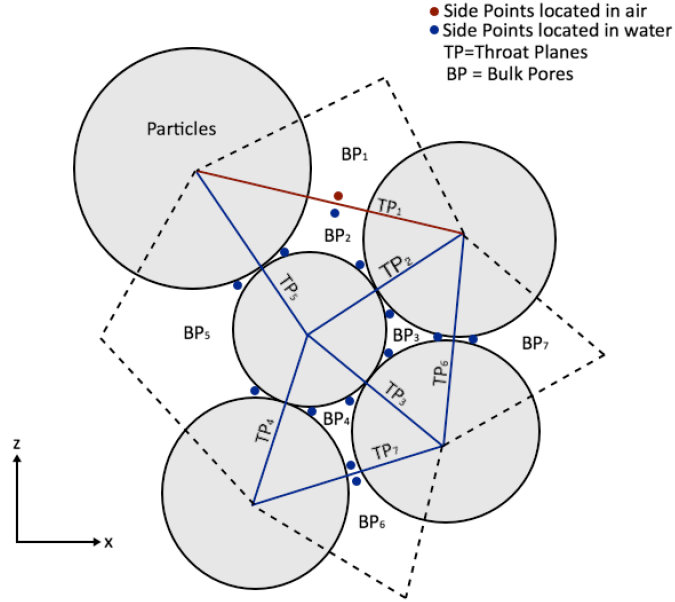


Figure 3.28: Schematic of drainage process

When a pore throat fails to reach the equilibrium, its mirrored pore throats will fail as well. Although, the water volume in the bulk pores located outside of the considered cubic medium are not included in the total water content calculation, drainage of these pores needs to be simulated in order to provide the penetration of air from sides of cubic medium.

While considering the location of pore throats, the amount of suction ($u_a - u_w$) in each pore throat must be superposed with hydrostatic pressure. The water pressure at considered pore throat will be determined. To this end, the Z coordinates of Side-Point (z_m), which is located on considered pore throat, will be utilized. For a Side-Point of i , the water pressure is,

$$u_w (\text{Pa}) = 9.8 \times z_m (i)(\text{mm}) \quad (3.56)$$

The size of suction interval is one of the main factors to decrease or increase the computing time. In this regard, this parameter is considered as one of the input variables of the algorithm. In order to develop logarithmic suction intervals, suction multiplier (s_m) variable is defined. As a result, the suction interval (s_I) is function of s_m as well as minimum (s_{min}) and maximum (s_{max}) applied suctions, which are also considered as input of the algorithm, as given by,

$$S_I = 0 : \log_{s_m} \left(\frac{S_{max}}{S_{min}} \right) \quad (3.57)$$

Therefore, the applied suction value (ψ) is equal to,

$$\psi = S_{min} \cdot (S_m)^{S_I} \quad (3.58)$$

Note that $S_{min} \neq 0$ and $S_m \neq 1$.

While applying the constant suction, if all of the pore throats in air-water interfaces reach the equilibrium, the total volume of remaining water (V_R) in medium will be determined.

$$V_R = V_v - V_B + V_P \quad (3.59)$$

where, V_v is total volume of voids, V_B is volume of drained bulk pores, and V_P is total volume of developed pendular rings.

The proportion volume of drained bulk pores is attained with Delaunay triangulation function. In the proposed method in section 3.3.4, the volume of tetrahedron forming from Side-Points is ascribed to each bulk pore. In order to normalize the volume of tetrahedrons in respect to total volume of voids, the following relation is considered.

$$V_B = \frac{V_v}{\sum_{i=1}^{N_b} v_B(i)} \cdot \sum_{j=1}^{N_d} v_B(j) \quad (3.60)$$

where, v_B is volume of each bulk pore given in Eq. (3.36), N_b is total number of defined bulk pores, and N_d is total number of drained bulk pores.

As bulk pores are drained, pendular rings develop. The volume of pendular ring is calculated with Eq. (3.39). As mentioned in section 3.3.5.1, the connectivity of pendular rings to bulk pores is determined. In this regard, for a single pendular ring, properties of connected bulk pores are considered. If a pendular ring surrounded by total amount of a_1 bulk pores and only a_2 of them is drained, the volume of pendular water is approximated as,

$$v_p = (V_1 - V_2) \cdot \left(\frac{a_2}{a_1} \right) \quad (3.61)$$

where, V_1 and V_2 are given in Eq. (2.32) and Eq. (2.35), respectively. Eventually, the total volume of developed pendular rings is,

$$V_p = \sum_{i=1}^{N_p} v_p(i) \quad (3.62)$$

where, N_p is total amount of identified pendular rings. The degree of saturation (S) in the end of each suction increment is equal to,

$$S = \frac{V_R}{V_v} \quad (3.63)$$

In additional, the gravimetric water content (ω) of medium can be determined.

$$\omega = \frac{e \cdot S}{G_s} \quad (3.64)$$

where, G_s is specific gravity, and e is void ratio of simulated medium. Eventually, the SWCC can be plotted in terms of suction versus gravimetric or volumetric water content as well as suction versus degree of saturation.

3.6 User Interface

In this section, input variables as well as main outputs of the developed algorithm are defined. The Matlab code of the algorithm is given in Appendix CD.

3.6.1 Input Variables of the Algorithm

Initially, the variables presenting physical properties of soils will be defined. The particle size distribution of any soil is represented with “Mass_Percent” and “Diameter” matrices. The “Mass_Percent” matrix is mass percent of particles finer than corresponding sieve diameters (“Diameter”). The unit of “Diameter” is millimeters. The target void ratio of specimen is presented with “e_target”. The contact angle of particle-air-water interface and surface tension of air-water interface are shown with “contact_angle” and “surface_tension” variables, respectively. The unit of “surface_tension” is N/mm. The specific gravity of particles is shown with “Gs”. The “dry_density” variable is dry density of considered specimen (g/cm^3).

Afterwards, the variables that can affect the outcome of the results should be defined. The variable “n(1)” is assumed number of the particles in coarsest segment of PSD. While considering non-uniform soils it is highly recommended to define this variable to be less than 10. Otherwise, the total number of particles will be too large and it will take days to simulate the SWCC.

The density factor (D_f), which is defined in section 3.2.2.4, is shown with “Density_Factor”. In order to pack a dense medium, this parameter should be equal to 1. The algorithm will increase this value if looser medium is considered. The minimum and maximum applied suctions are presented with “Minimum_Suction” and “Maximum_Suction” variables, respectively. The unit of these variables should be in Pa. The suction multiplier (s_m) is also given as input of the program (“Suction_Multiplier”). The value of this parameter is recommended to be between 1 and 2 (Note that $S_m \neq 1$).

3.6.2 Outputs of the Algorithm

The X, Y, and Z center coordinates of simulated particles and their radii are sorted in “x”, “y”, “z”, and “r” matrices, respectively. The “e” variable represents the void ratio of simulated medium. The PSD of simulated cubic medium is given in “Mass_Percent_Simulated” and “Diameter_Simulated” matrices. The “Total_Particles” variable is total number of packed and mirrored particles. The “Generated_Particles” only represents the packed particles. The total number of particles in cubic medium, which is considered to be saturated, is shown with “Sample_Particles”. The identified pore throats of medium are shown with MATLAB cell of “Pore_Throat”. Each matrix in the cell contains the id numbers of the three particles forming the pore throat. The X, Y, and Z coordinates of generated Side-Points are shown with “xm”, “ym”, and “zm” matrices, respectively. A matrix named “Pore” shows the number of bulk pores of each Side-Point. The “Pore_Volume_Normalized” matrix contains the normalized volume of each bulk pore with regard to total volume of voids. The “Pendular_Ring” cell contains the list of particle pairs between which a pendular ring can be developed. The gravimetric and volumetric water content of medium after each suction increment is presented with “Water_Content_Gravimetric” and “Water_Content_Volumetric” matrices, respectively. The applied suctions are shown with “Applied_Suction” matrix. Eventually, the simulated SWCC are plotted in terms of gravimetric and volumetric water content versus suction.

CHAPTER 4

INTERPRETATION AND COMPARISON OF RESULTS

With application of the proposed algorithm, defined in previous chapter, the SWCC of soils comprised of sand and silt particles are determined. In this regard, parametric SWCC results as well as comparison of the obtained SWCC with experimental and empirical results are presented in this chapter. Throughout the calculation procedure, surface tension of air-water interface is assumed to be constant. ($\sigma_{st} = 72.8 \times 10^{-3} \text{ N/m}$)

4.1 Parametric Results

The drying SWCC is basically a function of three factors: (i) Particles size, (ii) void ratio (e), and (iii) contact angle (θ). Here, effects of each factor on the SWCC outcomes are presented.

4.1.1 Effect of Particles Size on Simulated SWCC

Different particle sizes will result in distinct SWCC. Generally, soils consist of finer particles will result in greater AEP. This is due to the inverse relation between size of the pore throat and AEP. While considering the particle size as the only variable, SWCC of three uniform specimens with approximately similar void ratios ($e \approx 0.62$) and contact angles ($\theta = 30$) are obtained. The uniform specimens with diameter range of 250-300, 125-150 and 53-75 μm are generated using the proposed algorithm. According to physical properties of glass beads with same diameter ranges given by Toker (2002) (section 4.2.1), the specific gravity (G_s) of particles is assumed to be

2.43. Figure 4.1 presents the SWCC of these three samples wherein the inverse relation between AEP and particle size is visualized.

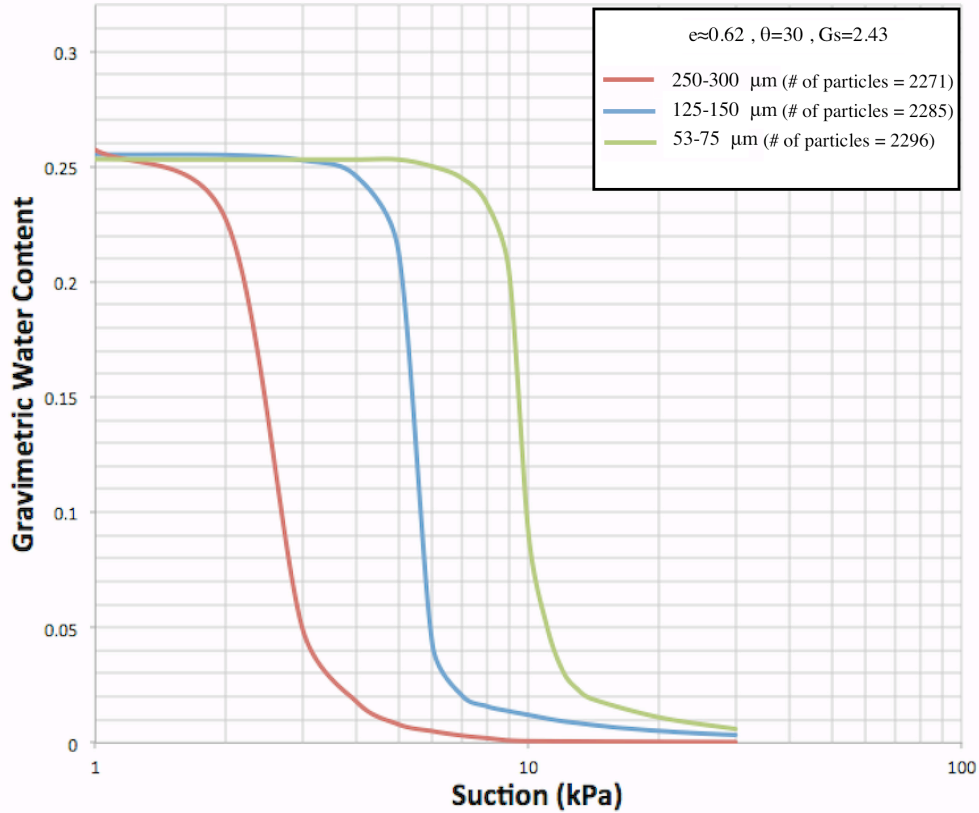


Figure 4.1: Effect of particles size on SWCC

4.1.2 Effect of Void Ratio on Simulated SWCC

While considering loose soils, particles will have greater distances among them. Therefore, the AEP of soil medium will be lower. In this regard, three specimens with different void ratios are simulated. The diameter ranges of particles are identical (125-150 μm). The void ratios of simulated media are 0.81, 0.72 and 0.62. The contact angle and specific gravity of all three specimens are 30° and 2.43, respectively. The impact of void ratio on SWCC results is illustrated in Figure 4.2. The specimen with smaller void ratio yielded in greater AEP. Furthermore, decreasing the void ratio also leads to steeper SWCC.

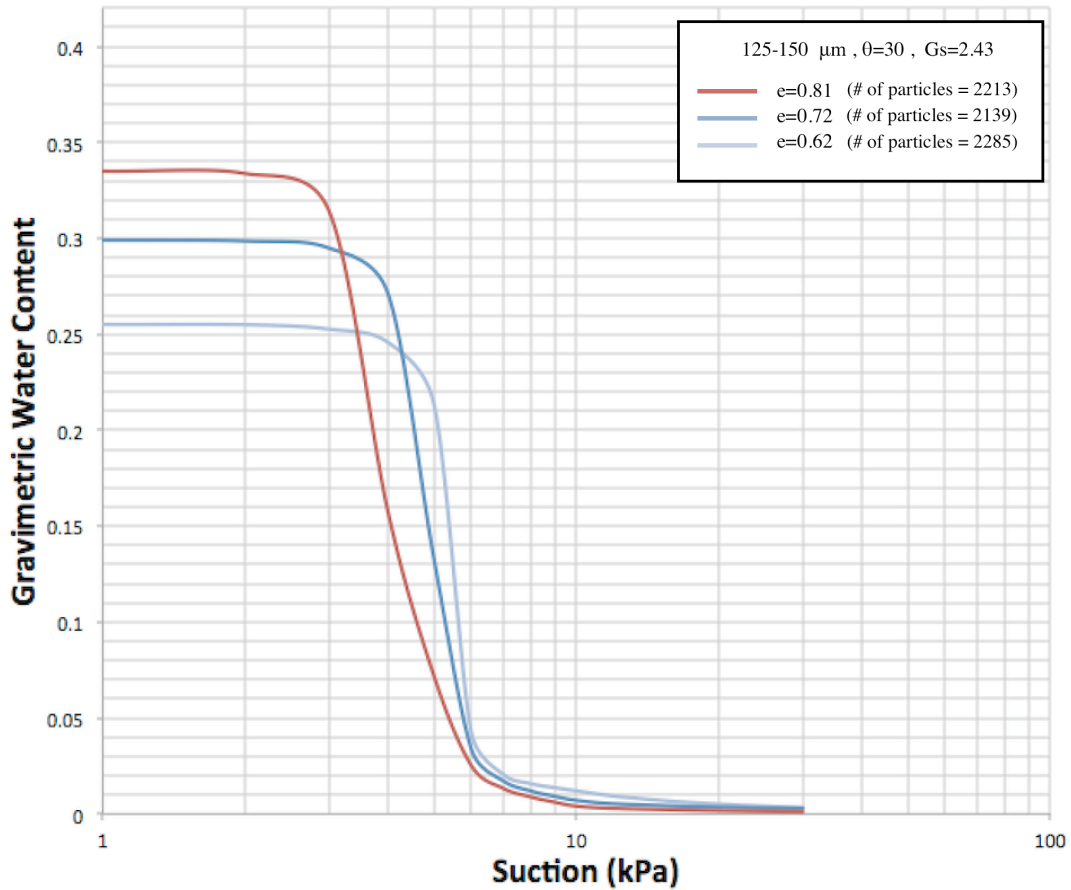


Figure 4.2: Effect of void ratio on SWCC

4.1.3 Effect of Contact Angle on Simulated SWCC

Another criterion that can alter SWCC outcome is contact angle at particle-air-water interface. In this research, the contact angle is considered to vary between 0 to 30 degrees. However, the methodology is applicable to different angles. The AEP of pore throats and volume of pendular rings are functions of contact angle. The contact angle has an inverse relation with AEP and volume of pendular rings. The effect of contact angle on AEP of pore throats and volume of pendular rings is shown in SWCC results. The SWCCs of a uniform specimen with particles diameter range of 125-150 μ m in different contact angles is determined. The void ratio and specific gravity of medium is 0.62 and 2.43, respectively. Figure 4.3 presents the SWCC of a simulated medium for contact angles of 0, 10, 20 and 30 degrees. The AEP of specimen with lower

contact angle is higher. Meanwhile, increasing the contact angle will also lead to steeper SWCC.

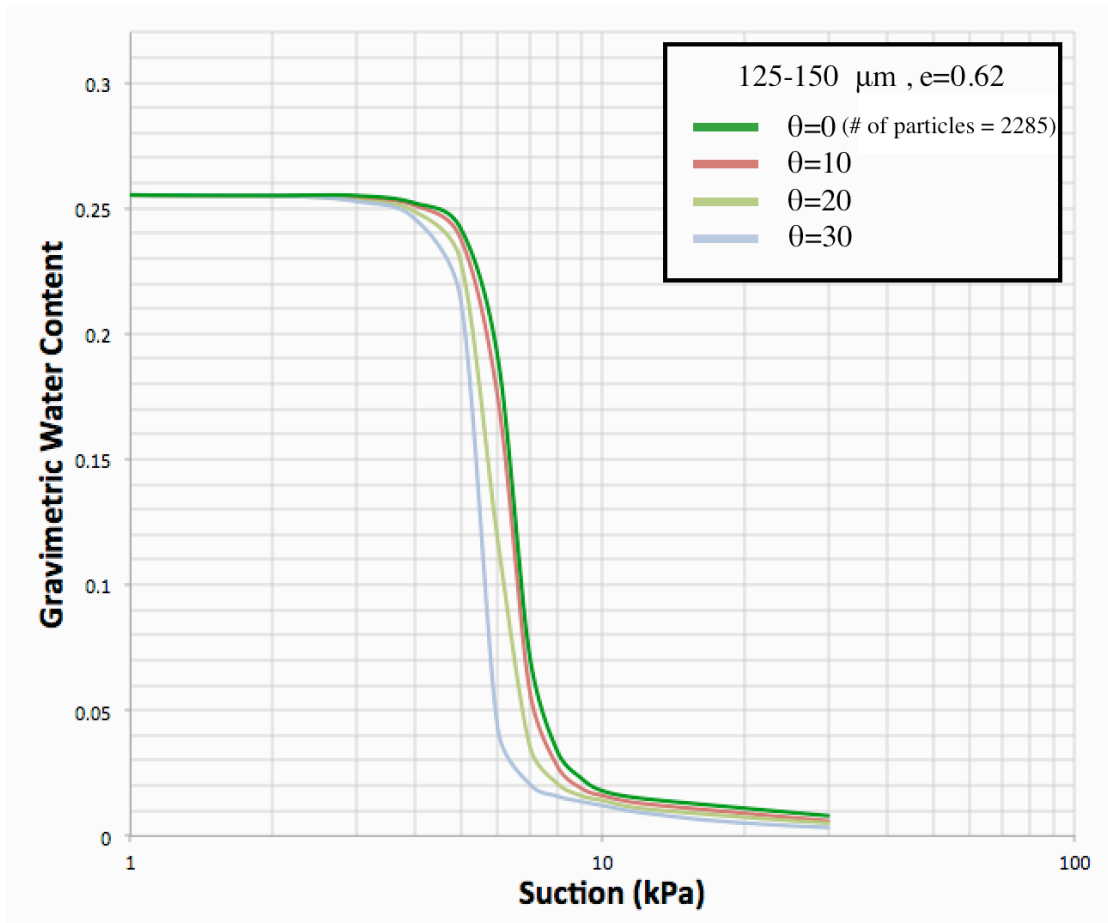


Figure 4.3: Effect of contact angle on SWCC

4.2 Verification Using Experimental Results of Spherical Particles

The simulated soil media consist of spherical particles. Therefore, for a realistic comparison, laboratory results of specimens consist of glass beads are considered.

4.2.1 Material Properties

Toker (2007) determined the SWCC of specimens consist of two different types of glass beads with MIT method (section 2.5.2.3). The first type of glass beads that are

mostly uniform are noted as Type 1 and processed from mixture of beads, found in MIT geotechnical laboratory. The specific gravity (G_s) of these glass beads is 2.43 (Sjoblom, 2000), which indicates the mixture of borosilicate (2.2) and sodalime (2.57) glass beads. Meanwhile, the second types of glass beads, which are perfectly uniform, were purchased from different resource. These glass beads are noted as Type 2 and the specific gravity of these borosilicate beads is 2.2.

The first specimen consists of Type 1 glass beads with diameter range of 106-125 μm . Meanwhile, the second specimen was prepared with Type 2 glass beads and similar diameter range. The microscopic photographs of these glass beads are shown in Figure 4.4. According to this figure, the Type 1 glass beads consists of finer particles that proofs its non-uniformity.

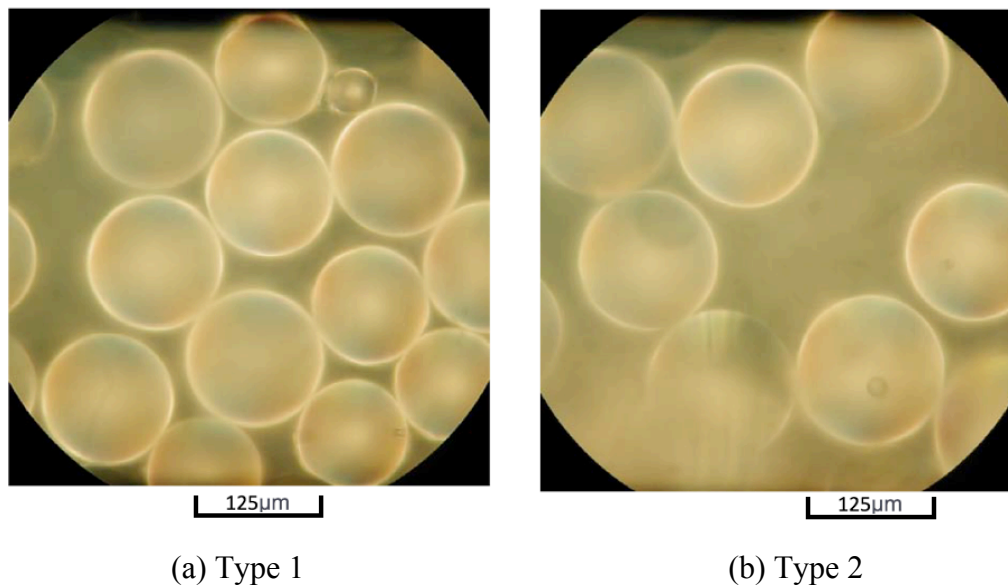


Figure 4.4: Microscopic photographs of (a) Type 1 and, (b) Type 2 glass beads (Toker, 2007)

The SWCCs of specimens consist of Type 1 and Type 2 glass beads, which are determined by Toker (2007), are shown in Figure 4.5.

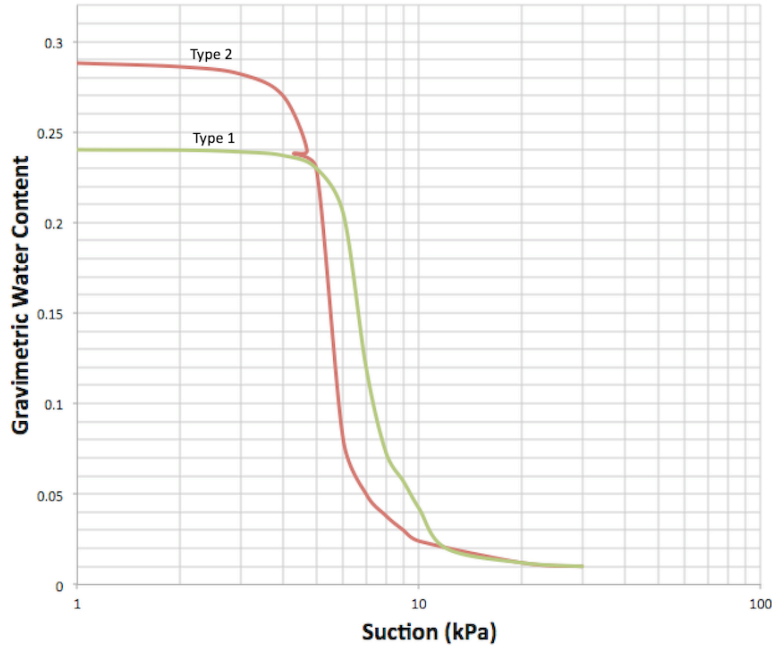


Figure 4.5: SWCC of mostly uniform (Type 1) and perfectly uniform (Type 2) specimens (Toker, 2007)

According to experimental SWCC data, the void ratio of each specimen can be calculated with following equation.

$$e = \omega_{\text{Sat}} \cdot G_s \quad (4.1)$$

where, e is void ratio of specimen, and ω_{Sat} is gravimetric water content at saturation ($S=1$). The e and ω_{Sat} of Type 1 and Type 2 glass bead specimens are calculated and presented in Table 4.1.

Table 4.1: Physical properties of specimens presented by Toker (2007)

Specimen	Diameter Range (μm)	Glass Beads	G_s	ω_{sat}	e
Mostly Uniform	106-125	Type 1	2.43	0.24	0.583
Perfectly Uniform	106-125	Type 2	2.2	0.288	0.633

Back in 2002, Toker succeeded to obtain the SWCC of mostly uniform soils, which consist of glass beads of Type 1, with application of MIT method. In conducted tests, the glass beads were separated into fractions with following diameters (μm): 250-300, 125-150, and 53-75. The SWCC of specimens are composed of these fractions are presented in Figure 4.6.

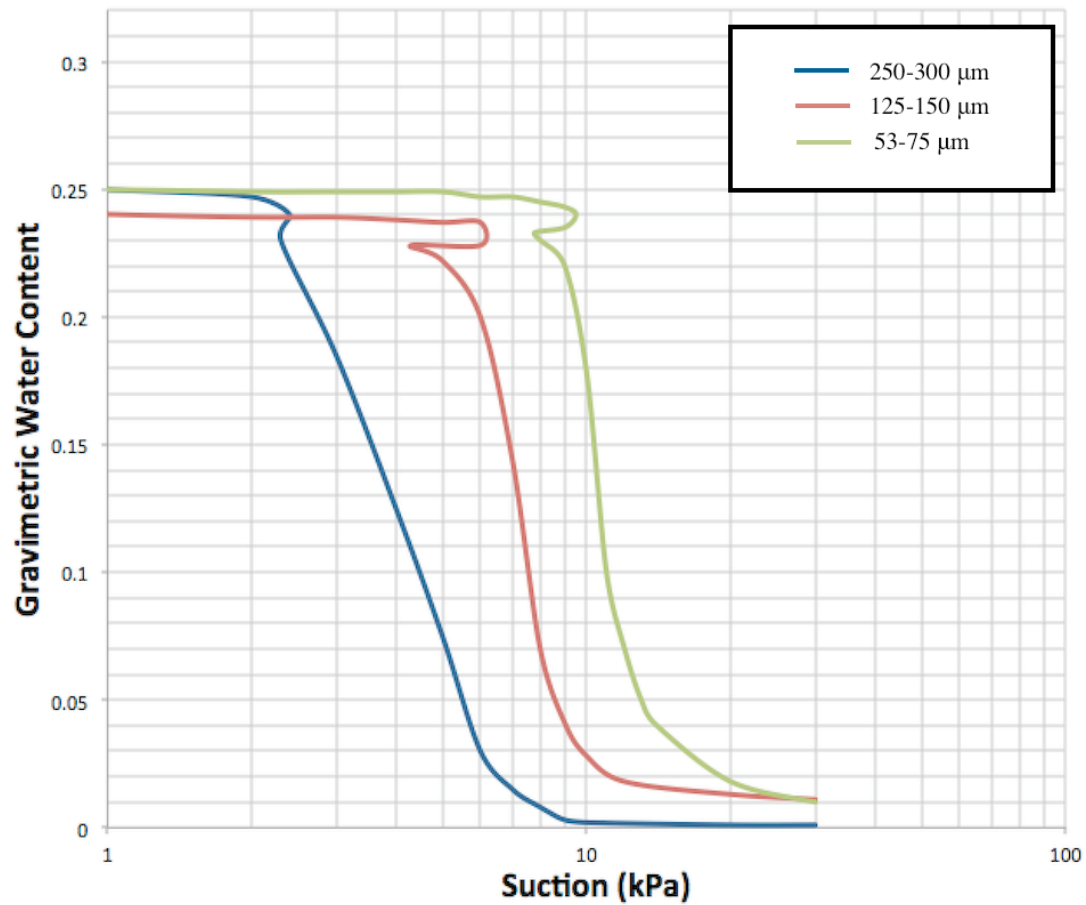


Figure 4.6: SWCC of mostly uniform specimens (Toker, 2002)

With regard to Figure 4.6 and Eq. (4.1), the void ratio and gravimetric water content of specimens at saturation are determined and presented in Table 4.2. (Note that G_s of Type 1 glass beads is 2.43)

Table 4.2: The ω_{sat} and e of mostly uniform specimens presented by Toker (2002)

Diameter Range of Specimens (μm)	ω_{sat}	e
250-300	0.252	0.61
125-150	0.24	0.583
53-75	0.251	0.609

According to Toker (2002), gap-graded specimens are comprised of two fractions. The size fractions of 250-300 μm and 53-75 μm are called coarse and fine fractions, respectively. Different ratios of these fractions resulted in different gap-graded specimens. The SWCCs of gap-graded specimens given by Toker (2002) are presented in Figure 4.7. According to this figure and Eq. (4.1), the void ratio and gravimetric water content of these specimens are determined (Table 4.3).

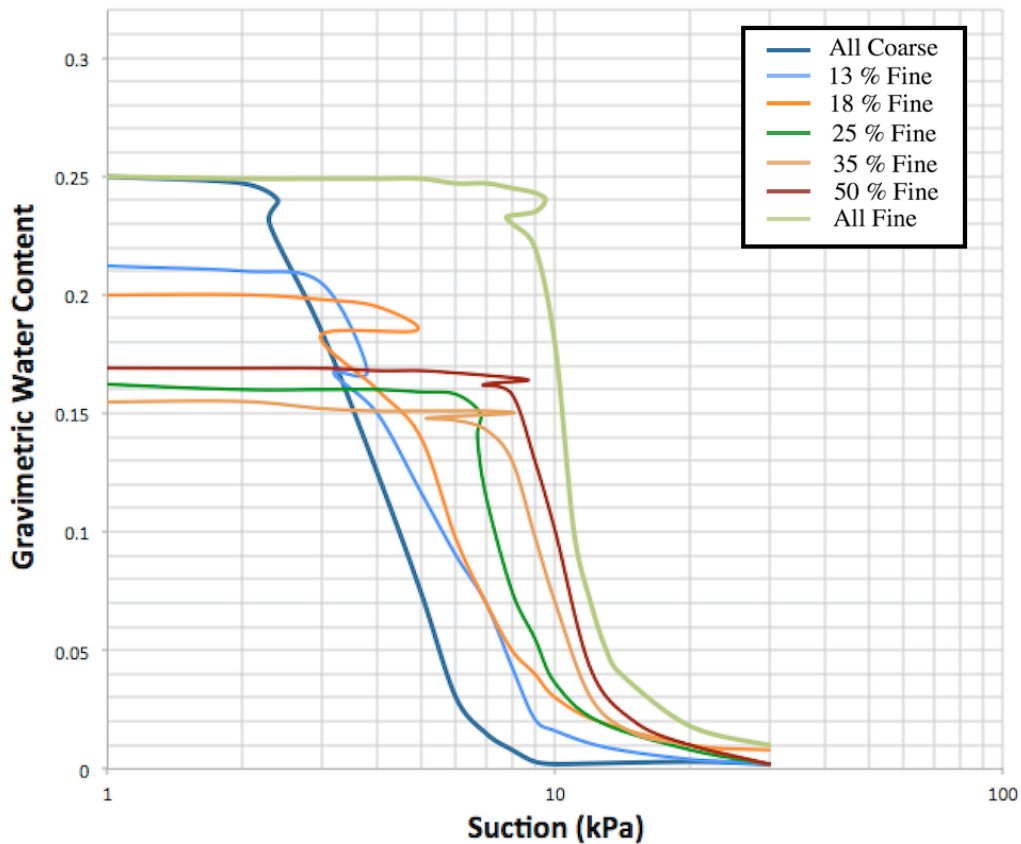


Figure 4.7: SWCC of gap-graded specimens (Toker, 2002)

Table 4.3: The ω_{sat} and e of gap-graded specimens presented by Toker (2002)

Coarse % (250-300 μm)	Fine % (53-75 μm)	ω_{sat}	e
87	13	0.212	0.515
82	18	0.201	0.488
75	25	0.162	0.393
65	35	0.154	0.374
50	50	0.171	0.415

4.2.2 Interpretation of Experimental SWCC Data

Generally, perfectly uniform soils will lead to steeper slopes of SWCC, which is the case in SWCC of Type 2 glass beads (Figure 4.5). While considering Figure 4.6, the SWCC of specimens with diameter range of 250-300 and 125-150 μm have moderate slopes. This indicates the non-uniformity of prepared specimens. Figure 4.8 proves the existence of finer particles in specimen prepared from fractions of 125-150 μm . As it can be observed from this figure, the specimen with particles diameter range of 125-150 μm (Type 1) has greater AEP in comparison to perfectly uniform specimen with finer particles (106-125 μm). In this regard, the fractions with diameter range of 250-300 and 125-150 μm consist of finer particles. For a fraction of 250-300 μm , 10% (mass) of particles are assumed to have diameter ranges between 150-200 μm . Similarly, for a fraction of 125-150 μm , 20% (mass) of particles are assumed to have diameter ranges between 90-125 μm . With application of proposed algorithm this assumption is verified (section 4.2.3). With regard to this assumption, the PSD of gap-grades specimens given by Toker (2002) in Table 4.3 also consists of particles in diameter range of 150-200 μm . The considered PSDs of gap-graded specimens for simulation are given in Figure 4.9.

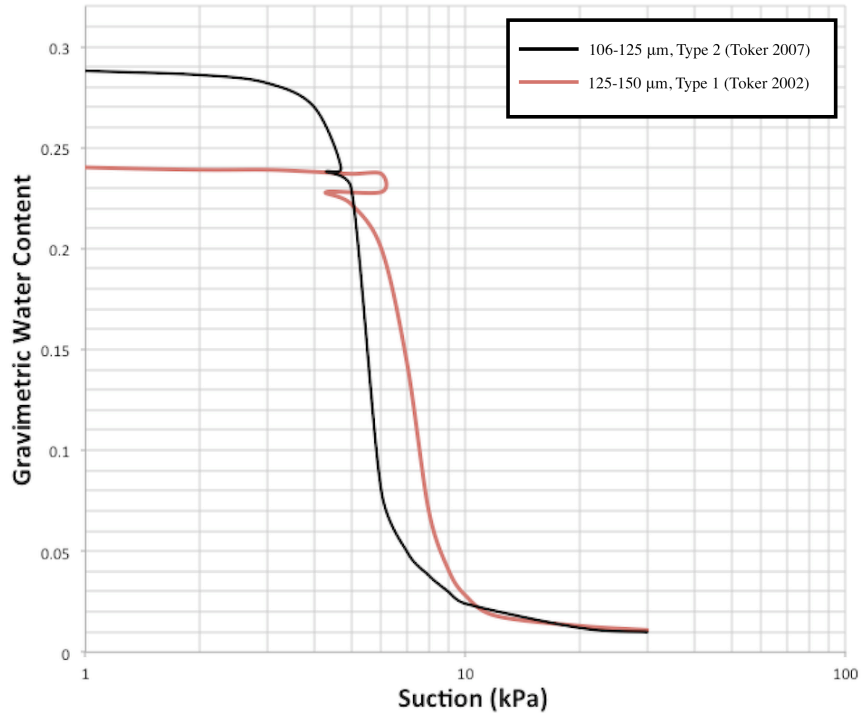


Figure 4.8: Comparison of SWCC of mostly uniform (Type 1) and perfectly uniform (Type 2) specimens given by Toker (2002, 2007)

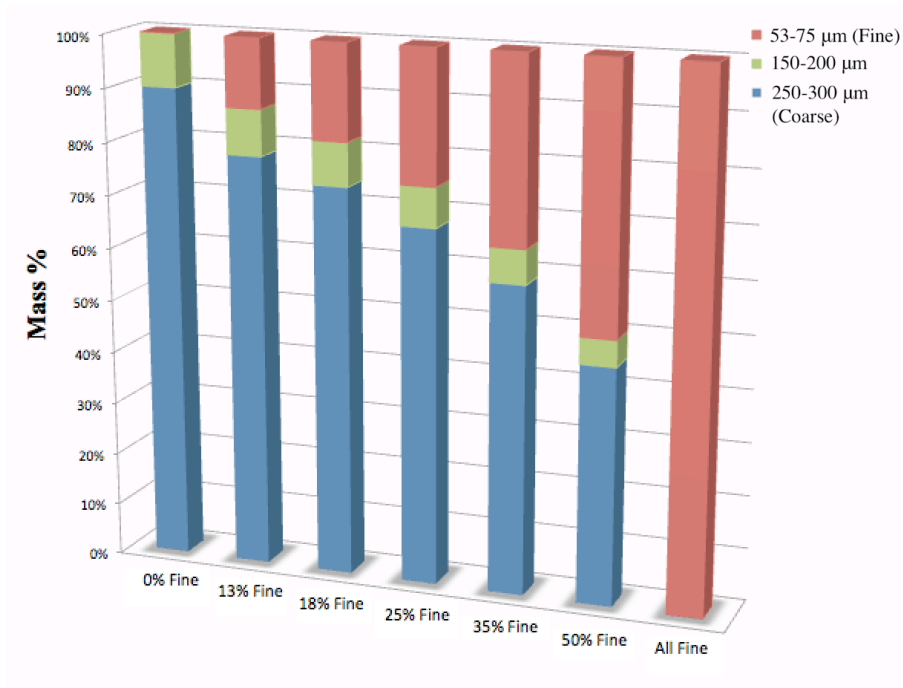


Figure 4.9: PSD of gap-graded specimens with modified fractions

4.2.3 Simulated SWCC Results of Glass Beads

Initially, the SWCC of perfectly uniform specimen consist of Type 2 glass beads (Toker, 2007) is simulated. The diameter range of particles, specific gravity and void ratio of considered perfectly uniform specimen given by Toker (2007) are presented in Table 4.1. To begin with, spherical particles are generated in considered diameter range (106-125 μm). When the void ratio of simulated medium is in acceptable tolerance of objective void ratio (Eq. 3.27) the packing procedure is stopped. Eventually, the void ratio of simulated medium is obtained as 0.64. While considering various contact angles, the best result is obtained at 20 degrees. Comparison of the experimental and simulated SWCC results is depicted in Figure 4.10. The AEP and slope of the simulated SWCC is slightly different from experimental results. Small differences in void ratio can result in this difference.

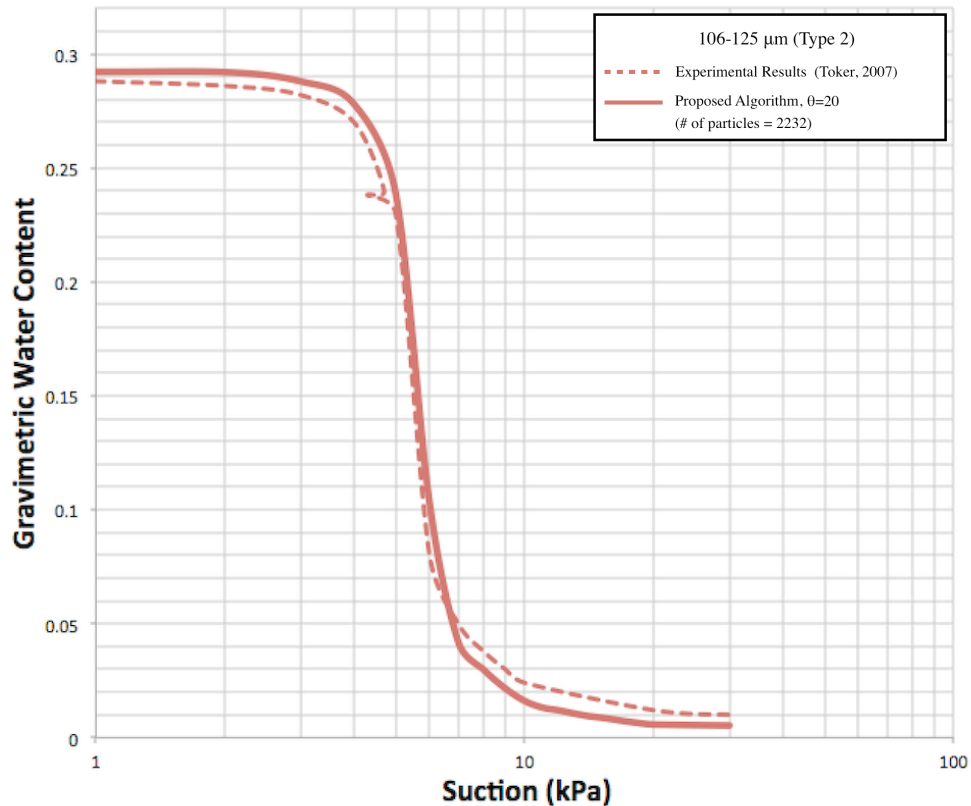


Figure 4.10: Comparison of simulated SWCC with experimental results given by Toker (2007)

Afterwards, the SWCCs of mostly uniform specimens consist of Type 1 glass beads (Toker, 2002) are simulated. The diameter range of particles, specific gravity and void ratios of prepared specimens by Toker (2002) are presented in Table 4.2. Due to non-uniformity of prepared specimens by Toker (2002), the target void ratio of specimens consist of particles with diameter range of 250-300 μm and 125-150 μm is not satisfied. The simulated SWCC of generated specimens with exact fractions given by Toker (2002) are illustrated in Figure 4.11. As it can be visualized the simulated SWCCs have steeper slopes, which is the case in perfectly uniform specimens.

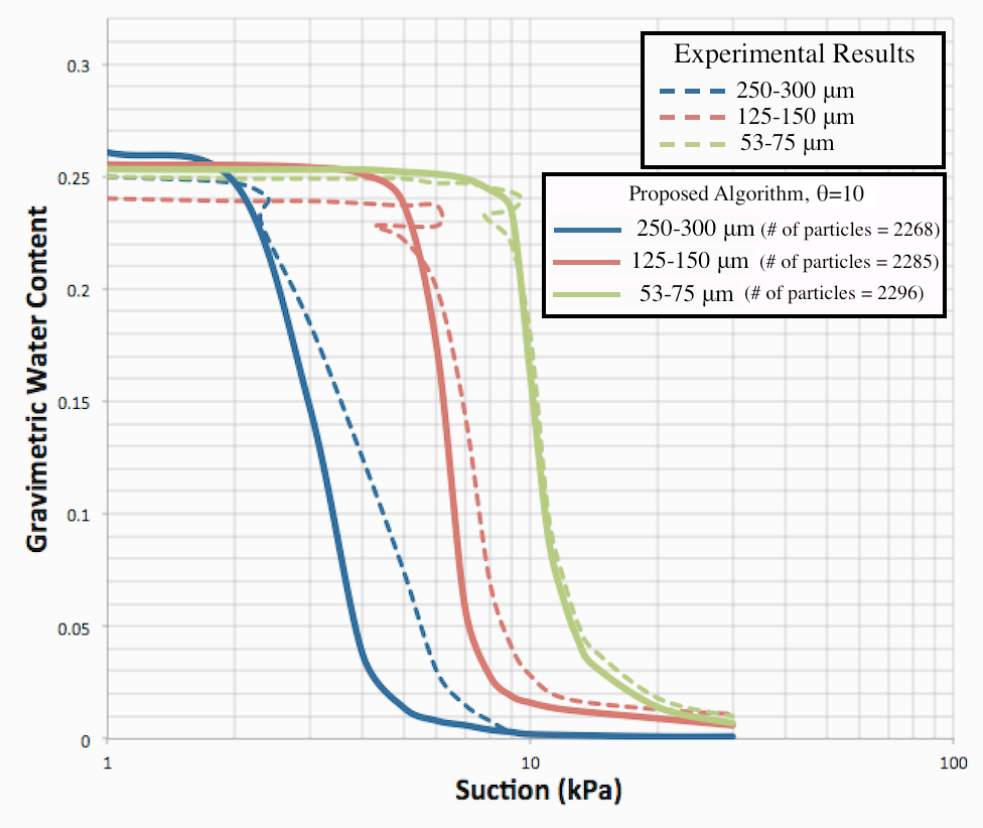


Figure 4.11: Comparison of simulated SWCC with experimental results given by Toker (2002)

However, assumption of finer particles in these fractions (section 4.2.2) leads to satisfaction of target void ratio. Therefore, the specimens composed of modified fractions of 250-300 and 125-150 μm are simulated. Figure 4.12 shows the simulated

SWCC of these specimens when θ is 10. With modification of fractions, not only the void ratio criterion is satisfied, but also the simulated SWCC concurs with experimental results.

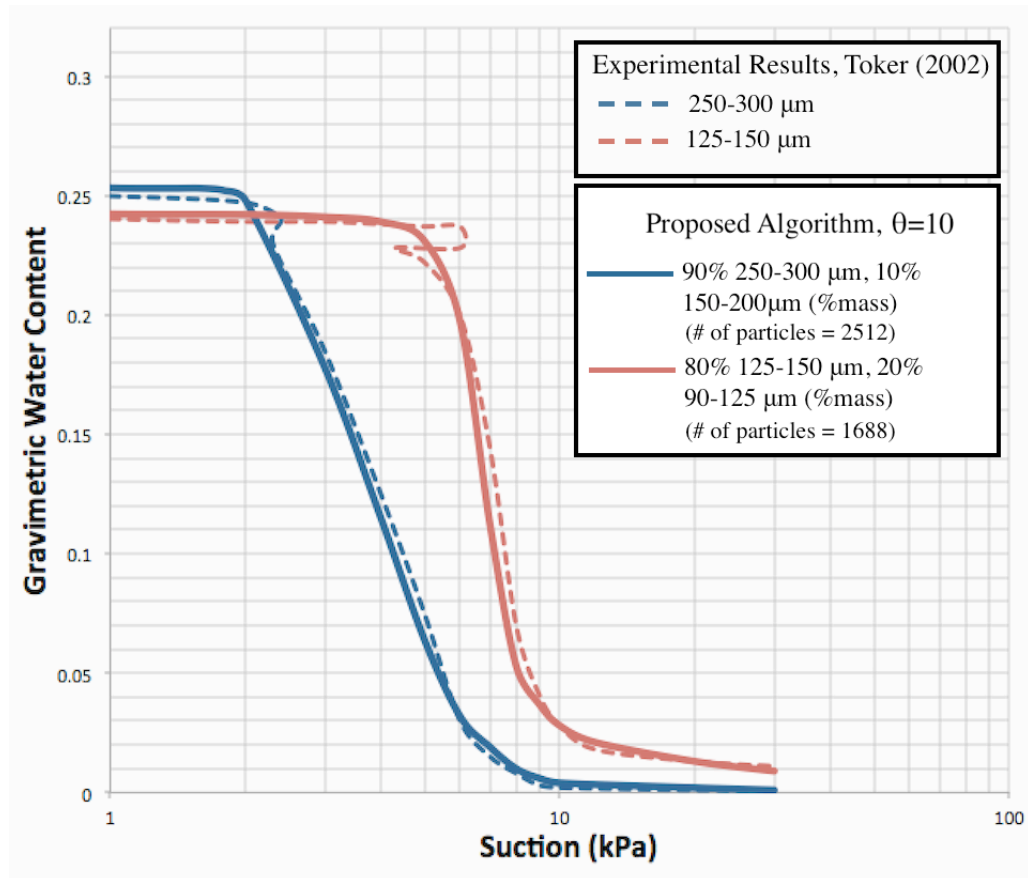
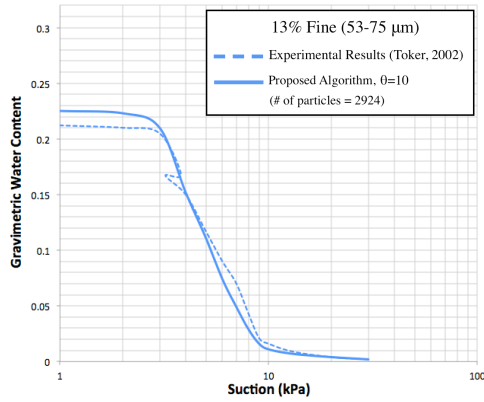
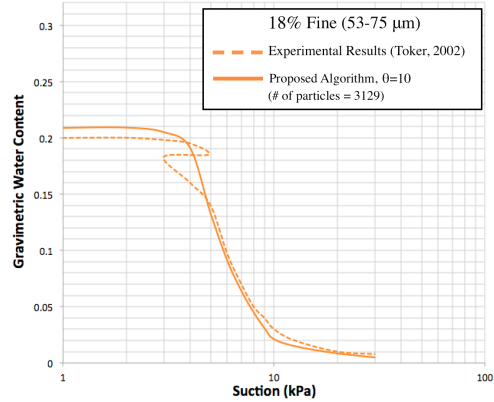


Figure 4.12: Comparison of simulated SWCC (modified fractions) with experimental results given by Toker (2002)

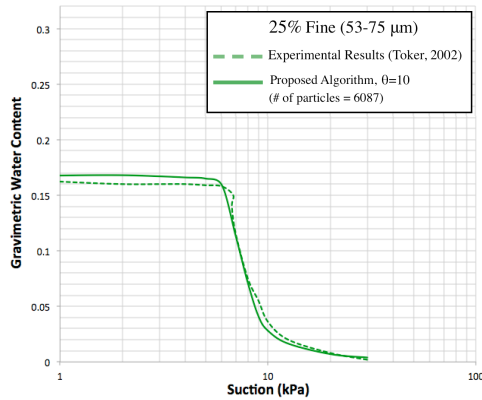
Finally, the SWCCs of gap-graded specimens with modified PSD (Figure 4.9) are simulated. The void ratios of gap-graded specimens (Toker, 2002) are given in Table 4.3. With respect to these void ratios the specimens are simulated. The simulated SWCC of gap-graded specimens are illustrated in Figure 4.13. Comparison of void ratio and AEP of simulate media with experimental data are presented in Figure 4.14. Distinction of the achieved void ratios with experimental data leads to small differences in AEP of SWCC.



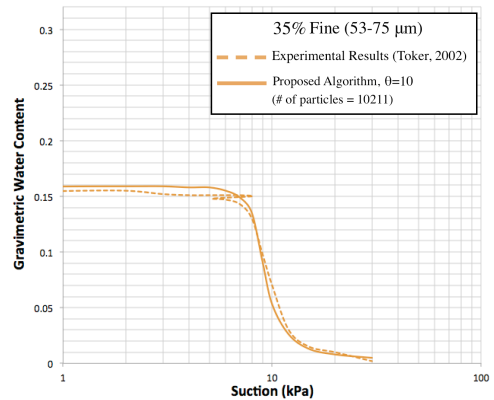
(a) 13% Fine



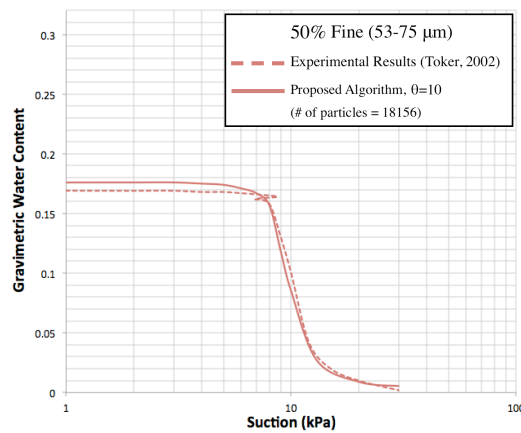
(b) 18% Fine



(c) 25% Fine

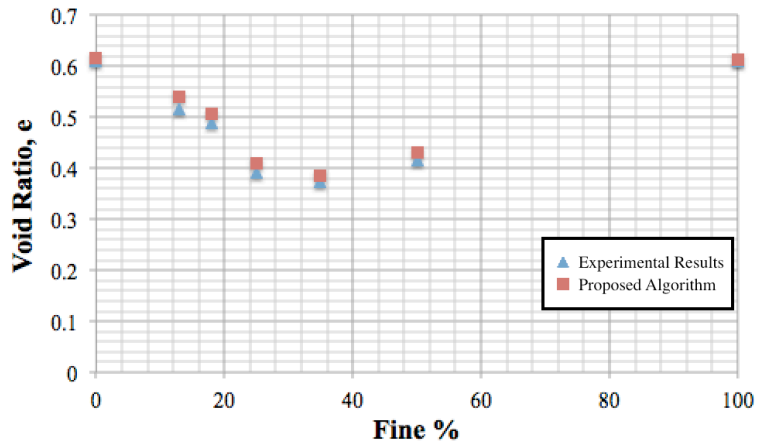


(d) 35% Fine

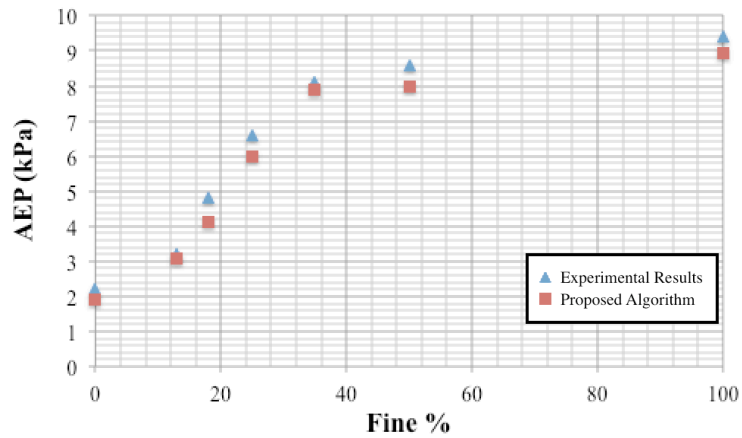


(e) 50% Fine

Figure 4.13: Simulated SWCCs of gap-graded specimens consist of (a) 13%, (b) 18%, (c) 25%, (d) 35% and, (e) 50% fine fractions and their comparison with experimental data given by Toker (2002)



(a) Void ratios



(b) AEP

Figure 4.14: Comparison of (a) void ratios and, (b) AEP of simulated media with experimental data of gap-graded specimens given by Toker (2002)

4.3 Verification with Real Soils

In nature, a soil structure consists of irregularly shaped particles. In this regard, experimental SWCC data of four types of soils are considered. With application of proposed algorithm (with spherical particles), conformity of obtained results with experimental outcomes is compared.

4.3.1 Material Properties

The experimental data of soils consisting of irregularly shaped sand and silt particles are gathered from different resources. The first set of data is chosen from Fredlund and Wilson (1997). The particle size distribution (PSD) of considered sandy soil by Fredlund and Wilson (1997) is presented in Figure 4.15. The specific gravity of sand particles is assumed to be 2.65.

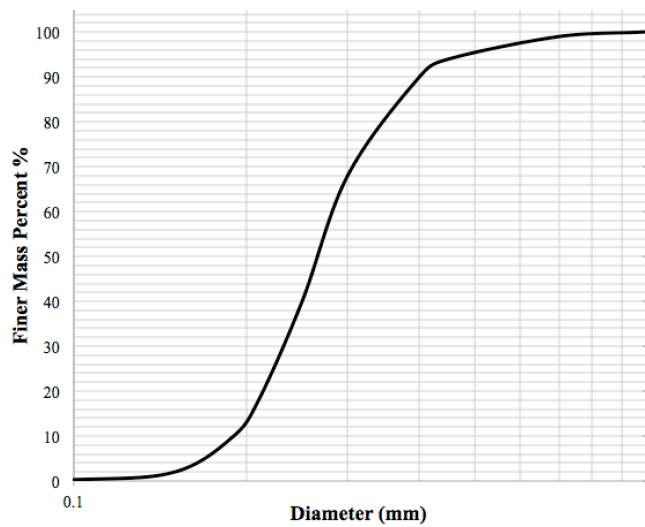


Figure 4.15: PSD of sand (Fredlund and Wilson, 1997)

Toker (2002) conducted laboratory tests (MIT method) to obtain SWCC of New Jersey Fine Sands (NJFS). The PSD of considered NJFS is shown in Figure 4.16. According to PSD of NJFS, 2.7% (mass) of particles are finer than $52\mu\text{m}$. In this regard, these particles are assumed to have diameter range of $20\text{-}52\mu\text{m}$. The shape of particles was visualized to be subrounded and equidimensional. The specific gravity of NJFS is assumed to be 2.65.

Ahmadi Adli (2014) determined the SWCC of quartz sand with hanging column method (section 2.5.2.1) in geotechnical laboratory of Middle East Technical University. The PSD of this soil is shown in Figure 4.17. According to PSD data, 2%

(mass) of particles have diameters finer than $75\ \mu\text{m}$. These particles assumed to have diameters in range of $60\text{-}75\ \mu\text{m}$. The specific gravity of quartz sand is 2.66. The dry density of considered specimen is $1.37\ (\text{g}/\text{cm}^3)$. According to microscopic photograph of quartz sand given in Figure 4.18, the shape of the majority of the particles is sub-angular.

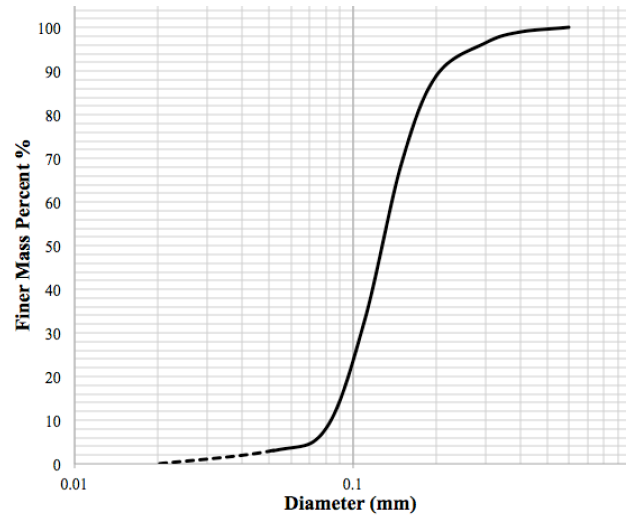


Figure 4.16: PSD of NJFS (Toker, 2002)

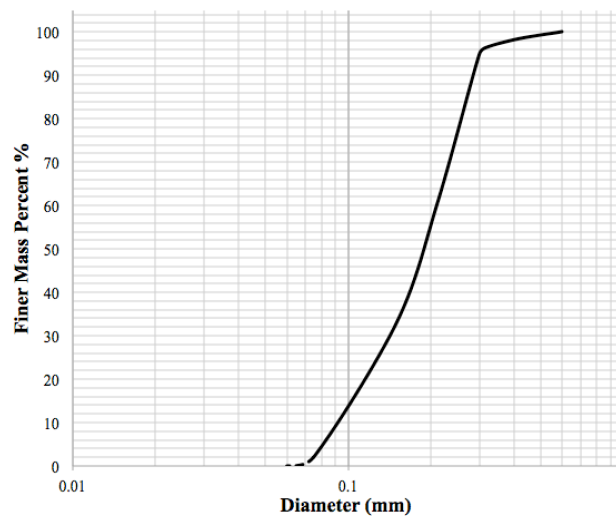


Figure 4.17: PSD of quartz sand (Ahmadi Adli, 2014)

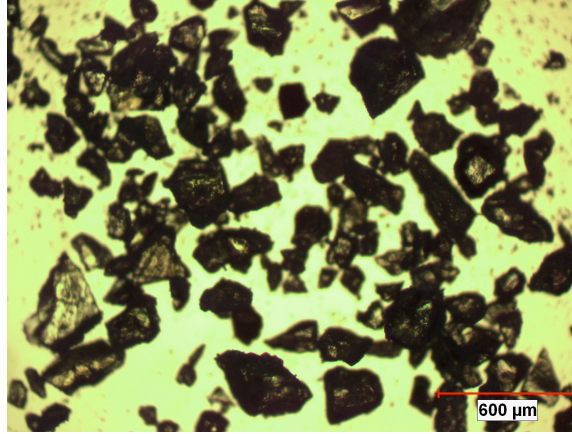


Figure 4.18: Microscopic photograph of quartz sand

The last set of data is also gathered from geotechnical laboratory of Middle East Technical University. Ahmadi Naghadeh (2014) utilized the pressure plate method (section 2.2.4) to determine the SWCC of quartz silts. Figure 4.19 illustrates the PSD of quartz silts. According to Figure 4.19, 4.89% (mass) of particles have diameters finer than 1 μm. Diameters of these particles are considered to be in range of 0.1-1 μm. The specific gravity of quartz silts is 2.66. The dry density of considered specimen is 1.31 (g/cm³). With regard to microscopic photograph of quartz silt, which is given in Figure 4.20, the shape of the quartz particles is angular.

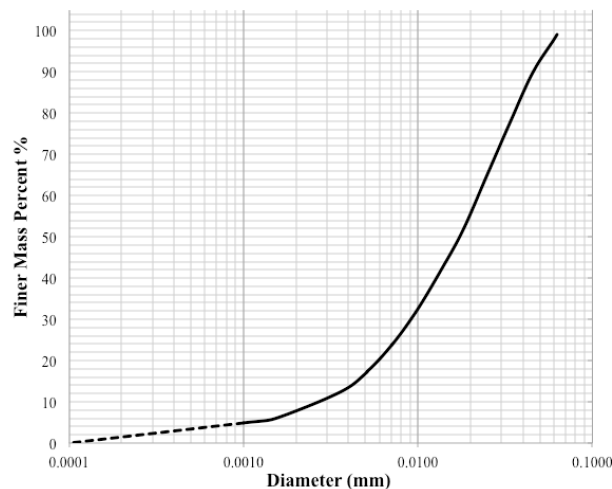


Figure 4.19: PSD of quartz silt (Ahmadi Naghadeh, 2014)

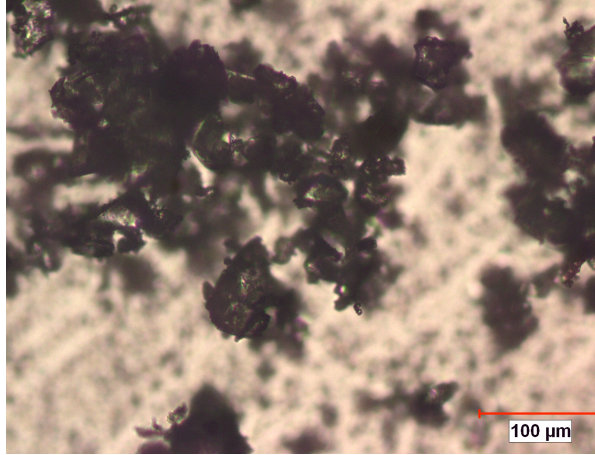


Figure 4.20: Microscopic photograph of quartz silt

Shapes, D_{10} , D_{60} , C_C (coefficient of curvature), C_U (coefficient of uniformity) and classification (USCS classification) of the real soils are presented in Table 4.4.

Table 4.4: Properties of real soils

Data Source	Soil Type	Shape	D_{10} (mm)	D_{60} (mm)	C_U	C_C	Class (USCS)
Fredlund and Wilson (1997)	Sand	N/A	0.19	0.28	1.47	0.99	SP
Toker (2007)	NJFS	Sub-Rounded	0.082	0.13	1.58	1.13	SP-SM
Ahmadi Adli (2014)	Quartz Sand	Sub-Angular	0.091	0.21	2.3	1.02	SP
Ahmadi Naghadeh (2014)	Quartz Silt	Angular	0.0025	0.022	8.8	1.47	ML

The physical properties of considered real soils are calculated from soil phase relations and presented in Table 4.5. The volumetric water content (Θ) of specimens is calculated with regard to gravimetric water content of soils.

$$\Theta = \omega \cdot \frac{\rho_d}{\rho_w} \quad (4.2)$$

where, ρ_d is dry density of specimen, and ρ_w is water density.

Table 4.5: Physical properties of real soils

Data Source	Soil Type	G_s	ρ_d	e	ω_{sat}	Θ_{sat}
Fredlund and Wilson (1997)	Sand	2.65*	1.64*	0.61	0.23	0.377
Toker (2007)	NJFS	2.65*	1.59	0.66	0.25	0.396
Ahmadi Adli (2014)	Quartz Sand	2.66	1.37	0.94	0.353	0.484
Ahmadi Naghadeh (2014)	Quartz Silt	2.66	1.31	1.03	0.387	0.507

* Assumed values

4.3.2 Estimation Methods

The SWCC of soils, which are presented in previous section, are estimated with application of two most common estimation techniques. In this regard, Arya and Paris (1981) as well as Fredlund and Wilson (1997) methods, which are discussed in section 2.5.3.2.1 and 2.5.3.2.2, respectively, are utilized.

4.3.2.1 Arya and Paris (1981) Method

For the PSD of sandy soil given by Fredlund and Wilson (1997) (Figure 4.15), the solid mass ratio (M) and mean particle radius (R) of each segment (divided in 8 segments) are calculated and presented in Table 4.6. The pore volume, volumetric water content, number of particles, mean pore radius and equivalent soil water pressure of each segments, which are the variables defined by Arya and Paris (1981), are calculated and presented in Table 4.7. In a similar procedure, these parameters can be obtained for the PSD of NJFS, quartz sand and quartz silt, which are given in Figure 4.16, 4.17 and 4.19, respectively. The empirical α parameter is approximated with regard to data given by Arya and Paris (1981). For sandy and silty soils α is considered to be 1.45 and 1.35, respectively. The contact angle is assumed to be 10

degrees. The estimated SWCC of considered soils with application of Arya and Paris (1981) method are presented in Figure 4.21 to Figure 4.24.

Table 4.6: Dividing the PSD of sandy soil into small segments

Segments	Solid Mass (W)	Mean Particle Radius (R)
1	0.05	0.3625
2	0.05	0.2125
3	0.24	0.175
4	0.26	0.1375
5	0.2	0.115
6	0.1	0.1
7	0.08	0.085
8	0.02	0.0625

Table 4.7: Arya and Paris (1981) parameters for sandy soil

Segments	Pore Volume (V)	Cumulative Volumetric Water Content (Θ)	Number of Particles (n)	Mean Pore Radius (r)	Equivalent Soil Water Pressure (ψ), kPa
1	0.011	0.018	0.094	0.44	0.325
2	0.011	0.036	0.46	0.18	0.794
3	0.055	0.126	4.02	0.09	1.58
4	0.059	0.222	8.98	0.06	2.38
5	0.046	0.297	11.81	0.047	3.04
6	0.023	0.334	8.98	0.043	3.32
7	0.018	0.363	11.7	0.034	4.2
8	0.004	0.369	7.35	0.028	5.1

4.3.2.2 Fredlund and Wilson (1997) Method

In order to estimate the SWCC of real soils with Fredlund and Wilson (1997) method, SoilVision database software is utilized. Fredlund and Wilson (1997) method is implemented in this program. With inputting the PSD data and physical properties of each soil (Table 4.5) into the program the estimated SWCC are obtained and presented in Figure 4.21 to Figure 4.24.

4.3.3 Simulated SWCC of Real Soils

Initially, the SWCC of sandy soil given by Fredlund and Wilson (1997) is simulated. To this end, spherical particles are generated and packed according to available PSD data (Figure 4.15) and objective void ratio (Table 4.5). The void ratio of simulated medium is 0.62, which is in the acceptable range of objective void ratio (± 0.02). The simulated SWCC of this soil with contact angle of 10 degree is presented in Figure 4.21.

Next, SWCC of NJFS is considered. According to PSD of NJFS given in Figure 4.16 and target void ratio of 0.66 (Table 4.5), the medium is simulated. In the end of simulation, void ratio of the medium is 0.654. For contact angle of 10 degree, the simulated SWCC of NJFS is determined and presented in Figure 4.22.

Afterwards, the SWCC of quartz sand given by Ahmadi Adli (2014) is simulated. According to PSD data given in Figure 4.17 and the target void ratio of 0.94 (Table 4.5), the medium is packed. In the end of particles packing procedure the void ratio of simulated medium is equal to 0.943. The simulated SWCC of quartz sand is illustrated in Figure 4.23. Note that the best fit is simulated at contact angle of 10 degrees.

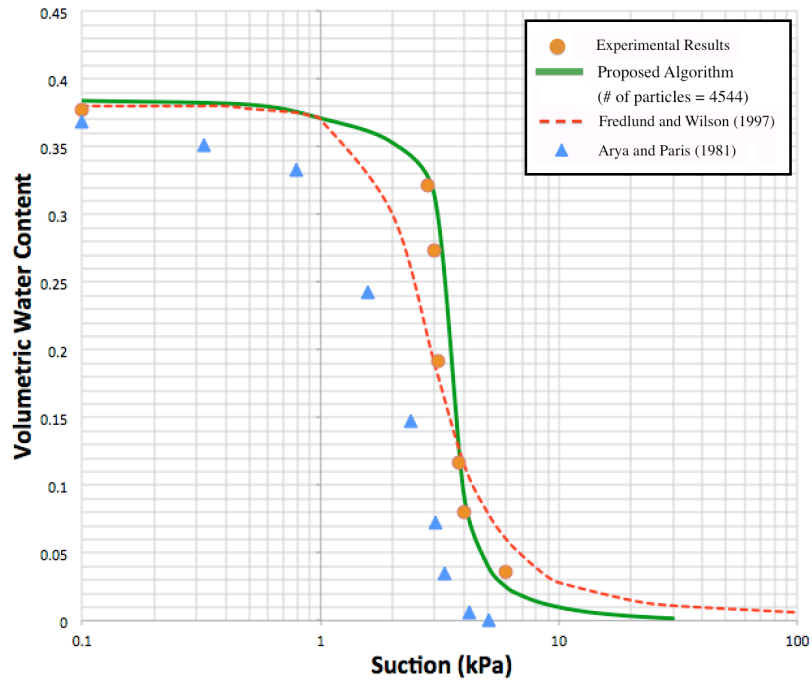


Figure 4.21: Comparison of the SWCC results of sandy soil with experimental data given by Fredlund and Wilson (1997)

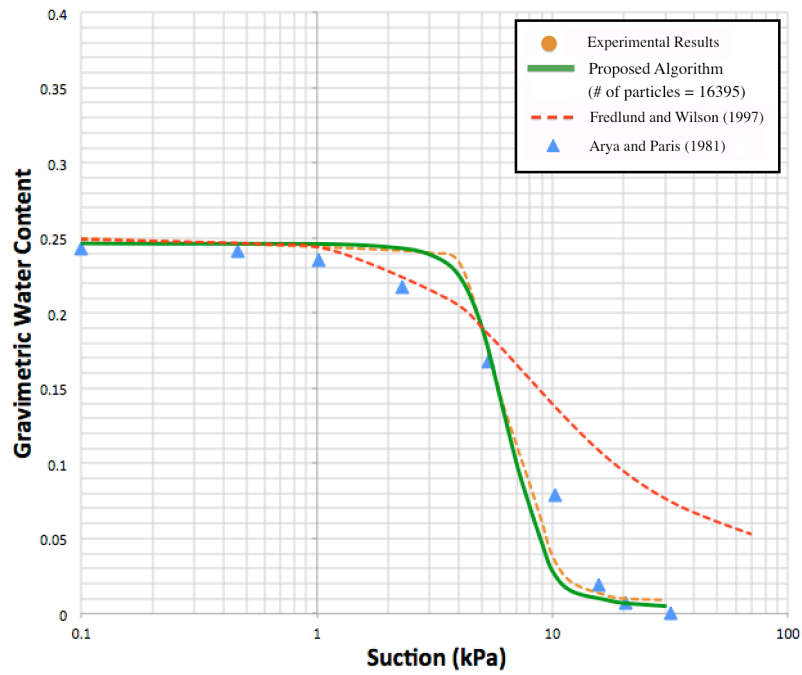


Figure 4.22: Comparison of the SWCC results of NJFS with experimental data given by Toker (2002)

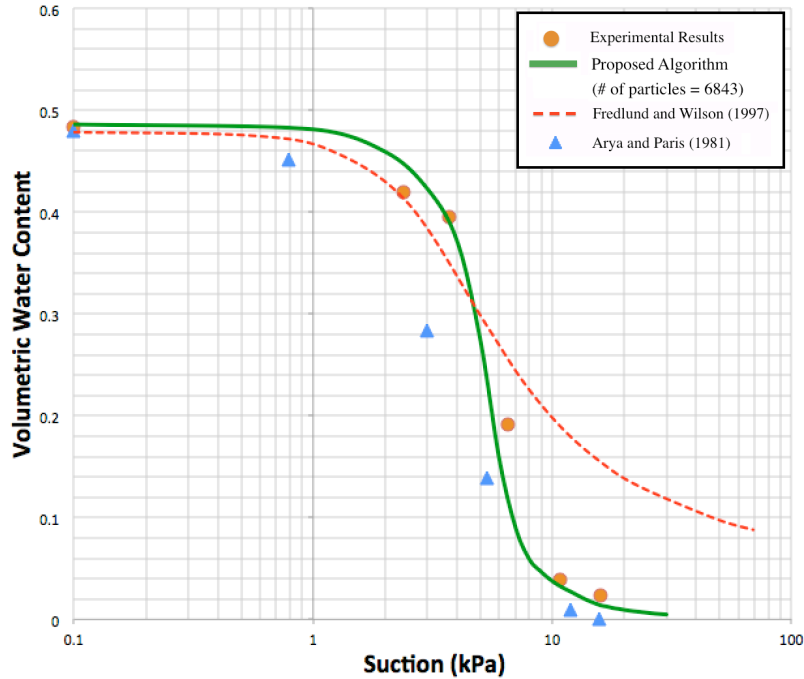
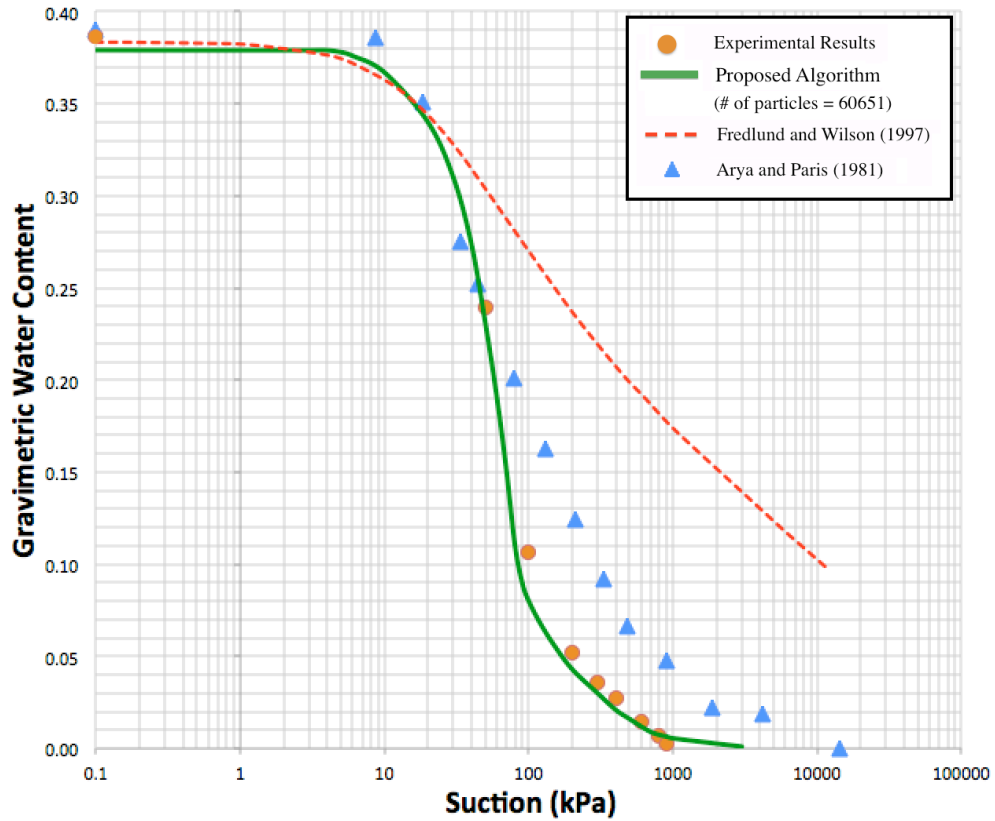


Figure 4.23: Comparison of the SWCC results of quartz sand with experimental data given by Ahmadi Adli (2014)

Finally, the SWCC of quartz silt given by Ahmadi Naghadeh (2014) is simulated. According to PSD data given in Figure 4.19 and the target void ratio of 1.03 (Table 4.5), the medium is generated. The void of simulated medium is equal to 1.012. In order to decrease the computing time, different suction intervals are considered. The simulated SWCC of quartz silt with contact angle of 10 degrees is presented in Figure 2.24.

Comparison of obtained AEPs, which is assumed as the suction value at 90% degree of saturation, and maximum slopes of SWCC (M), which is given in Eq. (4.3), that are determined from experimental, proposed algorithm and estimation techniques are presented in Table 4.8 and Table 4.9, respectively. According to these tables, proposed algorithm results in better estimation of SWCC in comparison to estimation methods. While comparing the estimation methods among each other, Arya and Paris (1981) method resulted in better slope estimations than Fredlund and Wilson (1997). In contrast, Fredlund and Wilson (1997) method yielded in better estimation of AEP.

$$M = \frac{\Delta\omega}{\Delta \log(\text{Suction})} \quad (4.3)$$



4.24: Comparison of SWCC results for quartz silt with experimental data given by Ahmadi Naghadeh (2014)

Table 4.8: Comparison of determined AEPs of real soils

Data Source	Soil Type	AEP (kPa)			
		Experimental Results	Arya and Paris (1981)	Fredlund and Wilson (1997)	Simulated Results
Fredlund and Wilson (1997)	Sand	2.3	0.85	1.4	2.2
Toker (2002)	NJFS	4.1	2.2	2.1	4
Ahmadi Adli (2014)	Quartz Sand	2.1	1.7	1.9	2.9
Ahmadi Naghadeh (2014)	Quartz Silt	18	19	20	19

Table 4.9: Comparison of maximum slope of resulted SWCC

Data Source	Soil Type	Maximum slope of SWCC (M)			
		Experimental Results	Arya and Paris (1981)	Fredlund and Wilson (1997)	Simulated Results
Fredlund and Wilson (1997)	Sand	1.53	0.68	0.62	1.78
Toker (2002)	NJFS	0.51	0.22	0.17	0.57
Ahmadi Adli (2014)	Quartz Sand	0.82	0.58	0.36	1.15
Ahmadi Naghadeh (2014)	Quartz Silt	0.44	0.23	0.1	0.46

While comparing the suction values of simulated and estimated methods with experimental data, the maximum relative error ($|\text{experimental data} - \text{estimation results}| / \text{experimental data}$) in suction for all of the real soils are determined and shown in Table 4.10.

Table 4.10: Comparison of maximum relative errors in suction values of real soils

Data Source	Maximum relative error in suction		
	Simulated Results	Arya and Paris (1981)	Fredlund and Wilson (1997)
Fredlund and Wilson (1997)	13.5%	68%	38%
Toker (2002)	25%	75%	660%
Ahmadi Adli (2014)	30.4%	57%	780%
Ahmadi Naghadeh (2014)	200%	1200%	9900%

While comparing the water content values of simulated and estimated methods with experimental data, the maximum absolute error ($|\text{experimental data} - \text{estimation results}|$) in water content for all of the real soils are determined and presented in Table 4.11.

Table 4.11: Comparison of maximum absolute errors in water content values of real soils

Data Source	Maximum absolute error in water content		
	Simulated Results	Arya and Paris (1981)	Fredlund and Wilson (1997)
Fredlund and Wilson (1997)	10%	20%	13%
Toker (2002)	1.2%	4.3%	10.5%
Ahmadi Adli (2014)	4.5%	10.1%	17%
Ahmadi Naghadeh (2014)	3.2%	7.5%	17.8%

4.4 Computational Performance

The goal of this research is to simulate the SWCC with superior accuracy than existing estimation methods while decreasing the time and cost required for conducting laboratory tests. As presented in section 4.3, the accuracy of proposed algorithm for simulating SWCC is much superior than available estimation methods. However, the time factor is in favor of considered estimation methods. For instance, the computing time for simulating SWCC of a uniform specimen that consists of 1000 particles (sand) is around 6 hours. Determining the AEP of pore throats is the most time consuming part of the simulation. This is due to convergence problems of Newton-Raphson method (section 3.4.4.1). With decreasing the uniformity of a specimen more particles will be generated. For example, a single particle with diameter of 300 μm will have a same mass as 64 particles with diameter of 75 μm (in the case of spherical particles and constant G_s). Yet, the total time for simulation of SWCC is by far less than standard laboratory tests. In laboratory, obtaining SWCC of a silty specimen with standard techniques takes weeks. With application of proposed algorithm, the computing time for simulating the SWCC of silty specimen, given by Ahmadi Naghadeh (2014), with more than 60,000 particles is around 3 days. All durations are for the simulation running on a computer with processor power of 2.7 GHz (Intel Core i7) and 16 GB of memory. Two factors have the most influence on

computing duration. The first factor is related to total number of generated particles inside the medium. With increasing the number of generated particles, more accurate SWCC will be simulated but the computing time will increase. This factor is function of total number of particles in coarsest segment of PSD (section 3.2.1), N_1 , which is an input of the algorithm. While considering the quartz sand given by Ahmadi Adli (2014), the effect of number of particles on simulated SWCC and computing time are presented in Figure 4.25 and Figure 4.26, respectively. The N_1 is assumed to be 1, 3, 5, and 10.

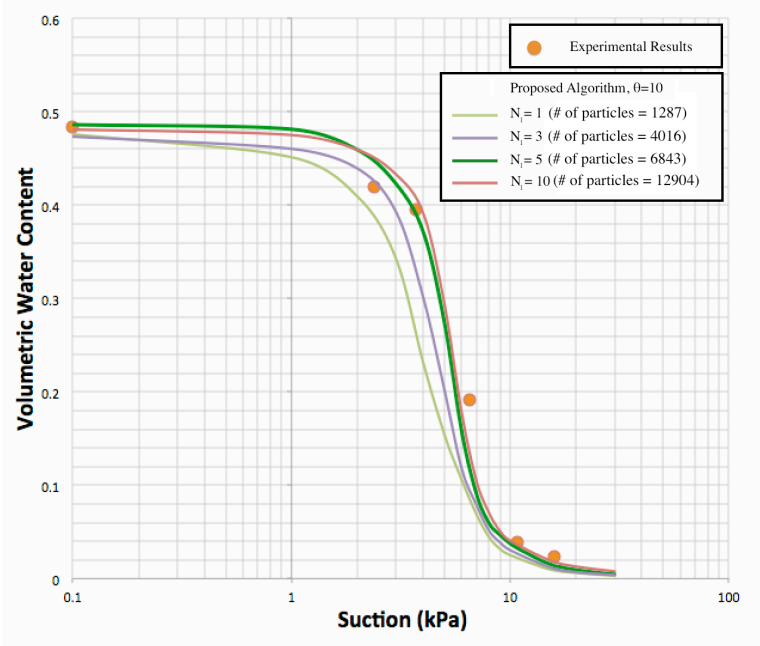


Figure 4.25: Effect of total number of particles on simulated SWCCs of quartz sand

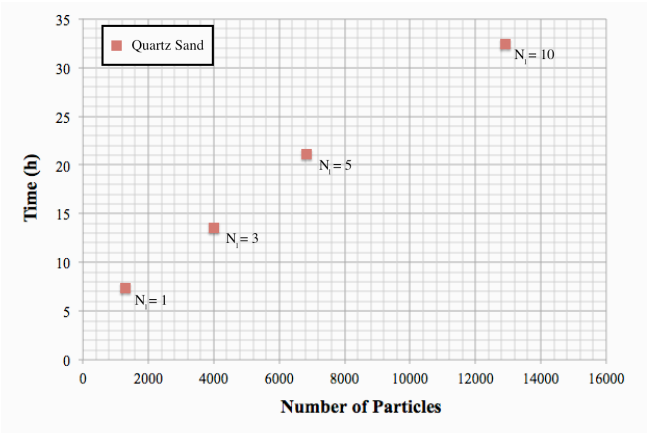


Figure 4.26: Effect of total number of particles on computing time

The number of applied suction levels is another key factor for controlling simulation time. In an instance, the sandy soils in comparison to silty soils will drain in lower suction values, so the simulation time will decrease (with same amount of particles). By defining the suction multiplier (Eq. (3.57)), which is also an input of the algorithm, the total number of applied suctions can be controlled. The effect of particles number on simulation time of soils composed of glass beads as well as real soils, which are considered in section 4.2 and 4.3, respectively, are illustrated in Figure 4.27.

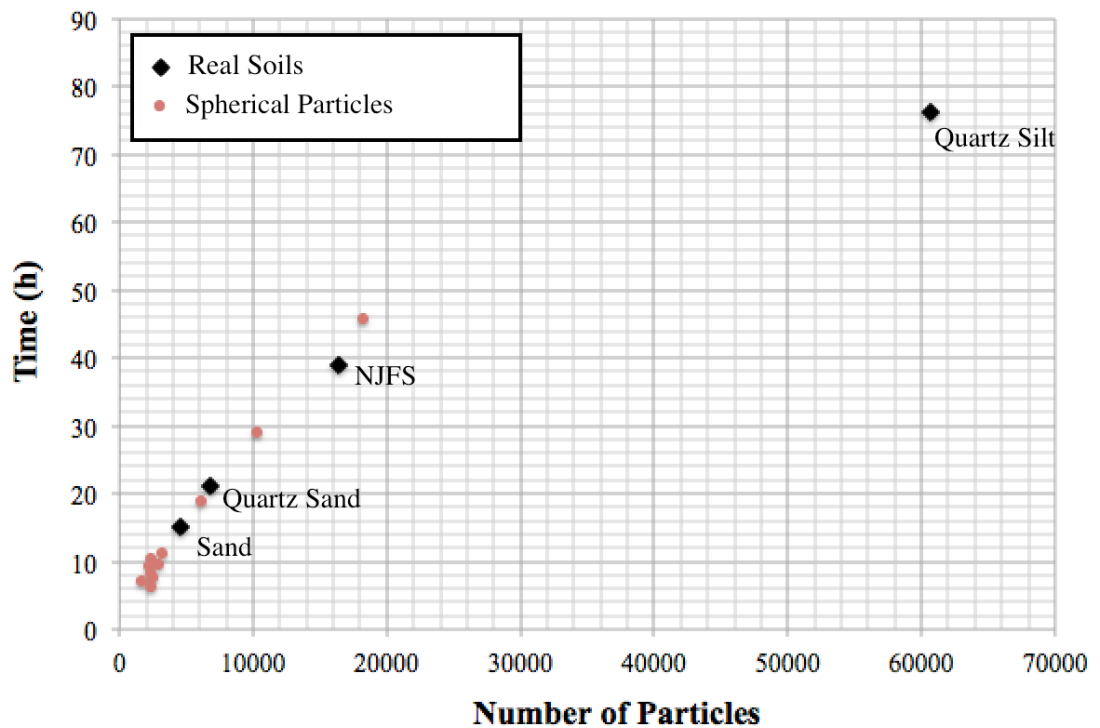


Figure 4.27: Computing time versus total number of particles

CHAPTER 5

CONCLUSION

5.1 Summary

The bulk of this study is development of a computer algorithm that simulates the SWCC of particulate soils. In order to simulate the SWCC, the physical properties of soil, which are particles size distribution (PSD) and void ratio (e), are considered as input of the algorithm. The methodology of proposed algorithm is discussed in detail in chapter 3. In chapter 4 of this dissertation, initially, the factors that can alter the outcome of SWCC simulation are investigated. Afterwards, the results of simulations are compared to laboratory data as well as existing methods of SWCC estimation. Finally, computing time of simulation is discussed. It has been proved that proposed algorithm results in superior SWCC simulations in comparison to estimation methods while it decreases the required time and cost in contrast to laboratory tests.

5.2 Discussion of the Results

The accuracy of the proposed method is evaluated in the fourth chapter. Initially, the effect of particles size, void ratio and contact angle on SWCC results are presented. It has been shown that AEP of soils have an inverse relation with particles size, void ratio and contact angle. Furthermore, the slope of SWCC increases with uniformity of a considered specimen, decreasing the void ratio and increasing the contact angle.

Next, comparison of the obtained SWCC with experimental results is considered. In the first attempt, experimental results of soils consist of glass beads are evaluated as these materials match the assumptions of the algorithm. The experimental data given

by Toker (2002, 2007) are employed to verify the obtained results. It has been shown that simulated SWCCs have perfect conformity with experimental results.

For the effect of irregular particles, the experimental results of four real soils are considered. In respect to PSD and void ratio of these soils, spherical particles are generated and packed. In case of irregular particles, the factor that can make the distinction between the results is related to assumption of spherical particles in proposed method. It has been noted that at contact angle of 10 degrees the best SWCC results are obtained. For all soils, the AEPs and slope of experimental and simulated SWCC results are compared and shown to have perfect conformity.

Finally, the accuracy of proposed method is compared to those of the estimation techniques that are available in the literature. The SWCC of soils comprised of irregular particles are estimated with Arya and Paris (1981) as well as Fredlund and Wilson (1997) methods. While comparing the results of estimation methods with each other, Arya and Paris (1981) method presents better approximation of slope of SWCC. However, it falls short in obtaining AEP of soils in comparison to Fredlund and Wilson (1997). While comparing the proposed algorithm with presented estimation techniques, differences in accuracy of methods are significant. The proposed method's accuracy in terms of determining the AEP, slope of SWCC and water content of medium after each suction application is much superior than available estimation techniques.

While considering the computing time of experimental methods with proposed algorithm, the time factor is in favor of proposed method. The time for simulation of SWCC with proposed algorithm is by far less than laboratory tests. The required time for simulation of SWCC can be also decreased with assumption of fewer particles in coarsest segment of PSD and increasing the suction intervals. However, these assumptions can lead to increased numerical errors. The effect of total number of particles on outcome of simulated SWCC is studied. According to results, the AEP of

simulated medium is slightly affected by total number of particles packed inside the medium.

5.3 Recommendations for Future Works

Although the proposed method has an acceptable level of accuracy, inability of obtaining exact objective void ratio as well as assumption of stationary and spherical particles resulted in small errors in the case of specimens composed of irregular particles. The first improvement can be made by taking the shape of particles into account. Application of regular shape particles will be the first alternative to spherical particles. This will result in a more realistic medium simulation by avoiding the complexity of irregular shapes.

Simulating the particles movement, which is a result of inducing suction and gravity, can also lead to an accurate SWCC. In this regard, implementation of discrete element methods (DEM) can be beneficiary in simulating the particles movement as well as obtaining the developed forces within a medium. With application of the proposed algorithm into DEM, the behavior of unsaturated soil mechanics might also be evaluated.

The exact volume of pendular rings has slight differences with considered toroidal pendular rings (Toker, 2002). An attempt to obtain the exact volume of pendular rings could be devoted. However, its impact on SWCC results will not be notable. Alternatively, the exact volume of bulk pores can be obtained with complex geometry methods. As mentioned before, this will result in an improvement over determining the volume of bulk pores and will not have considerable effect on SWCC results. To do so, regular Delaunay triangulation principle or dual Voronoi diagrams can be implemented.

The main improvement can be made in respect to determining the air entry pressure (AEP) of pore throats. Other numerical approaches can be implemented to eliminate

the divergence problems of Newton-Raphson method. In addition, defining better pore throat boundary conditions with consideration of continuity among pore throats can result in overall improvement of AEP acquisition process. Improving the pore throat AEP calculation subroutine not only can provide better SWCC estimations, but also it can decrease the computing time of proposed algorithm. Alternatively, in order to decrease the computing time of simulation, the correlation between AEP of pore throats and their dimensions can be considered.

The suction stress within the medium can also be determined with cutting cross-sections of medium and dividing resultant of all water forces normal to the cross-section to its area.

In this research pore-scale modeling of drainage of the water from the soil medium is simulated. With small alteration in AEP acquisition process and considering a dry medium at the beginning of the simulation, the wetting SWCC can also be extracted. The ability to provide both wetting and drying SWCCs would be a major advantage over laboratory tests and other estimation methods.

REFERENCES

Abichou, T., Benson, C. H., and Edil, T. B. (2004). Network Model for Hydraulic Conductivity of Sand-Bentonite Mixtures. *Canadian Geotechnical Journal*, 41(4), 698-712.

Adamson, N. K. (1960). *Physical Chemistry of Surfaces*. Interscience Publishers Inc.

Adler, P. M., and Thovert, J. F. (1998). Real Porous Media: Local Geometry and Macroscopic Properties. *Applied Mechanics Reviews*, 51, 537-585.

Ahmadi Adli, M. (2014). *Shallow Landslides Triggered by Rainfall in Unsaturated Soils*. Doctor of Philosophy Dissertation in Progress, Middle East Technical University.

Ahmadi Naghadeh, R. (2014). *Personal Communication*, Middle East Technical University.

Aitchison, G. D. (1965). *Moisture Equilibria and Moisture Changes in Soils Beneath Covered Areas*. Butterworths.

American Society for Testing and Materials (2000). *Annual Book of ASTM Standards*. American Society for Testing and Materials, West Conshohocken, PA, Vol. 04.08 and 04.09.

American Society for Testing and Materials (2003). *Annual Book of ASTM Standards*. American Society for Testing and Materials, West Conshohocken, PA, Vol. 04.08 and 04.09.

American Society for Testing and Materials (2014). Annual Book of ASTM Standards. American Society for Testing and Materials, West Conshohocken, PA, Vol. 04.08 and 04.09.

Amyx, J. W., Bass, D. M., and Whiting R. L. (1960). Petroleum Reservoir Engineering, McGraw-Hill, New York, NY.

Anderson, S. P., Dietrich, W. E., Torres, R., Montgomery, D. R., and Loague, K. (1997). Concentration-Discharge Relationships in a Steep, Unchanneled Catchment. Water Resources Research, 33, 211-225.

Arya, L. M., and Paris, J. F. (1981). Physicoempirical Model to Predict the SMC from Particle Size Distribution and Bulk Density Data. Soil Science Society of America Journal, Vol.45, 1023-1030.

Bear, J., and Verruijt, A. (1992). Modeling Groundwater Flow and Pollution. Reidel Publishing Company, Dordrecht.

Berthelot, M. (1850). Sur Quelques Phénomènes de Dilatation Forcée des Liquides/On Some Phenomena of Tensile Force of Liquids. Annales de Chimie et Physique, Vol.30, No.3, 232-237.

Blunt, M., and King, P. (1990). Macroscopic Parameters from Simulations of Pore Scale Flow. Physical Review A, 42, 4780-4787.

Bohren, C. F. (1987). Clouds in a Glass of Beer: Simple Experiments in Atmospheric Physics. John Wiley & Sons, New York, 51.

Boissonnat, J. D., Devillers, O., Pion, S., Teillaud, M., and Yvinec, M. (2002). Triangulations in CGAL. Computational Geometry: Theory and Applications, 22, 5-19.

Bouma, J. (1989). Using Soil Survey Data for Quantitative Land Evaluation. *Advances in Soil Science*, 9, 177-213.

Briggs, L. J. (1897). *The Mechanics of Soil Moisture*. US Department of Agriculture, Division of Soils, Bulletin No.10.

Briggs, L. J., and McLane, J. W. (1910). Moisture Equivalent Determinations and Their Application. *Proceedings of the American Society of Agronomy*, 2, 138-147.

Brooks, R. J., and Corey, A. T. (1964). *Hydraulic Properties of Porous Media*. Hydrology Paper 3, Colorado State University, Fort Collins.

Bryant, S., and Blunt, M. (1992). Prediction of Relative Permeability in Simple Porous-Media. *Physical Review A*, 46, 2004-2011.

Bryant, S., and Johnson, A. (2003). Wetting Phase Connectivity and Irreducible Saturation in Simple Granular Media. *Journal Of Colloid and Interface Science*, 263(2), 572-579.

Bryant, S. L., King, P. R., and Mellor, D. W. (1993a). Network Model Evaluation of Permeability and Spatial Correlation in a Real Random Sphere Packing. *Transport in Porous Media*, 11, 53-70.

Bryant, S. L., Mellor, D. W., and Cade, C. A. (1993b). Physically Representative Network Models of Transport in Porous-Media. *AIChE Journal*, 39, 387-396.

Buckingham, E. (1907). *Studies on the Movement of Soil Moisture*. Bulletin 38. USDA Bureau of Soils, Washington, DC.

Burdine, N. T. (1953). Relative Permeability Calculation from Pore Size Distribution Data. *Transactions of American Institute of Mining, Metallurgical and Petroleum*

Engineering, 198, 71-78.

Chareyre, B., Briancon, L., and Villard, P. (2002). Theoretical Versus Experimental Modeling of the Anchorage Capacity of Geotextiles in Trenches. *Geosynthetics International*, 9(2), 97-123.

Chatzis, I., and Dullien, F. A. L. (1977). Modeling Pore Structures by 2-D and 3-D Networks with Application to Sandstones. *Journal of Canadian Petroleum Technology*, 16, 97-108.

Chen, Y., Zhao, Y., Gao, H., and Zheng, J. (2011). Liquid Bridge Force Between Two Unequal-Sized Spheres or a Sphere and a Plane. *Chinese Society of Particuology and Institute of Process Engineering*, 9, 374-380.

Childs, E. C., and Collis-George, N. (1950). The Permeability of Porous Materials. *Proceeding of Royal Society of London, Series A*, 201, 392-405.

Chin, K. B., Leong, E. C., and Rahardjo, H. (2010). A Simplified Method to Estimate the Soil-Water Characteristic Curves. *Canadian Geotechnical Journal*, 47, 1382-1400.

Clark, W. C., Haynes, J. M., and Mason, G. (1968). Liquid Bridges Between a Sphere and a Plane. *Chemical Engineering Science*, 23, 810-812.

Coelho, D., Thovert, J. F., and Adler, P. M. (1997). Geometrical and Transport Properties of Random Packings of Spheres and Aspherical Particles. *Physical Review E*, 55, 1959-1978.

Conciani, W., Hermann, P. S., and Soares, M. M. (1996). The Time Domain Reflectometry to Study Matrix Suction. *Proceedings of the First International Conference on Unsaturated Soils, Paris, Vol.3*, 1481-1486.

Cook, B. K., Noble, D. R. and Williams, J. R. (2004). A Direct Simulation Method for Particle-Fluid Systems. *Engineering Computations: International Journal for Computer-Aided Engineering*, Vol.21, No.2/4, 151-168.

Corey, A. T. (1977). *Mechanics of Heterogeneous Fluids in Porous Media*. Water Resource Publication. Fort Collins, Colorado.

Coussy, O., and Fleureau, J. M. (2002). *Mecanique des Sols non Satures*, Hermes Science Publications, 137-174.

Cross, N. L., and Picknett, R. C. (1963). The Liquid Layer Between a Sphere and a Plane Surface. *Transactions of the Farady Society*, 59, 846-855.

Cundall, P. (1971). A Computer Method for Simulating Progressive, Large-Scale Movements in Blocky Rock Systems, Paper No. II-8, Proceedings of Symposium of the International Society for Rock Mechanics, Vol.1.

Dunsmuir, J. H., Ferguson, S. R., D'Amico, K. L., and Stokes, J. P. (1991). X-ray Microtomography. Proceedings of the 1991 SPE Annual Technical Conference and Exhibition, SPE 22860, Society of Petroleum Engineers, Dallas.

Edelsbrunner, H., and Shah, N. R. (1996). Incremental Topological Flipping Works for Regular Triangulations. *Algorithmica*, 15(6), 223-241.

Erle, M. A., Dyson, D. C., and Morrow, N. R. (1971). Liquid Bridges Between Cylinders, in a Torus, and Between Spheres. *AIChE Journal*, 17, 115-121.

Fatt, I. (1956). The Network Model of Porous Media I, II, III. *Transaction of American Institute of Mining, Metallurgical and Petroleum Engineering*, 207, 144-177.

Fatt, I., and Dykstra, H. (1951). Relative Permeability Studies. Transactions of American Institute of Mining, Metallurgical and Petroleum Engineering, 192, 249-256.

Fisher, R. A. (1926). On the Capillary Forces in an Ideal Soil. The Journal of Agricultural Science, 16, 492-505.

Fredlund, M. D., Fredlund, D. G., and Wilson, G. W. (1997). Prediction of the Soil-Water Characteristic Curve from Grain-Size Distribution and Volume–Mass Properties. In Proceedings of the 3rd Brazilian Symposium on Unsaturated Soils, Rio de Janeiro, Vol. 1, 13-23.

Fredlund, D. G., and Rahardjo, H. (1993). Soil Mechanics for Unsaturated Soils. 507.

Fredlund, M. D., Wilson, G. W., and Fredlund, D. G. (2002). Use of Grain Size Distribution for Estimation of the Soil-Water Characteristic Curve. Canadian Geotechnical Journal, 39, 1103-1117.

Fredlund, D. G., and Xing, A. (1994). Equations for the Soil Water Characteristic Curve. Canadian Geotechnical Journal, 31, 521-532.

Fredlund, D. G. (2006). Unsaturated Soil Mechanics in Engineering Practice. ASCE Journal of Geotechnical and Geoenvironmental Engineering, Vol.132, No.3, 286-321.

Gardner, W. R. (1958). Some Steady State Solutions of the Unsaturated Moisture Flow Equation with Application to Evaporation from a Water Table. Soil Science, 85(4), 228-232.

Gardiner, B. S. and Tordesillas, A. (2000). Micromechanical Constitutive Modeling of Granular Media: Evolution and Loss of Particle Contact in Clusters. Journal of Engineering Mathematics, Vol.52, 93-106.

Gibbs, J. W. (1873). A Method of Geometrical Representation of the Thermodynamic Properties of Substances by Means of Surfaces. Transactions of the Connecticut Academy, Vol. 2, 382-404.

Gupta, S. C., and Larson, W. E. (1979). Estimating Soil Water Retention Characteristics From Particle Size Distribution, Organic Matter Percent, and Bulk Density. Water Resources Research, Vol.15, No. 6, 1633-1635.

Haines, W. B. (1927). A Further Contribution to the Theory of Capillary Phenomena in Soils. The Journal of Agricultural Science, 17, 264-290.

Henderson, S. J., and Speedy, R. J. (1980). A Berthelot-Bourdon Tube Method for Studying Water Under Tension. Journal of Physics E-Scientific Instruments, 13, No.7, 778-82.

Hilfer, R. (2002). Review on Scale Dependent Characterization of the Microstructure of Porous Media. Transport in Porous Media, 46, 373-390.

Hilpert, M., Glantz, R., and Miller, C. T. (2003). Calibration of a Pore-Network Model by a Poremorphological Analysis. Transport in Porous Media, 51, 267-285.

Itasca Consulting Group (1999). PFC2D Users' Guide, Command Reference, FISH Reference, and Theory and Background, Minneapolis, MN.

Jerauld, G. R., Scriven, L. E., and Davis, H. T. (1984b). Percolation and Conduction on the 3D Voronoi and Regular Networks- a 2nd Case-Study in Topological Disorder. Journal of Physics C, Solid State Physics, 17, 3429-3439.

Koekkoek E. J. W., and Booltink, H. (1999). Neural Network Models to Predict Soil Water Retention. European Journal of Soil Science, 50, 489-495.

Kruyer, S. (1958). The Penetration of Mercury and Capillary Condensation in Packed Spheres. *Transactions of the Faraday Society*, 54, 1758-1767.

Laplace, P. S. (1806). *Mécanique Céleste*, Supplement to the Tenth Edition.

Latham, J. P., Lu, Y., and Munjiza, A. (2001). A Random Method for Simulating Loose Packs of Angular Particles Using Tetrahedra. *Geotechnique*, 51, 871-879.

Latham, J. P., Munjiza, A., and Lu, Y. (2002). On the Prediction of Void Porosity and Packing of Rock Particulates. *Powder Technology*, 125, 10-27.

Leveque, R. J. (2007). *Finite Difference Methods for Ordinary and Partial Differential Equations: Steady-State and Time-Dependent Problems*. Society for Industrial and Applied Mathematics.

Levine, S., and Neale, G. H. (1974). Theory of the Rate of Wetting of a Porous Medium. *Journal of the Chemical Society. Faraday Transactions II*, 71, 12-21.

Lewis, G. M., 1961. The Tensile Strength of Liquids in Berthelot Tubes. *Proceedings of the Physical Society*, 78-133.

Li, X., Li, J. H., and Zhang, L. M. (2014). Predicting Bimodal Soil-Water Characteristic Curves and Permeability Functions Using Physically Based Parameters. *Computer and Geotechnics*, 57, 85-96.

Lian, G., Thornton, C., and Adams, M. J. (1993). A Theoretical Study of the Liquid Bridge Forces Between Two Rigid Spherical Bodies. *Journal of Colloid and Interface Science*, 161, 138-147.

Lim, P., Barbour, S., Fredlund, D. (1998). The Influence of Degree of Saturation on the Coefficient of Aqueous Diffusion. *Canadian Geotechnical Journal*, 35, 811-827.

Liu, S. H., Sun, D. A. and Wang, Y. (2003). Numerical Study of Soil Collapse Behavior by Discrete Element Modeling. *Computers and Geotechnics*, Vol.30, 399-408.

Johari, A., Habibagahi, G., and Ghahramani, A. (2006). Prediction of Soil-Water Characteristic Curve Using Genetic Programming. *Journal of Geotechnical and Geoenvironmental Engineering*, ASCE, Vol. 5, 661-665.

Maris, H., and Balibar, S. (2000). Negative Pressures and Cavitation in Liquid Helium. *Physics Today*, 53(2), 29-34.

Mason, G. (1972). Desaturation of Porous Media, I. Unconsolidated Materials. *Journal of Colloid and Interface Science*, 41(2), 208-27.

Mattox, D. M. (1998). *Handbook of Physical Vapor Deposition (PVD) Processing: Film Formation, Adhesion, Surface Preparation and Contamination Control*. Noyes Publications, Westwood, NJ, 689.

Melrose, J. C. (1966). Model Calculations for Capillary Condensation. *AIChE Journal*, 12, 986-994.

Millington, R. J., and Quirk, J. M. (1961). Permeability of Porous Solids. *Transactions of the Faraday Society*, 57, 1200-1207.

Mualem, Y. (1976), A New Model for Predicting the Hydraulic Conductivity of Unsaturated Porous Media. *Water Resources Research*, 12, 513-522.

Nelson, J. D., and Miller, D. J. (1992). *Expansive Soils, Problems and Practice in Foundation and Pavement Engineering*. John Wiley and Sons Inc., New York.

Oda, M. (1974). *A Mechanical and Statistical Model of Granular Material, Soils and*

Foundations. Japanese Society of Soil Mechanics and Foundation Engineering, Vol.14, No.1, 13-27.

Pachepsky, Y. A., Timmlin, D., and Varallyay, G. (1996). Artificial Neural Networks to Estimate Soil Water Retention From Easily Measurable Data. Soil Science Society of America Journal, 60(3), 727-733.

Perera, Y. Y., Zapata, C. E., Houston, W. N., and Houston, S. L. (2005). Prediction of Soil-Water Characteristic curve Based on Grain-Size-Distribution and Index Properties. Advances in Pavement Engineering, 1-12.

Petrucci, R. H. (1989). General Chemistry: Principles and Modern Applications. Macmillan Publishing Company, New York.

Pierrat, P., and Caram, H. S. (1997). Tensile Strength of Wet Granular Materials. Powder Technology, 91, 83-93.

Pietsch, W., and Rumpf, H. (1967). Adhesion Capillary Pressure Liquid Volume and Angle of Contact of a Liquid Bridge Between 2 Spheres. Chemie Ingenieur Technik, 39, 885-893.

Pilotti, M. (2000). Reconstruction of Clastic Porous Media. Transport in Porous Media, 41, 359-364.

Piri, M., and Blunt, M. J., (2005). Three-Dimensional Mixed-Wet Random Pore-Scale Network Modeling of Two- and Three-Phase Flow in Porous Media, I. Model Description. Physical Review E, 71(2), 026301.

Rabinovich, Y. I., Esayanur, M. S., and Moudgil, B. M. (2005). Capillary Forces Between Two Spheres with a Fixed Volume Liquid Bridge: Theory and Experiment. Langmuir, 21, 10992-10997.

Ram, B. (2010). Numerical Methods. Pearson Education India.

Sjoblom, K. J. (2000). The Mechanisms Involved During the Desaturation Process of a Porous Matrix. Doctor of Philosophy Dissertation in Civil and Environmental Engineering. Massachusetts Institute of Technology, Cambridge, MA.

Sjoblom, K. J., and Germaine, J. T. (2001). Method and Apparatus for the Direct Measurement of Moisture Characteristics of Porous Samples of Soil, Wood, Concrete and the Like. U.S. Patent No. 6, 234, 008.

Smilauer, V., Catalano, E., Chareyre, B., Dorofeenko, S., Duriez, J., Gladky, A., Kozicki, J., Modenese, C., Scholtes, L., Sibille, L., Stransky, J., and Thoeni, K. (2010). Yade Reference Documentation. In V. Smilauer, Editor, Yade Documentation.

Spanne, P., Thovert, J. F., Jacquin, C. J., Lindquist, W. B., Jones, K. W., and Adler, P. M. (1994). Synchrotron Computed Microtomography of Porous-Media-Topology and Transports. Physical Review Letters, 73, 2001-2004.

Terzaghi, K. (1943). Theoretical Soil Mechanics. John Wiley and Sons, Inc., New York.

Thompson, K. E., and Fogler, H. S. (1997). Modeling Flow in Disordered Packed Beds from Pore-Scale Fluid Mechanics. AIChE Journal, 43(6), 1547-5905.

Thovert, J. F., Yousefian, F., Spanne, P., Jacquin, C. G., and Adler, P. M. (2001). Grain Reconstruction of Porous Media: Application to a Low-Porosity Fontainebleau Sandstone. Physical Review E, 63.

Toker, N. K., (2002). Improvements and Reliability of MIT Tensiometers and Studies on Soil Moisture Characteristic Curves. Master of Science Dissertation in Civil and Environmental Engineering. Massachusetts Institute of Technology.

Toker, N. K., Germaine, J. T., Sjoblom, K. J., and Culligan, P. J. (2004). A New Technique for Rapid Measurement of Continuous SMC Curves. *Geotechnique*, Vol.54, No.3, 179-186.

Toker, N. K. (2007). Modeling the Relation Between Suction, effective Stress and Shear Strength in Partially Saturated Granular Media. Doctor of Philosophy Dissertation in Civil and Environmental Engineering. Massachusetts Institute of Technology.

Trevana, D. H. (1987). *Cavitation and Tension in Liquids*. IOP Publishing Ltd, Philadelphia.

Urso, M. E. D., Lawrence, C. J., and Adams, M. J. (1999). Pendular, Funicular, and Capillary Bridges: Results for Two Dimensions. *Journal of Colloidal and Interface Science*, 220, 42-56.

Valvatne, P. H., (2004). Predictive Pore-Scale Modeling of Multiphase Flow. Doctor of Philosophy Dissertation in Earth Science and Engineering. Imperial College London.

Van der Waals, J. D. (1893). The Thermodynamic Theory of Capillarity Under the Hypothesis of a Continuous Variation of Density. *Verhandel Koninklijke Nederlandse Akademie van Wetenschappen*, Section 1, Vol.1, No.8.

Vanapalli, S. K., Fredlund, D. G., Pufahl, D. E., and Clifton, A. W. (1996). Model for the Prediction of Shear Strength with Respect to Soil Suction. *Canadian Geotechnical Journal*, Vol.33, 379-392.

Van Genuchten, M. T. (1980). A Closed-Form Equation for Predicting the Hydraulic Conductivity of Unsaturated Soils. *Soil Science Society of America Journal*, 44, 892-898.

Vereecken, H., Maes, J., Feyen, J., and Darius, P. (1989). Estimating the Soil Moisture Retention Characteristic from Texture, Bulk Density, and Carbon Content. *Soil Science*, 148, 389-403.

Vomocil, J. A. (1965). Porosity. In: Black, C.A. (Editor). *Methods of Soil Analysis: Physical and Mineralogical Properties, Including Statistics of Measurement and Sampling*. Madison, American Society of Agronomy, 499-510.

Wildenschild, D., Jensen, K. H., Hollenbeck, K. J., Illangasekare, T. H., Znidarcic, D., Sonnenborg, T., and Butts M. B. (1997). A Two-Stage Procedure for Determining Unsaturated Hydraulic Characteristics Using a Syringe Pump and Outflow Observations. *Soil Science Society of America Journal*, 61, 347-359.

Williams, J. R. and O'Connor, R. (1995). A Linear Complexity Intersection Algorithm for Discrete Element Simulation of Arbitrary Geometries. *Engineering Computations*, Vol.12, No.2, 185-201.

Williams, J., Prebble, R. E., Williams, W. T., and Hignett, C. T. (1983). The Influence of Texture, Structure and Clay Mineralogy on the Soil Moisture Characteristic. *Australian Journal of Soil Research*, 21, 15-32.

Yeong, C. L. Y., and Torquato, S. (1998a). Reconstructing Random Media. *Physical Review E*, 57, 495-506.

Zhang, L., ASCE, M., and Chen, Q. (2005). Predicting Bimodal Soil-Water Characteristic Curves. *Journal of Geotechnical and Geoenvironmental Engineering*, ASCE, 131, 666-670.